WARSAW UNIVERSITY
OF TECHNOLOGY

Faculty of Physics

Ph.D. THESIS

Marek Krzysztof Szuba, M.Sc., Eng.

**Long-range Correlations of Charged Hadrons
in Nucleus–Nucleus Collisions at the CERN SPS**

Supervisor
Prof. Marek Gaździcki, Ph.D.

Warsaw, 2009

Streszczenie

Od lat sześćdziesiątych ubiegłego wieku uważa się, iż hadrony — tj. większość sztucznie produkowanych cząstek wraz z obecnymi w jądrach atomowych protonami i neutronami — składają się z jeszcze mniejszych cząstek zwanych kwarkami. Jednocześnie uważa się, iż nie jest możliwe uwolnienie kwarku z wnętrza hadronu; fenomen ten nosi nazwę uwięzienia (ang. *confinement*) i pozostaje w zgodzie ze wszystkimi dotychczasowymi wynikami doświadczalnymi. Z drugiej strony, dzięki przeciwnemu a również dotyczącemu wiążącego kwarki oddziaływania silnego efektowi asymptotycznej swobody fizycy oczekują, iż odpowiednie warunki środowiskowe mogą spowodować przejście fazowe złożonej z kwarków materii do stanów, w których kwarki i gluony (nośniki oddziaływania silnego) mogą być traktowane jak swobodne. Jeden z takich stanów, którego charakterystyczną własnością jest wysoka temperatura, nosi nazwę plazmy kwarkowo-gluonowej (ang. *quark-gluon plasma*, QGP).

Chociaż wedle bieżącego stanu wiedzy QGP nie występuje już naturalnie nigdzie w naszym wszechświecie, jesteśmy w stanie odtwarzać odpowiednie warunki poprzez wysokoenergetyczne zderzenia ciężkich jąder atomowych, przyspieszanych do relatywistycznych prędkości w przyspieszaczach cząstek. Doświadczalne badania poświęcone poszukiwaniom plazmy kwarkowo-gluonowej prowadzone są w wielu posiadających tego typu urządzenia laboratoriach już od lat siedemdziesiątych ubiegłego wieku. Jeden z programów tego rodzaju badań rozpoczęto na początku lat 90 przy przyspieszaczu Super Proton Synchrotron w CERNie, w jego ramach prowadzono wiele eksperymentów poszukujących QGP w zderzeniach jąder ołowiu przy energii wiązki 158A GeV; jednym z tych eksperymentów jest NA49.

Z racji niezmiernie małej objętości i bardzo krótkiego czasu życia, produkowanej eksperymentalnie plazmy kwarkowo-gluonowej nie da się zaobserwować bezpośrednio. Zamiast tego analizuje się obserwable zawierające według naszych oczekiwań informacje o plazmie — czy to poprzez badanie ich w zderzeniach, w których spodziewamy się istnienia QGP i poszukiwanie rozbieżności względem systemów, w których plazma nie powstaje, czy też poprzez śledzenie ich w funkcji energii zderzenia i poszukiwanie jakościowych zmian mogących sugerować wystąpienie przejścia fazowego. Jedną z takich obserwabli są strumienie (ang. *jets*) — skupione w przestrzeni kaskady cząstek produkowanych w wyniku oddziaływań pojedynczych kwarków bądź gluonów, a nie hadronów jako całości (są to tzw. twarde procesy), a co za tym idzie najprawdopodobniej czułe na obecność w zderzeniu ośrodka złożonego ze swobodnych kwarków i gluonów. Jedna z metod pozwalających na obserwację kształtu strumieni w zderzeniach wykorzystuje ich skupienie, które obserwować można tworząc wielocząstkowe funkcje korelacji azymutalnych. Zastosowanie metod korelacyjnych do analizy danych ze zderzacza RHIC w BNLu okazało się wielkim sukcesem, z drugiej jednak strony aż do 2005 roku (kiedy to pierwsze wyniki tego rodzaju przedstawiła Kolaboracja CERES) metod takich nie stosowano w zakresie energii zderzeń oferowanych przez SPS. Jednym z istotnych powodów ku temu jest

znacznie większa niż w przypadku energii RHICa kłopotliwość obserwacji twardych procesów, jako że inne źródła korelacji azymutalnych są tu w stanie zniekształcić bądź zamaskować sygnał pochodzący od strumieni.

NA49 to spektrometr hadronowy o dużej akceptancji, który w latach 1995–2002 zebrał informacje o wielu różnego rodzaju zderzeniach — z różnymi zderzanymi cząstkami oraz przy różnych energiach wiązki. Jego główny element stanowią cztery duże Komory Projekcji Czasu, które dostarczają badaczom informacji o kinematyce cząstek w zderzeniu oraz umożliwiają ich identyfikację poprzez pomiar energii jonizacji (dE/dx). Dodatkową identyfikację cząstek o niskim pędzie bądź centrum akceptancji zapewniają dwa detektory Czasu Przelotu. Pozostałe części układu to szereg detektorów wyzwalających oraz służących pomiarowi położenia wiązki, a także wykorzystywany do określania centralności zderzeń jądro–jądro (poprzez pomiar energii pozostałości wiązki) Kalorymetr Weta. Mimo iż jego akceptancja w kącie azymutalnym nie jest jednorodna, dzięki dużej akceptancji ogólnej oraz szerokiemu wachlarzowi badanych systemów NA49 można traktować jako dobre źródło danych dla analiz korelacyjnych.

W ramach projektu opisanego w niniejszej pracy wyznaczyliśmy dwucząstkowe funkcje korelacji azymutalnych dla zderzeń proton–proton, centralnych zderzeń krzem–krzem oraz centralnych i półcentralnych zderzeń ołów–ołów przy energii 158A GeV, jak również dla centralnych zderzeń ołów–ołów przy energii 80A, 40A, 30A i 20A GeV; ponadto dla centralnych zderzeń jąder ołowiu przy energii 158A GeV byliśmy także w stanie wyznaczyć dwucząstkowe funkcje korelacji ($\Delta\eta$, $\Delta\phi$). Opisane i omówione zostały zastosowane cięcia na przypadki i ślady służące polepszeniu jakości mierzonego sygnału wraz z procedurami wyznaczania i szacowania statystycznych i systematycznych błędów pomiarowych. Wyznaczone funkcje wykorzystano w badaniach ich zależności od centralności i energii zderzeń, rodzaju zderzanych cząstek oraz ładunku elektrycznego bądź pędu poprzecznego cząstek produkowanych w zderzeniach. Funkcje uzyskane w zderzeniach ciężkich jąder przy maksymalnej energii SPS porównane zostały z wynikami eksperymentu CERES, podczas gdy wyniki eksperymentu PHENIX przy RHICu pozwoliły nam rozszerzyć badanie zależności od energii zderzenia. Wreszcie, porównaliśmy dwucząstkowe funkcje korelacji azymutalnych ze zderzeń proton–proton przy energii 158 GeV oraz z centralnych zderzeń ołów–ołów przy różnej energii, jak również dwucząstkowe funkcje korelacji ($\Delta\eta$, $\Delta\phi$) z centralnych zderzeń jąder ołowiu przy energii 158A GeV dla różnych zakresów pędu poprzecznego, z funkcjami opartymi na danych z modelu UrQMD.

Na podstawie powyższych obserwacji stwierdziliśmy, iż „daleka” strona dwucząstkowych funkcji korelacji azymutalnych zależy silnie od rozmiaru systemu, za to słabo od energii zderzenia bądź pędu poprzecznego produkowanych cząstek. Ponadto „daleka” strona funkcji wykazuje zgodność z UrQMD niezależnie od tego, czy model uwzględniał produkcję strumieni, czy też nie. Wyniki te odbiegają od oczekiwań opartych na założeniu, iż źródłem obserwowanych korelacji są strumienie i ich oddziaływania z plazmą kwarkowo-gluonową, są jednak zgodne z oczekiwaniami względem globalnego zachowania pędu. Z kolei w dwucząstkowych funkcjach korelacji ($\Delta\eta$, $\Delta\phi$) nie zaobserwowano kojarzonych z obecnością QGP struktur „grani”, które

widoczne są w wynikach przy energii RHICa. Z drugiej strony, amplituda strony „bliskiej" dwucząstkowych funkcji korelacji azymutalnych wyraźnie maleje wraz ze spadkiem energii zderzenia; w szczególności przy energii około 40A GeV korelacja zmienia się w antykorelację. Efekt ten nie jest widoczny w funkcjach pochodzących z symulacji, co sugeruje iż może on być związany z przejściem fazowym do QGP.

Abstract

It has been believed since the 1960s that hadrons — most artificially-produced particles as well as protons and neutrons making up atomic nuclei — consist in fact of even smaller particles called quarks. At the same time it is believed that it is impossible to free a quark from inside a hadron; this phenomenon is called confinement and has so far been confirmed by all experimental observations. On the other hand the opposite effect, asymptotic freedom, has led physicists to believe that under appropriate environmental conditions quark matter could undergo a phase transition into states in which quarks along with gluons (carriers of the strong force) could be considered deconfined; one of such states, characterised by high temperature, is called quark-gluon plasma (QGP).

Even though the QGP is thought no longer to naturally exist in our universe, we are capable of recreating appropriate conditions through the means of high-energy collisions of heavy atomic nuclei, hurried to relativistic speeds in particle accelerators. Experimental programs involving searches for the QGP have been in progress in a number of accelerator facilities around the world since the 1970s; one of such programs was launched in early 1990s at the Super Proton Synchrotron at CERN and involved a variety of experiments dedicated to searching for quark-gluon plasma in *Pb*+*Pb* collisions at the beam energy of 158A GeV, including the experiment NA49.

With minuscule droplet sizes and extremely short lifetime, experimentally-produced quark-gluon plasma cannot be observed directly and must be searched for by examining observables expected to be possible to trace back to when it existed — either by examining them in systems believed to contain the QGP and looking for discrepancies with respect to systems which do not, or by tracking their behaviour as a function of beam energy and looking for qualitative changes which could signify phase transition. One such observable is the shape of jets, collimated showers of particles originating from interactions of individual quarks/gluons rather than whole hadrons (the so-called hard scatterings) and as such expected to be sensitive to the presence of deconfined quarks and gluons. In turn, one of the methods which can be used to observe jet shapes in collisions takes advantage of their particles' collimation to produce multiparticle azimuthal-correlation functions. Its application to analysing data from experiments at the BNL RHIC has been a resounding success, however until 2005, when first results on the subject were shown by the CERES Collaboration, no analysis of this sort was performed in the energy range of the SPS — not least due to the fact the realm of hard processes is not as easy to access there as at the RHIC, with other correlation sources potentially capable of distorting or obscuring the jet signal.

NA49 is a large-acceptance hadronic spectrometer which between 1995 and 2002 collected information about a variety of different collision events, with several types of collided particles and for a wide range of collision energies. Its primary components are four large-volume Time

Projection Chambers, providing kinematic information about event particles as well as identifying them by ionisation energy loss (dE/dx). Two Time of Flight walls complement particle identification at low momentum and around mid-rapidity. The set-up also contains a plethora of small beam-position and triggering detectors, as well as a Veto Calorimeter used to determine centrality of nucleus–nucleus collisions through measurements of beam-remnant energy. In spite of its non-uniform azimuthal coverage, with its large acceptance and many different observed systems NA49 can be considered a good source of data for correlation studies.

In the study described in this dissertation we have produced two-particle azimuthal correlation functions for *p+p*, central *Si+Si* as well as central and mid-central *Pb+Pb* collisions at 158A GeV, along with central *Pb+Pb* events at 80A, 40A, 30A and 20A GeV; moreover, for central *Pb+Pb* collisions at 158A GeV we have also produced two-particle ($\Delta\eta$, $\Delta\phi$) functions. Event and track cuts used to improve quality of the observed signal, along with procedures for calculating and/or estimating statistical and systematic errors, have been described and discussed. The functions have been used in a number of scans attempting to establish trends of their behaviour with changing centrality, selection of charge or transverse momentum of paired particles, system size and beam energy. Results from the CERES experiment at the SPS have been used for reference for heavy-nucleus collisions at the top SPS energy, whereas functions from the PHENIX experiment at the RHIC have allowed us to extend the energy scan beyond the SPS. Finally, two-particle azimuthal correlation functions from *p+p* events at 158 GeV as well as from central *Pb+Pb* events at different collision energies, along with two-particle ($\Delta\eta$, $\Delta\phi$) functions from central *Pb+Pb* collisions at 158A GeV for a number of transverse-momentum bins, have been compared to the output of the string-hadronic model UrQMD.

Our results show the shape and amplitude away-side peak of two-particle azimuthal correlation functions to depend strongly on system size but only weakly on collision energy or transverse-momentum selection, moreover they agree with UrQMD regardless of whether jet production is enabled in the model or not. This is at odds with expectations regarding such correlations should they originate from jets and their modification by quark-gluon plasma but is consistent with effects of global momentum conservation. Furthermore no ridge-like structure, visible in RHIC results and associated with the QGP, has been observed in two-particle ($\Delta\eta$, $\Delta\phi$) correlations. On the other hand, the amplitude of the near-side peak in two-particle azimuthal correlations drops with decreasing energy and turns into a depletion around 40A GeV. This phenomenon is not visible in simulated functions, suggesting the possibility of its association with the onset of deconfinement.

Contents

List of Figures

List of Tables

Acknowledgements

The list of everyone who in one way or another has contributed to either this dissertation or the work which has led to it is very long and would be difficult for me to quote it here in its entirety. To all of you I give my most sincere thanks! Whether you are aware of it or not, I owe you one.

In particular, I would like to thank the following people:

- Marek Gaździcki — who first made it possible for my project to get started by persistently encouraging the heavy-ion group from Warsaw University of Technology to join NA49 and supporting our application once it had been submitted, then shared his knowledge and offered valuable guidance in the course of the project, and last but not least agreed to become my supervisor and helped me immensely to refine the dissertation. It is not an overstatement to say that without him, all this would likely never have come to be;
- Jan Pluta and the rest of the staff of the Heavy Ion Reaction Group of Warsaw University of Technology — who hooked me on heavy-ion physics, put up with me as a collaborator and then member of the group for 8 years and provided me with many opportunities to learn how to do science;
- All the students who worked at HIRG during my time there — for having made these 8 years interesting and worth remembering;
- All members present and former of the NA49 Collaboration, in particular its spokesmen Reinhard Stock and Peter Seyboth — for everything from having made the experiment come into being up to amusing conversations over coffee at collaboration meetings;
- Grażyna Odyniec and everyone else at the Relativistic Nuclear Collisions Group at Lawrence Berkeley National Laboratory, with whom I worked as a member of STAR Collaboration in 2006 and 2007 — working with them has taught me a lot not just about STAR, but about fine points of heavy-ion physics research in general;
- and finally, my family and friends — for having indulged and supported me in my strange desire to get a Ph.D., for having helped me get many an idea while chatting with them even though I suspect they often had no idea what I was talking about, and finally just for being there when I needed them.

For Qi, without whom I don't think I would have ever got to the stage when I could actually start writing this dissertation, who greatly motivated me to finish it in reasonable time — and who ever since Fortune brought us together has been making my life more complete in countless smaller and bigger ways.

– MS

Chapter 1

Introduction

1.1 Subject of the Dissertation

The primary task of the project that is the subject this dissertation is to observe and analyse long-range correlations between hadrons produced in collisions of nuclei at the Super Proton Synchrotron at CERN. Correlations of this sort are, according to state-of-the-art theoretical predictions, sensitive to the state of matter made up of colliding nuclei, thus providing one with a potentially useful probe of presence of *quark-gluon plasma* which is expected to be produced in most central heavy-ion events at energies in and above the range available at the SPS, and observation of whose properties could provide us insight into the nature of early periods of existence of our universe.

It has been believed since the 1960s that hadrons, that is — most artificially-produced particles as well as protons and neutrons making up atomic nuclei, consist in fact of even smaller particles called quarks. Those quarks are bound together by the so-called strong force (with the related degree of freedom known as colour charge and the force carrier called gluon), one of whose properties is that its intensity grows with distance — thus on one hand *confining* quarks to hadrons (*i.e.* making the latter impossible to break into constituents) and on the other giving them essential freedom when they are very close to each other. This second phenomenon, known as *asymptotic freedom*, has led physicists to believe that extreme environmental conditions could cause a phase transition of quark matter into states where quarks and gluons can be considered independent; one of such postulated states is the quark-gluon plasma.

As our universe has both expanded and cooled down significantly comparing to the time right after the Big Bang, the QGP is thought no longer to exist anywhere in it[1]; moreover. Then again, we are capable of artificially re-creating such extreme conditions by colliding particles hurried to immense velocities in *accelerators*. It is believed that if a collision of accelerated heavy nuclei accelerated to near-light speed velocities will generate high enough energy density for the phase transition to occur. Experiments dedicated to this field of scientific research have

[1] Unlike certain other deconfined states, which are expected to be present inside dense stellar objects such as neutron stars and/or black holes.

been running in several facilities worldwide, in particular at the SPS at CERN in France and Switzerland as well as the RHIC at BNL in the United States, soon to be followed by projects associated with the most powerful particle accelerator ever built, the recently-launched Large Hadron Collider at CERN.

Minuscule time and length scales involved forbid one from observing experimentally-produced quark-gluon plasma directly in nucleus-nucleus collisions. As a result, a number of probes have been postulated, which can both be observed in (or derived from) experimental data and, if present together, imply existence of the quark-gluon plasma in a collision. One of such probes is the modification of shape of jets — collimated showers of particles which are produced in "hard" scattering of individual quarks and gluons, expected therefore to be sensitive to their increased freedom in the QGP. The abundance of non-jet particles in the transverse momentum range available at SPS energies makes it infeasible to reconstruct jets on an event-by-event basis, it is however possible to determine their positions statistically by taking advantage of how strongly they are correlated in momentum space, in particular in azimuthal angle. This approach has been shown to be highly successful by RHIC experiments, producing possible evidence of the presence of quark-gluon plasma in most-central heavy-ion collisions, however until recently[2] no such analyses were performed in the energy range available at the SPS.

The research project described in this dissertation has involved investigating long-range particle correlations in the energy range of the CERN SPS using the data acquired by the NA49 experiment. A number of different systems at different collision energy has been analysed and compared to models as well as other experiments, in order to extend our knowledge of such correlations into the SPS energy range and attempt to provide additional information on whether or not heavy-ion collisions at that accelerator have witnessed production of a hot medium of deconfined quarks and gluons.

What makes analysing jet shape modification using long-range particle correlations particularly challenging at SPS energies is the fact that hard scatterings contribute very little to the overall yield of particles produced in collisions, even at the highest available p_T. As a consequence, correlation signals from non-jet sources — resonance decays, conservation laws, quantum correlations — play a much bigger role at the SPS than at the RHIC. A significant portion of the project described in this dissertation has been dedicated to an attempt to identify the dominating component of the correlation function, thus facilitating a meaningful interpretation of the results.

1.2 Fundamental Interactions and the Structure of Matter

It would be truistic to say that our universe and everything in it are governed by interactions between its elementary particles. Without interactions the universe would either be a uniform and completely neutral "soup" or, taking the Big Bang theory into account (more on that later),

[2] First results on the subject were shown in 2005 by the CERES Collaboration.

never have expanded at all. Without interactions there would be no stars, no planets and no living organisms; even in the macro scale they are the ultimate basis of all the complexity around us, from the way bacteria find their way through space to the human civilisation itself.

There is of course more than one kind of interactions, at least within the boundaries of our perception — which doesn't stop many renowned researchers from hoping we will one day be able to describe them all in common terms, the so-called Grand Unification Theory. A present-day, accurate (and quite possibly correct, albeit not complete — for one thing, it doesn't include gravity) description of these mechanisms as we understand them today is contained in the so-called *Standard Model* — a quantum field theory developed in the early 1970s [1]. Despite its incompleteness, its agreement with all existing experimental results has made it remain to these days a useful illustration of most processes occurring in micro scale.

According to the Standard Model all matter ultimately consists of only 12 fundamental particles; the same rule applies to antimatter. Basing the forces these 12 particles are sensitive to one can divide them into two classes; by comparing their other properties it is possible to subdivide each class further, into pairs called *generations*:

1. Leptons:

   - electron e, electron neutrino ν_e;
   - muon μ, muon neutrino ν_μ;
   - tau τ, tau neutrino ν_τ.

   Leptons are not sensitive to the strong force (see below). They all have fractional spin (they are fermions) and possess electric charge of 0 (neutrinos) or -1 (the others). Their mass range is very wide: from $(0-0.13)\times10^{-9}$ through $(0.009-0.13)\times10^{-9}$ to $(0.04-0.14)\times10^{-9}\ GeV/c^2$ for neutrinos and from 0.000511 through 0.106 to $1.777\ GeV/c^2$ for their charged counterparts [2];

2. Quarks:

   - down d, up u;
   - strange s, charm c;
   - bottom b, top t.

   Quarks do interact strongly. While they are fermions as well, their electric charge is fractional: $-\frac{1}{3}$ (d, s, b) or $\frac{2}{3}$ (u, c, t). Their approximate masses[3] are, respectively: 0.005, 0.002, 0.1, 1.3, 4.2 and $173\ GeV/c^2$ [2].

The convention assigns the same base names to antiparticles but prefix their names with *anti-* and place bars over the symbols: antielectron $\bar{e}$, tau antineutrino $\bar{\nu}_\tau$, antistrange quark $\bar{s}$ *et cetera*.

[3] The nature of the strong force (more on that later) makes it more-or-less impossible to obtain exact values here so they are published as ranges; the numbers quoted here are averages from such ranges

These particles can be affected by four different forces. As any interaction in the quantum world can be described as an exchange of *force-carrier* particles[4], each of the four forces can be assigned at least one such carrier. The four forces are:

1. As mentioned above, **gravity** is not in fact described by the Standard Model[5] despite being the most common of the forces and highly important in macro and astronomic scales; on the other hand, owing to their low masses it is so weak at the level of elementary particles (10^{41} times weaker than the electromagnetic force) that this omission has not yet caused any significant problems in the field. It will not be discussed further in this work;

2. The **electromagnetic** force, being second to none but the strong force in intensity while at the same time theoretically infinite in range, is particularly important at the level of atoms - it governs all atomic reactions and keeps atoms and ions stable. At the level of elementary particles it is still much weaker than the strong force and therefore only plays a secondary role, which however doesn't prevent many of its effects from being non-negligible or even highly significant. Its carrier particle, the *photon*, is well known and massless;

3. The **weak** force, while stronger than than gravity (it is about 10^4 times weaker than electromagnetism), has a very limited range ($10^{-16} - 10^{-17}\ m$) and only affects fundamental particles; it is therefore only significant in subatomic systems. Since it is quite different from the previous two forces (for example, its carriers — the $W^{\pm}$ and Z^0 bosons — possess mass in non-negligible amounts[6]), specifying whether it's repulsive or attractive is not trivial; however, it can be told that the weak force is responsible for certain kinds of radiative decays. Its characteristic behaviour is that it is capable of *changing the flavour of fundamental particles*: in beta decays for example the weak force changes a down quark into an up quark, transforming a neutron into a proton.

   At the same time the weak force is speculated to be related with the existence of *dark matter* — matter which we cannot observe but which is believed to be in strong majority in our universe: one of the hypotheses tries to explain it in terms of weakly interacting massive particles (WIMPs)[7].

   In 1967 Weinberg, Glashow and Salam unified the electromagnetic and the weak force into one; their formulation of the *electroweak* theory has been rewarded with a Nobel Prize in 1979 and constituted an important step on the way to the Standard Model. This is the second electromagnetic force-related unification, the first being James Maxwell's famous four equations from 1864 which unified the electric and the magnetic force;

[4] This is but one way of describing forces; the other describes them in terms of fields. Naturally both approaches are interchangeable.

[5] Primarily due to difficulties with unifying quantum field theory and general relativity

[6] 80.1 and 91.187 GeV/c^2, respectively

[7] As opposed by neutrinos, which interact almost exclusively weakly but possess very small — albeit non-zero, as proven in 1998 by the Super-Kamiokande collaboration [3] — masses

4. The **strong** force, affecting only quarks, is the strongest of the four (60 times as strong as electromagnetism) and purely attractive. This is what holds non-fundamental particles (in its basic form) and atomic nuclei (in the so-called *residual* form) together. Its carrier, the *gluon*, is massless and electrically neutral. The strong force is quite limited in range (up to $\approx 10^{-15}\ m$), on the other hand its intensity increases with distance; this behaviour and its consequences are of the essence to the subject of this dissertation and will be discussed at greater depth further on.

The forces' strengths were compared for two u quarks $3 \times 10^{-17}\ m$ apart.

1.2.1 Quantum Chromodynamics

With the advent of rapid progress in the field of experimental particle physics in the 1950s, which resulted in discovery of literally tens of new hadron species, scientists began to believe that they could not all be fundamental. A number of attempts were made to classify hadrons, ultimately resulting in formulation of the quark theory in 1963 by Murray Gell-Mann and George Zweig. Consequently, it was found out that quarks need to possess an additional SU(3) gauge degree of freedom in order for the quark model to encompass all known species of hadrons. This new degree of freedom, introduced along with a new carrier boson — the gluon — in 1965 by Moo-Young Han with Yoichiro Nambu and Oscar W. Greenberg, was later called the colour charge, whereas the whole theory received the name of *quantum chromodynamics* (QCD).

The moniker "colour" illustrates quite well the way the strong force binds quarks in hadrons: in a nutshell, the total colour of all the quarks[8] in a hadron must be "white". With six available values of the colour charge (named red (r), green (g), blue (b), antired ($\bar{r}$), antigreen ($\bar{g}$) and antiblue ($\bar{b}$)) one can achieve this in three different ways, thus dividing hadrons into three base categories:

- **mesons** — combinations of colour and respective anti-colour: $r\bar{r}$, $g\bar{g}$, $b\bar{b}$. This class encompasses all known two-quark hadrons, none of which however are stable;
- **baryons** — combinations of three quarks in rgb colour configuration. This class encompasses all known three-quark hadrons, including the stable protons and neutrons;
- **antibaryons** — like baryons, but with anti-colour: $\bar{r}\bar{g}\bar{b}$.

An interesting feature of the strong force according to quantum chromodynamics is that not just quarks but gluons too are thought to carry the colour charge. There are eight possible colour states available to a gluon, roughly corresponding to different combinations of one unit of colour coupled with one unit of anti-colour. One notable consequence of this is that colour is continuously exchanged between quarks in a hadron instead of being fixed; furthermore, the force field between two quarks behaves more than a spring that of gravity or electromagnetism, resulting in the aforementioned increase of strength with distance.

[8] Valence quarks, to be exact — QCD also features virtual "sea" quarks and gluons.

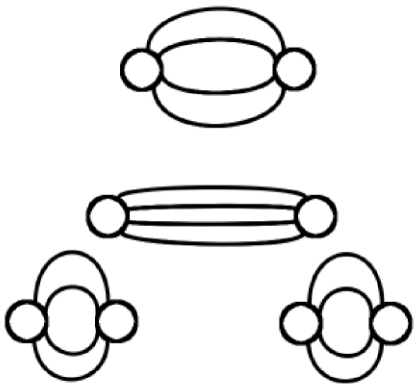

Figure 1.1: This figure illustrates how the strong force between two quarks changes while they're being moved apart by employing a popular model depicting the field between them, or *flux tube*, as strings. Top: the quarks are relatively close together and the strings between them are almost loose. Middle: as the quarks are moved apart the strings become more drawn, symbolising the potential energy increase. Bottom: after the flux tube's energy has passed the q-$\bar{q}$ creation threshold the strings snap, separating the system into two sets of still-confined quarks.
More complex systems (three-quark coupling or flux tubes with gluons inside) are too complicated to be drawn clearly, but the principle remains.

Despite having been in use for many years, many problems of QCD can still be solved either only approximately or not at all, leaving many gaps in our understanding of practical implications of the theory. Even so, what we do know has allowed us to establish two peculiar properties of the strong force:

- **asymptotic freedom** — interactions of quarks and gluons grow weaker as the distance between them decreases. Discovery of this phenomenon in 1973, independently by David Politzer and David Gross with Frank Wilczek [4, 5], was the subject of the 2004 Nobel Prize in Physics. Asymptotic freedom is particularly important from the point of view of experimental physics, as it matches quite well the conditions achieved by strongly interacting matter in high-energy collisions in accelerators;

- **confinement** — since the force between quarks grows in strength as the distance between them increases, *they can never be separated*. The energy stored in the interaction "string" results in creation of new quark-antiquark pairs instead, preventing emergence of free quarks (see Figure 1.1). Although confinement has not been analytically proven yet, it is believed to be true because it can be demonstrated using approximate solutions and can explain the lack of success in all searches for free quarks.

A number of approaches have been developed over the years in order to facilitate solving of problems of quantum chromodynamics. Among those approaches, the two that, thanks to their immense contributions to the field, warrant particular attention are: *lattice* and *perturbative* QCD.

Perturbative QCD (pQCD) approximates solutions of quantum chromodynamics through the use of perturbation theory. It is fairly limited in scope, as inherent qualities of perturbative approaches mean that in quantum chromodynamics they can only be accurate in the realm of asymptotic freedom — which experimentally can be accessed by high-energy collisions. pQCD has been growing in accuracy over the years and is now the source of the most precise existing tests of quantum chromodynamics, as well as a basis of our quite thorough understanding of high-energy interactions of quarks and gluons.

Lattice QCD on the other hand is a numerical approach, in which analytically intractable path integrals are simplified by reducing the space-time to a discrete lattice. Despite this simplification the calculations remain extremely complex and can only be performed employing significant amounts of computing power — typically clusters of ordinary personal computers joined together into massively parallel systems. These difficulties aside however, lattice QCD can be applied to a wide range of cases that are beyond the reach of perturbative methods and therefore keep providing new insight into the realm of confinement.

1.2.2 The Phases of Strongly Interacting Matter

With quantum chromodynamics providing information about dynamics of quarks and gluons, one can among other things begin to consider the matter of *phases* strongly-interacting matter can take.

As described earlier on in this section, under normal conditions quarks and gluons are confined to hadrons — however, lattice QCD calculations imply that other states can exist if the conditions are right. In particular, this implication postulates existence of the phenomenon of *deconfinement*: a transition from "unbreakable" hadrons into a state or states in which quarks and gluons could be considered unbound.

The phase diagram of strongly-interacting matter according to state-of-the-art QCD results is shown in Figure 1.2. Similarly to the phase diagram of water, the ordinate of the plot is temperature (T); the abscissa on the other hand is baryon chemical potential (μ_B), which is plays the role of water diagram's pressure. The following phases can be distinguished on the diagram:

- **Hadronic matter**, where all quarks and gluons are confined to hadrons. The short line and dot at $\mu_B \approx 900$ MeV and low temperatures indicate the first-order phase transition and critical point between two forms of such matter: nuclear liquid, known to be present in atomic nuclei around us, and a phase referred to as hadron gas (HG);

- **Quark-gluon plasma (QGP)**, which is a state consisting of deconfined quarks and gluons; the deconfinement is caused by high temperature of the system;

- **Normal quark (NQ)** matter, in which quarks and gluons become deconfined due to high pressure. Sometimes referred to as "cold plasma" in contrast to "hot" QGP. It is believed

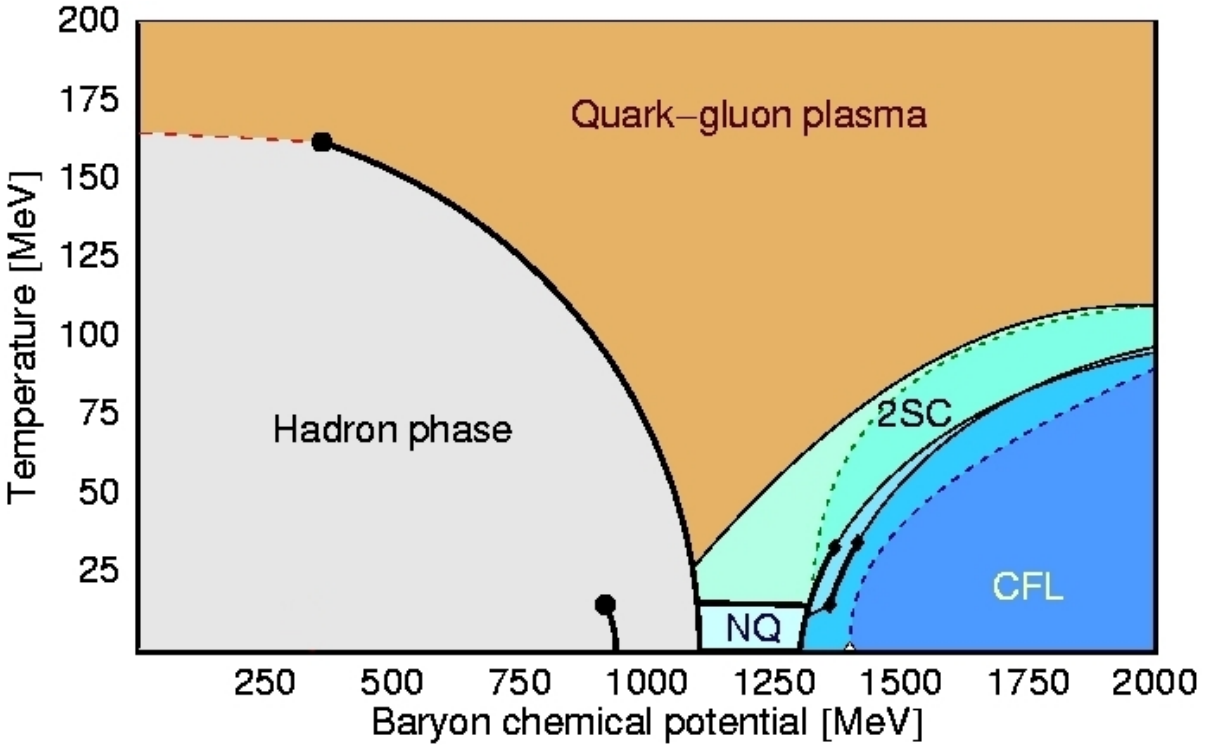

Figure 1.2: The state-of-the-art QCD phase diagram, with temperature as the ordinate and baryon chemical potential as the abscissa. Different areas of the diagram are marked with names of phases; see the text for explanation [6].

that matter of this state exists inside compact stellar objects, *i.e.* neutron stars or black holes;

- **Two-flavour Colour-Superconducting (2CS) matter** — the first state of strongly-interacting matter in which quarks form Cooper pairs, resulting in emergence of colour superconductivity. The term "two-flavour" refers to the fact that like nuclear matter around us, 2CS can be described using only two flavours of quarks: u and d [7];

- **Colour-Flavour-Locked (CFL) matter** — another superconducting state, with an interesting property: the colour a Cooper pair possesses in CFL is strictly correlated with its flavour content [8]. It is described by models involving three flavours of quarks (u, d, s) and is the highest baryon-density state of strongly-interacting matter postulated to exist by such models.

The final notable feature of the QCD phase diagram to be discussed here is the critical point expected to exist on the transition line between hadronic matter and quark-gluon plasma. Established and widely-accepted results from lattice-QCD calculations at $\mu_B = 0$ described the transition between HG and QGP as a second-order "cross-over" [9]. On the other hand, energy-scan results obtained by the NA49 experiment in the years 1998–2000 for baryochemical potential between 300 and 400 MeV, have been demonstrated to show consistency with expectations of

a first-order phase transition [10, 11] — implying existence of the aforementioned critical point where the transition order changes. These conclusions are supported by more recent lattice-QCD calculations at finite μ_B [12, 13]. In light of the above, programs are now underway at major particle-physics centres worldwide (light-ion runs at the SPS, low-energy runs at the RHIC, CBM experiment at the new FAIR centre in Germany, the proposed heavy ion-dedicated NICA facility in Russia [14, 15, 16, 17]) whose purpose is to experimentally validate existence of such a point by attempting to directly observe the critical point's properties.

1.2.3 The Big Bang and the Early Universe

Having already discussed the QCD diagram in general we shall now turn our attention to the phase most closely related to the subject of this dissertation, quark-gluon plasma. Unlike some forms of hadron gas or normal quark matter, QGP is thought not to exist naturally anywhere in the universe. However, it is also though it did exist in it at some point — right after the Big Bang.

According to the Big Bang theory, a cosmological model formulated in 1931 by Georges Lemaître[9] and so far thought to agree the best with gathered scientific evidence, our universe come into being — about 13.7 billion years ago, according to the latest data [18] — in explosive expansion of space-time from an initial state of immensely hot, uniform matter. As expansion progressed the density and the temperature decreased (see Figure 1.3), ultimately forming the atomic world in which we live. Therefore, if the phase diagram of strongly-interacting matter derived from quantum chromodynamics is correct there was a stage of the evolution of the universe at which it consisted of quark-gluon plasma — and as a result being able to somehow create and observe the properties of QGP would provide us with insight into our cosmogony.

1.3 Recreating Extreme Conditions: Collisions of Accelerated Particles

As it was mentioned before, only a small fraction of QCD states described in Section 1.2.2 is believed to exist naturally in our universe at this point in time — and even some of these cannot be accessed by scientists yet due to inhospitable conditions. Fortunately, humankind possesses technological means of creating some of normally-absent states artificially.

To move across the QCD phase diagram one needs to change the baryochemical potential and/or the temperature, similarly to how changing pressure and/or temperature allows one to move across the phase diagram of water. This however is where practical similarities between the two end: temperature and density scales of extreme QCD states are significantly higher than those available in the macroscopic world, and even if they weren't it would be impossi-

[9] Although the name itself was coined, later, by Sir Fred Hoyle.

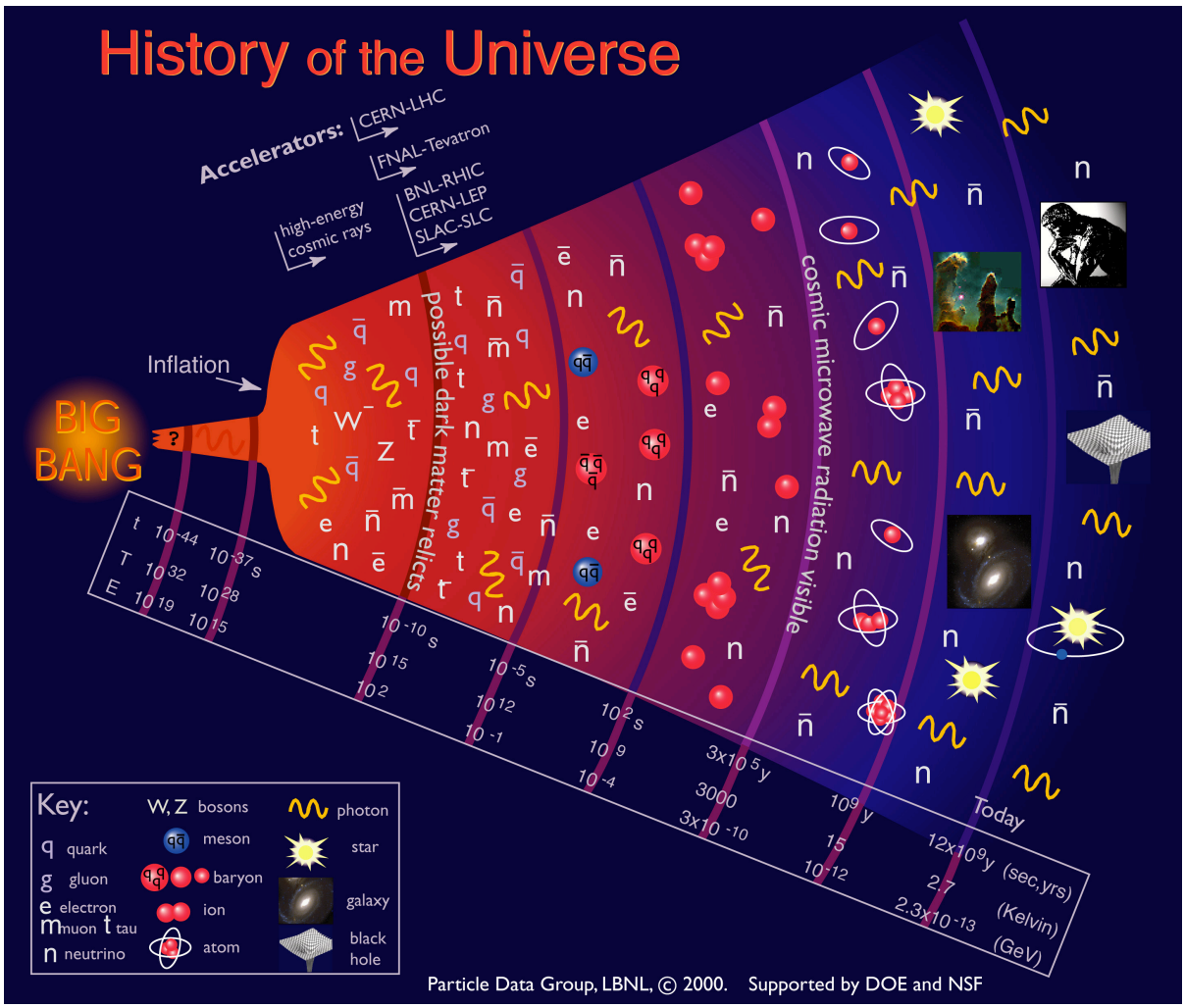

Figure 1.3: History of our universe

ble to employ macroscopic methods of transferring heat and applying pressure while working with subatomic particles. What *can* be done to reach hotter and more dense states of strongly-interacting matter in such particles is to provide them with kinetic energy in an *accelerator*, then force them to transform it into heat in a *collision*.

1.3.1 Particle Accelerators

One of the major issues early-day accelerator physicists had to deal with was that all atomic nuclei, which are the only readily-available repository of hadrons on Earth, possess positive electric charge — meaning that if two of them are to collide electric repulsion needs to be overcome before they get close enough to each other to interact strongly. How big an effect this repulsion can have was shown in 1911 by Hans Geiger and Ernest Marsden, in what is now known as the Rutherford experiment: α particles encountering gold nuclei were significantly deflected from their original trajectories and in some cases were even forced back to where they came from [19]. Eventually however this initial problem turned out to be a blessing in disguise,

as the very same electric charge was soon discovered to be useful for accelerating charged particles by sending them through an electric field — which has been the general principle behind accelerators ever since.

The first particle accelerator dedicated to smashing atoms[10], a single-stage linear device made out of a high-voltage transformer and a discharge tube, was built in 1930 at the Cambridge University by John Cockroft and Ernest Walton. An upgraded, more powerful version of this device was used in 1932 to propel protons at a lithium target in what became the first accelerator-driven atomic fission experiment in the world. Meanwhile, on the other side of the Atlantic Ernest Orlando Lawrence was working on constructing a cyclotron, which allowed more efficient acceleration of particles by using magnetic fields to repeatedly redirect particles back into the electric field. This work began in 1929, resulted in a proof-of-concept device (about 4 in in diameter, with top kinetic energy of 80 keV) and led to Lawrence reproducing Cockroft and Walton's experiment, using an 11-inch cyclotron, mere three months after the original. Ever since the domain of accelerator design has been making steady progress, overcoming leading up to large, ultra high-energy devices of today.

Table 1.1 shows a list of chosen historic, currently-active and future particle accelerators along with some of their properties.

Fixed-target and Collider Set-ups

In a collision event one typically refers to one particle as a projectile and the other as a target. This division is traditional, as the earliest experiments of this kind used accelerated particles to bombard stationary targets, clearly distinguishing the two classes. Experiments in this configuration are called *fixed-target*.

In contrast to the above, in 1960s Burt Richter and other Stanford physicists began investigating the viability of a different set-up — with *two* beams circulating in opposite directions and colliding at intersection points. Obviously, such a configuration implies a number of challenges that need to be addressed: a *collider* must be able to accelerate two beams at the same time, more precise control is necessary to achieve good interaction rates and so on. Then again, these are also many advantages — most notably the centre-of-mass collision energy in a collider experiment is significantly (*i.e.* by approximately $\sqrt{2E_{lab}}$) higher comparing to using the same kinetic energy in a fixed-target experiment and that it is much easier then to provide uniform detector coverage of the interaction point. In a collider distinction between projectiles and targets becomes arbitrary and is usually specified by convention, either by basing it on what particles are collided (especially for asymmetric systems) or simply by assigning each name to a specific beam of the accelerator.

After the advantages of colliding two accelerated beams became well-visible in the advent of Stanford's SPEAR, the new approach quickly established itself in the field and now the most

[10] Which, however, didn't succeed as a smasher due to acceleration energy being too low to penetrate the target nuclei.

Name	Site	Launched	Geometry	Size	Particles	E_k (e/p)	Comments
Wideröe linear accelerator [20]	Aachen (Germany)	1928	linear	88 cm	K^{X+}, Na^{X+}	50 keV	Proof of concept
Cockroft-Walton accelerator [21]	Cambridge (UK)	1932	*complex*	2.4 m	p	0.8 MeV	The first accelerator to split the nucleus
11-inch cyclotron [22]	UC Berkeley (USA)	1932	circular	$\approx$ 40 cm	p	1 MeV	Cost: $\approx$ 25 USD (present-day 1000 USD)
Cosmotron [23]	BNL (USA)	1953	circular	72 m	p	3.3 GeV	The first running synchrotron
Dubna Synchrophasotron [24]	JINR (USSR)	1957	circular	208 m	p, light ions	10 GeV	
SLAC Linac [25]	Stanford (USA)	1966	linear	3 km	$e^{\pm}$	30 GeV	
Stanford Positron Electron Asymmetric Ring [26]	Stanford (USA)	1972	circular	255 m	$e^{\pm}$	1.5 GeV	The first running collider
Super Proton Synchrotron [27]	CERN	1976	circular	6 km	$p/\bar{p}$, $e^{\pm}$, Pb^{X+}	450 GeV	
Tevatron [28]	Fermilab (USA)	1983	circular	6.3 km	$p/\bar{p}$	0.9 TeV	
Relativistic Heavy Ion Collider [29]	BNL (USA)	2000	hexagonal	3.8 km	p, d, Cu^{X+}, Au^{X+}	250 GeV	
Large Hadron Collider [30]	CERN	2008	circular	27 km	p, Pb^{X+}	7 TeV	Cost: $\approx$ 3,000,000,000 EUR
International Linear Collider [31]	*TBD*	2015-2020?	linear	30-40 km	$e^{\pm}$	0.5 TeV	Proposed

Table 1.1: Properties of chosen historic, currently-active and future particle accelerators, sorted by the year of commissioning.

powerful particle accelerators in the world are almost invariably colliders; on the other hand, fixed-target accelerators and experiments remain widespread and show no sign of being phased out. Interestingly enough, certain machines could and at times did operate in both modes — for example, despite having originally been designed as an accelerator for fixed-target experiments and being still used for this purpose, CERN's SPS spent a large part of the 1980s colliding protons with anti-protons.

Collisions of Atomic Nuclei

As partially illustrated by Table 1.1, the number of different species of particles that get accelerated and collided is quite large. In this section I would like to devote particular attention to projects and facilities accelerating and colliding a specific kind of such particles — atomic nuclei.

Even though the first particle accelerator in the world, the proof-of-concept device of Rolf Wideröe, accelerated sodium and potassium ions, a long time had to pass before particles larger than deuterons began to be accelerated for collision purposes. The first research facility to initiate such a program was the Soviet JINR, whose Synchrophasotron was proposed to be upgraded for acceleration of nuclei heavier than hydrogens in 1969. The upgrades were carried out in early 1970s and culminated in, near the end of the decade, the machine being able to accelerate helium, carbon, oxygen and neon nuclei up to $\sqrt{s_{NN}}$ = 4.1 GeV. Meanwhile, similar work was underway at the Lawrence Berkeley Lab in the United States to upgrade its venerable Bevatron for nucleus acceleration; first ion beams were produced in 1971, whereas in 1974 the machine was connected to the SuperHILAC linear accelerator which would operate as Bevatron's ion injector, forming the Bevalac. Basic nucleus–nucleus physics programs of the two facilities were quite similar, involving studies of behaviour of compressed hadronic matter; however, JINR experiments concentrated on hard scattering and quark-parton structure functions of the nuclei whereas LBL focused its attention on such matter's equation of state along with properties of post-collision expansion. Moreover, both facilities performed (unsuccessful) searches for signals of the phase transition. Last but not least, the Dubna Synchrophasotron also featured experiments searching for exotic hadronic states, whereas the Bevalac had its beams used for the purposes of radiotherapy [32, 33].

Also worth noting at this point is CERN's Intersecting Storage Rings (ISR) collider, which in 1980 and 1983 accelerated helium ions for the purpose of $\alpha + \alpha$ and $p + \alpha$ collisions at then remarkably high $\sqrt{s_{NN}}$ of up to 31 and 44 GeV, respectively [34]. Then again, it never accelerated any nuclei heavier than helium and was decommissioned soon afterward.

The next generation of accelerators featuring experiments with nucleus–nucleus collisions consisted of the Alternating Gradient Synchrotron (AGS), commissioned at the Brookhaven National Laboratory in the US in 1960, and the Super Proton Synchrotron (SPS), launched at CERN in 1976. Similarly to the Dubna Synchrophasotron and the Bevalac, the two machines began their lives as proton accelerators and were later adapted to accelerate heavier ions: fol-

lowing a period of machine development, in 1986 the AGS and the SPS became capable of accelerating ions up to silicon to $\sqrt{s_{NN}}$ = 5 GeV and up to sulphur to $\sqrt{s_{NN}}$ = 20 GeV, respectively [35]. This time, searching for quark-gluon plasma was clearly defined as the primary physics goal of the two programs, involving several experiments based on different detectors (*e.g.* E802, E810, E814 or E858 at the AGS; NA34/2, NA35, NA36, NA38 or WA80 at the SPS) in order to address large uncertainties of theoretical predictions as well as conclusions of earlier experiments [36, 37].

Commissioning of the AGS booster in 1993 and of a new injector linac at CERN in 1994 marked the beginning of another stage of nucleus–nucleus collision physics by allowing the two synchrotrons to accelerate, for the first time, truly heavy ions such as gold (AGS; top energy $\sqrt{s_{NN}}$ = 4 GeV) and lead (SPS; top energy $\sqrt{s_{NN}}$ = 17.3 GeV). At the AGS, gold-beam studies were performed by the same experiments as before, along with E859 which eventually succeeded E802. On the other hand, CERN initiated a whole new series of experiments dedicated to heavy-ion studies — among them the experiment constituting the subject of this dissertation, NA49 [38, 39]. All of these experiments have already finished taking data but some of them are still active analysing it; moreover, many of their results have been interpreted as evidence of production of quark-gluon plasma and the onset of deconfinement at the SPS.

The last year of the XXth century saw the launch of the Relativistic Heavy Ion Collider at the BNL. This device has been unique not only due to its high top collision energy, $\sqrt{s_{NN}}$ = 200 GeV, but also due to the fact it has been the first and so far the only particle accelerator dedicated to heavy ions — out of five experiments at the RHIC, four (the smaller BRAHMS and PHOBOS, along with the larger PHENIX and STAR) have been built specifically to observe collisions of gold nuclei [40, 41, 42, 43]. All four experiments remain active, with PHENIX and STAR still taking data on a yearly basis, and have produced important results pertaining to production of quark-gluon plasma; some of these results will be touched upon in this dissertation.

Finally, the youngest and most powerful to date accelerator of heavy ions is the Large Hadron Collider at CERN, officially launched in September 2008 and expected to achieve readiness for physics data-taking in the spring of 2009. Lead ions will be collided at the LHC at the energy of $\sqrt{s_{NN}}$ = 5.5 TeV — almost 30 times as high as at the RHIC; QGP produced at this energy is expected to exist long enough to allow extremely accurate measurement of its properties. Although the LHC is dedicated primarily to high-energy p+p collisions and only one of its four experiments, ALICE, is heavy ion-specific, the other two large ones (ATLAS and CMS) also feature heavy-ion physics programs [44, 45, 46].

1.3.2 Nucleus–nucleus Collisions

Unlike collisions of individual hadrons or leptons, where both the projectile and the target are almost point-like, colliding nuclei involves objects of non-negligible dimensions and mass, as well as — in some cases — non-trivial shapes; this is particularly the case for nuclei such as gold,

lead, uranium and so on, commonly referred to as *heavy ions*, which weigh over two hundred times more than a single nucleon. Moreover, one could intuitively expect collisions of such compound objects to exhibit properties not observed in the case of leptons or single hadrons. On the other hand, both single hadrons and atomic nuclei do ultimately consist of quarks…How exactly, then, will such a system behave in a collision?

Phenomena in an *A*+*A* Collision

Basing on a combination of theoretical predictions and empirical observations, we are able to formulate a number of hypotheses pertaining to be behaviour of matter in nucleus–nucleus collisions. In particular, it is possible to divide phenomena occurring in such events into several classes.

To begin with, a large number of effects can be explained by simple quantitative scaling of elementary collisions. The elementary system in question is typically nucleon–nucleon (which can be approximated by p+p interactions at high-enough energy), with the scaling based on the number of, depending on the effect and the model in question, either participating nucleons or binary nucleon–nucleon collisions. The ability of performing such a factorisation quite advantageous: on one hand small systems such as p+p events may be easier to understand than larger ones, on the other it facilitates comparing the latter to the former. A good example of a practical implementation of this approach is the wounded-nucleon model, in which particle yields are assumed to be proportional to the number of wounded (participating) nucleons [47]; this model in turn has been based Glauber model, discussed in Section 1.4.2.

Moving on the effects present in nucleus–nucleus events which cannot be described with such a factorisation, one can of course begin with *hot* strongly-interacting matter phenomena, which are related to the matter's equation of state, its phases and transitions between them. According to state-of-the-art knowledge such phenomena occur in particular in collisions of heavy ions such as gold, lead or uranium and as such do not appear in p+p interactions. Specifically, concerning transitions from hadron gas to quark-gluon plasma, there are in fact two such transitions expected to take place: chiral symmetry restoration as a result of quarks becoming essentially massless, and the deconfinement itself. The two are expected to take place very close to each other, however whether this happens at exactly the same time or not remains open. Last but not least, it is possible that plasma itself changes properties with increasing energy: although it is still expected that the QGP observed by LHC experiments will be a weakly-interacting, gas-like state similar to electromagnetic plasmas which gave it its name, results obtained in recent years at the RHIC are consistent with the picture of a *strongly*-interacting medium, more like a low-viscosity liquid than like a gas. In order to make a clear distinction between the two forms of the deconfined phase, such a "perfect liquid" is typically referred to as **sQGP**.

Another hot matter effect occurring in nucleus–nucleus collisions is *flow* — collective motion of particles as a result of pressure gradients produced in a collision. In particular, peripheral interactions feature flow which is anisotropic. Its origin is purely geometric and can be seen in

Figure 1.4: spatial anisotropy of the interacting volume translates into anisotropy of momentum, resulting in non-uniform production of particles with respect to the reaction plane. This non-uniformity is typically described in terms of coefficients of its Fourier expansion (Ψ_r is the azimuthal position of the reaction plane):

$$\frac{\mathrm{d}N}{\mathrm{d}(\phi - \Psi_r)} = 1 + 2\sum_{n=1}^{\infty} v_n cos[n(\phi - \Psi_r)]. \tag{1.1}$$

The contribution of terms higher than the fourth is very small and they are typically omitted. On the other hand, in a symmetric collision system all odd terms of the expansion equal zero. Therefore, the terms that are of foremost significance in physics analyses are the second, often referred to as *elliptic flow*, and the fourth one. In case of asymmetric systems such as *p+Pb* or *d+Au* the first term, *directed flow*, is considered as well.

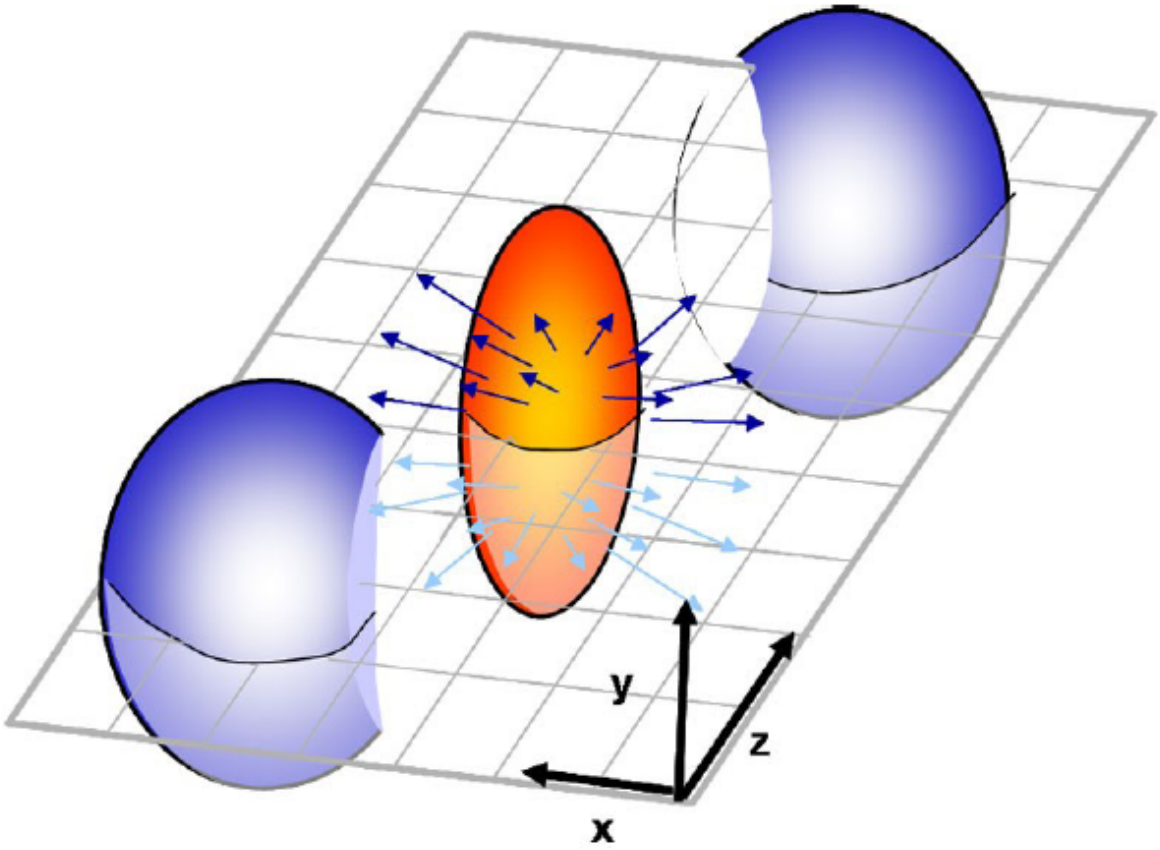

Figure 1.4: Schematic illustration of the origin of flow. See the text for a description [48].

Next, there are of course effects other than hot nuclear matter ones which cannot be explained through factorisation. To begin with one needs to take into account the so-called *cold* nuclear matter (CNM) effects [49]. These can be divided into two classes. First of all, parton density functions are different in bound nucleons than in free protons and neutrons; this results in the phenomena of *shadowing* (which, roughly speaking, amounts to nucleons in front of the target

hiding the ones in the back from the incoming projectile), anti-shadowing and the EMC effect. On the other hand, cold nuclear matter can "get in the way" of outgoing particles and cause their *absorption*. Both of these classes are relatively well understood theoretically.

Last but not least, it has been known since mid-1970s that transverse-momentum spectra from nucleon–nucleus and central nucleus–nucleus collisions are enhanced in the range of intermediate p_T with respect to those from nucleon-nucleon events [50]. This phenomenon, dubbed the *Cronin effect* after its discoverer, is hypothesised to be related to multiple scattering of partons in nuclear matter but generally remains something of an unknown from theoretical point of view.

Colour Glass Condensate In two papers published in 1993 Larry McLerran and Raju Venugopalan introduced a new approach to calculating properties of the initial state of nuclear matter in relativistic collisions of heavy nuclei, using quark and gluon density functions [51, 52]. As this approach evolved it became visible that the matter in question can be said to achieve a new state: a strongly Lorentz-contracted, dense wall (sheet) of gluons. This new state was named *Colour Glass Condensate*: "colour" because gluons possess colour charge, "condensate" because of its density and "glass" because of its similarity to common silicon glass — possessing properties of a solid in short time scales but acting like a liquid in the long run.

As the theory of CGC is quantum, applying it to nuclear collisions is much more complicated than the Glauber model. Then again, models based on Colour Glass Condensate have recently been shown to describe quite well cold nuclear matter effects, and to some degree — Cronin enhancement, in such collisions. A detailed discussion of properties of this approach, which would be beyond the scope of this dissertation, can be found here: [53].

Stages of a Collision

Regardless of system size it is physically impossible for everything in a collision to happen at exactly the same time, and for such large objects as heavy nuclei this isn't even approximately the case. An inelastic nucleus–nucleus collision can be divided into a number of distinguishable stages discussed below.

Note: As the properties of a point of the system during a collision depend not only on elapsed time, t, but also on the point's distance from the interaction point along the beam axis, z, chronology of a collision is based on *proper time*: $\tau = \sqrt{t^2 + z^2}$. Also, for convenience of illustration we consider the system in the centre-of-mass frame.

1. **Initial state** — the two nuclei head towards each other. As a result of travelling at relativistic velocities they are highly Lorentz-contracted in the beam direction, appearing to the observer as almost-flat "pancakes";

2. **Early stage** — constituents of the two nuclei interact, producing new quarks and gluons as well as changing properties of existing ones. Any hadrons and leptons, both stable and

unstable, produced at this stage are called *primary*;

3. **Expansion** — the matter begins to expand as a result of pressure gradient between it and the surrounding vacuum, much like a fireball from a chemical explosion. Particles produced at the previous stage can now interact, both inelastically (*i.e.* changing numbers of particle species) and elastically. Last but not least, this stage witnesses first decays of unstable particles;

4. **Freeze-out** — a point or points in proper time marking the end of particles' interactions. Two types of freeze-out are distinguished:

   - chemical freeze-out — marks the end of all inelastic interactions, thus fixing the yields of particles produced by the fireball[11];
   - kinetic freeze-out — marks the end of all elastic interactions, thus fixing the particles' momentum.

   The two are expected to occur separately, with chemical freeze-out obviously preceding the kinetic one. Then again, certain theoretical considerations can be accurate enough — while much easier to accomplish — with single freeze-out time [54];

5. **Final state** — In addition to all interactions having already ceased to take place, all or all but the most long-lived unstable particles have already decayed into their final, stable products. This is the stage seen by particle detectors.

State of Early-stage Matter

In the previous section, the early stage was considered only in the context of interactions of individual particles. This time on the other hand, we shall discuss its matter in bulk. A typical approach to describing systems of particles this way is to use the language of *thermodynamics* and this is the method we shall apply in this case as well. Note that in order for us to be allowed to take advantage of this approach early-stage matter must be close to equilibrium — which, luckily, is believed to be the case.

Thermodynamically speaking, a relativistic system can be characterised by temperature and baryochemical potential. Values of these two quantities determine the state of this system. Now, while considering the aforementioned early stage of a collision one additional variable appears: *energy density* resulting from deposition of collision's energy into the system's volume. This energy density forces a rapid change of the system's thermodynamic properties, placing it in a different region of the phase diagram and defining the phase of its matter. In case of strongly-interacting matter, Section 1.2.2 of this dissertation tells us that in light of the above, early-stage matter can be a hadron gas, quark-gluon plasma or a mixture of the two.

[11] Total yields may still be changed as a result of decays.

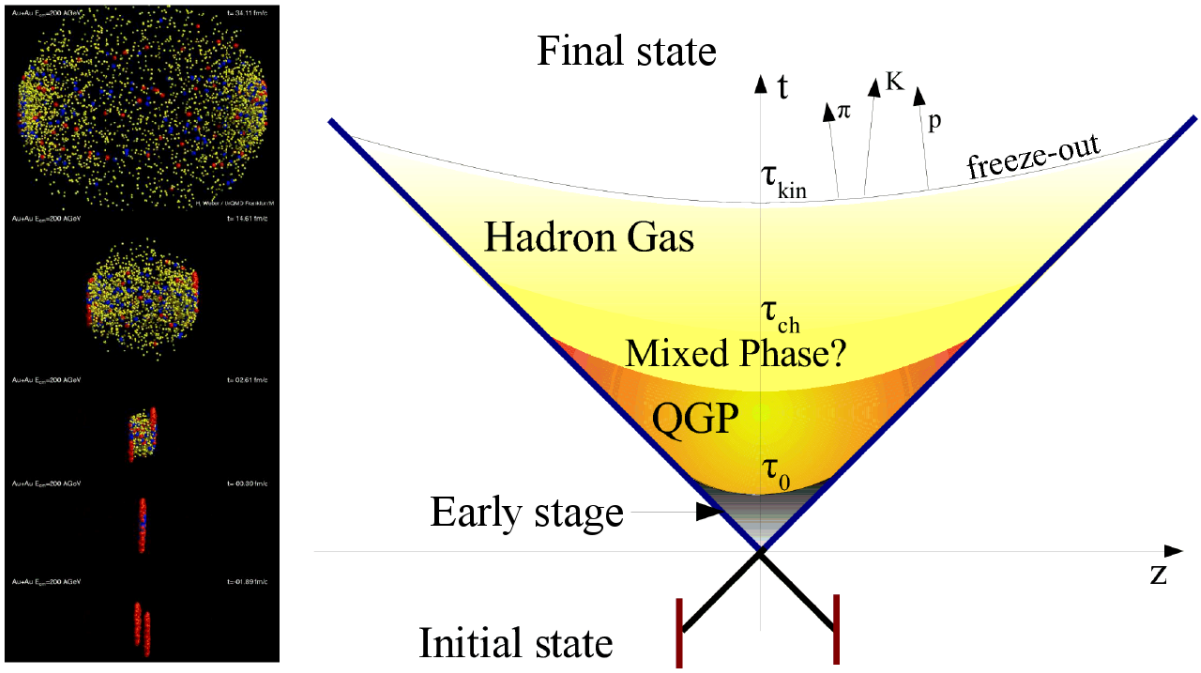

Figure 1.5: Different stages of a nucleus–nucleus collision: visualisation of a simulated event (left) and a space-time diagram (right). See the text for discussion of each of the stages.

Naturally, state of the early stage can affect progress of expansion. Depending on thermodynamic properties of the former, the latter follows one of the following three paths:

1. Early stage is a **hadron gas** — expansion simply dilutes the gas with no qualitative changes of its properties in the process;

2. Early stage is **quark-gluon plasma**, μ_B is **low** — the system evolves from the QGP phase into hadron gas, with a smooth transition (cross-over) between the two;

3. Early stage is **quark-gluon plasma**, μ_B is **high** — the system evolves from the QGP phase into hadron gas, with the first-order phase transition in the process resulting in emergence of a mixed phase between the two.

1.3.3 Experimental Detection of Phase Transition

Of course with the lifetime of 10^{-22}–10^{-23} s and the drop size in the range of single femtometres, it is impossible to observe quark-gluon plasma directly. Regardless of what happens in an event at its early state or during expansion, only the final state can be observed by detectors. Therefore, the only way to gain access to early-state matter is to take what final-state observables are available and, using models and theoretical calculations, "trace them back" to their origins.

Two experimental approaches can be applied to searching for quark-gluon plasma. The first involves searching highest-energy heavy-ion events, in which we expect the QGP to be formed,

for a number of *probes* — phenomena which, in spite of the fact each of them occurring by itself could be explained by alternative hypotheses, could when occurring together be considered evidence for plasma's presence. A number of different probes has been proposed: modification of properties of jets (this probe will be discussed in more depth in Section 1.4.4), suppression and/or recombination of particles consisting of heavy quarks, chiral symmetry restoration along with its effect on yield of certain hadrons, changes in production of thermal photons and other effects. Appropriate quantities related to those probes are typically compared to scaled results from more elemental collision systems, either real or simulated.

The other possible approach on the other hand concentrates on searching for the phase transition between hadron gas and quark-gluon plasma rather than for the QGP itself. It takes advantage of the monotonic relationship between early-stage energy density and the collision energy provided by the accelerator. With that in mind, the transition could in principle be detected by performing an *energy scan* of some specific observable and looking for sudden and/or radical changes in its behaviour. This quite naturally requires more data sets to be collected than the first case and, given the phase space must be sampled on both sides of the transition region, limits the use of this methods to machines providing appropriate range of collision energy (such as the RHIC after recent upgrades or the SPS); on the other hand, energy scans do not need to track as many variables as probes (which, as mentioned above, must be observed simultaneously to be conclusive) and are somewhat less model-dependent (the only major assumption that has to be made here is that the variable in question is affected by the phase transition). A number of different observables is suitable for energy-scanning, including correlation functions used in the project described in this dissertation.

Both of these approaches have already been used in heavy-ion experiments. Among present-day experiments, probes have mostly been employed at the RHIC (see *e.g.* [55, 56, 57], as well as jet-modification results presented in Section 1.4.4) and will be used at the LHC, then again they have also been used in some analyses at the SPS (see *e.g.* [58]). Energy scans on the other hand have mostly been the domain of SPS experiments — in particular of NA49, whose results on energy dependence of production of certain hadrons show a number of structures (the "horn" in kaon-to-pion ratios, the "kink" in pion yield and the "step" in the inverse-slope parameter of kaon m_T spectra) whose presence is consistent with prediction of the onset of the deconfinement phase transition [10, 11].

1.4 Hard Processes

As available collision energies became larger and larger a number of interesting phenomena was discovered to occur in high-energy events:

1. **Deep Inelastic Scattering** (DIS) in ep collisions. The first of such phenomena to be observed, in late 1960s at the Stanford Linear Accelerator Centre. Electron-scattering

experiments at SLAC observed a threshold of e-beam energy beyond which the deflection angle of scattered electrons became significantly larger, whereas the proton target would disintegrate into lighter, high-p_T particles instead of simply recoiling [59];

2. Unlike their less energetic counterparts, which are distributed uniformly in azimuth, high-p_T particles produced in both leptonic and hadronic collisions tend to "cluster together", forming highly collimated bunches called **jets** — which in turn tend to appear in azimuthally back-to-back pairs often referred to as *dijets*. A good illustration of this phenomenon can be found in Figure 1.6;

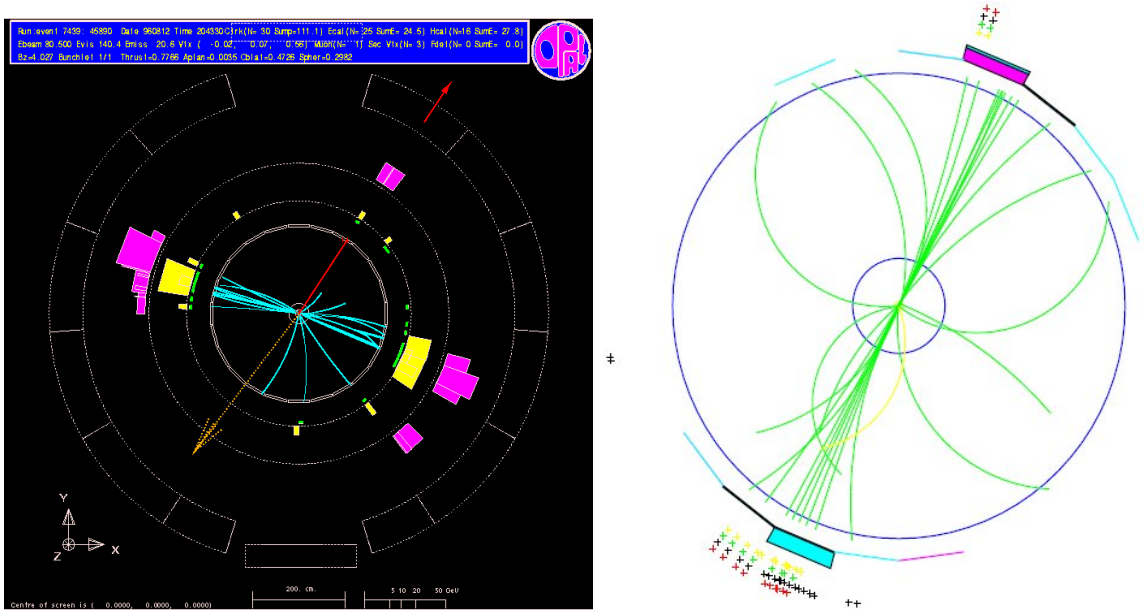

Figure 1.6: Two-jet events observed in e^+e^- collisions at 161 GeV at LEP (left) and in $p\bar{p}$ collisions at 1.8 TeV at the Tevatron (right) [60, 61].

3. **Power-law p_T spectra and m_T yield** in pp and $p\bar{p}$ collisions. Early experiments in the field have shown basic properties of hadron production in such collisions to approximately follow the principles of statistical mechanics, as such both the transverse momentum spectra and the transverse mass yields follow the Boltzmann distribution,

$$\frac{\mathrm{d}n}{\mathrm{d}x} \propto exp(-\frac{x}{T}), \tag{1.2}$$

with an additional cut-off resulting from finite collision energy. However, it has been shown by more recent experiments at the CERN ISR and Fermilab that this is only the case for $p_T \leq 2\ GeV/c$ or $m_T \leq 2\ GeV/c^2$; above these thresholds both transverse momentum spectra and transverse mass yields begin to deviate from the exponential and

instead follow the power-law form,

$$\frac{\mathrm{d}n}{\mathrm{d}x} \propto x^{-P}, \tag{1.3}$$

also cut off by finite collision energy. For an overview of these results, see [62].

At the time of discovery of DIS the origin of such effects was entirely unknown. Soon afterwards however, in 1967–1969, James Bjorken and Richard Feynmann proposed a theory which explained the change in scattering by allowing protons to have internal structure [63, 64, 65]. This was late shown to be correct and in agreement with the recently-introduced quark theory, despite initial conflict of properties between Feynmann's *partons* and Gell-Mann's quarks (which was later removed by the discovery of asymptotic freedom). In reference to high transverse momentum of the particles involved, all processes believed to originate from interactions with individual quarks have been assigned the moniker "hard".

Let us at this point discuss in slightly more detail, as relevant to the subject of this dissertation, a later model of hard scattering, introduced by Feynman and Field in 1976 in an attempt to address the power-law behaviour of high-p_T particles produced in pp/$p\bar{p}$ collisions and the phenomenon of jets therein [66]. The approach they have presented was to treat non-elastic hadron–hadron collisions as elastic collisions of their constituent partons, at that point already recognised as quarks and/or gluons. This can be qualitatively described as (also see Figure 1.7)

$$E\frac{\mathrm{d}\sigma}{\mathrm{d}^3p}\,(s,t,u;A+B\to h+X) \propto G_{h\to q/g}(x) \times \frac{\mathrm{d}\hat{\sigma}}{\mathrm{d}\hat{t}}(\hat{s},\hat{t};q_a+q_b\to q_c+q_d) \times D^h_{q/g}(z), \tag{1.4}$$

where

$\hat{s} = (p_a + p_b)^2$;

$\hat{t} = (p_a - p_c)^2$;

$x = \frac{p_{q/g}}{p_h}$;

$z = \frac{p_h}{p_{q/g}}$;

$G_{h\to q/g}(x)$ is what is typically referred to nowadays as parton distribution function (PDF) and was named the source function in the original paper, describing the probability of the quark/gluon q/g at given x to appear in the initial hadron h;

$D^h_{q/g}(z)$ is the so-called fragmentation function (FF), describing the opposite situation - probability of the scattered quark/gluon q/g fragmenting into the final hadron h with given z;

$\frac{\mathrm{d}\hat{\sigma}}{\mathrm{d}\hat{t}}(\hat{s},\hat{t};q_a+q_b\to q_c+q_d)$ is the cross-section for the elastic scattering of partons as a function of the reaction's energy ($\hat{s}$) and momentum transfer ($\hat{t}$).

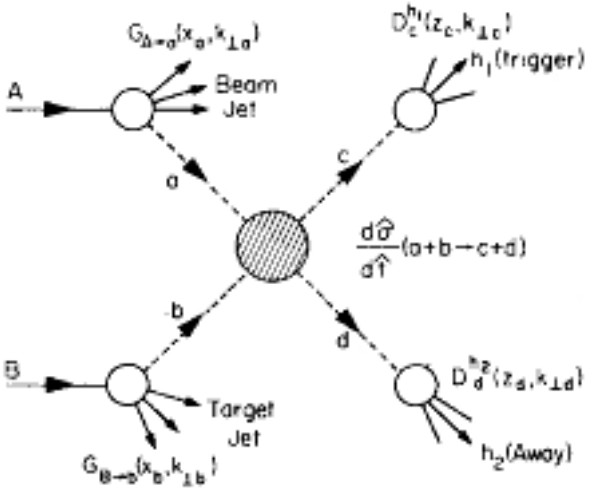

Figure 1.7: Feynman and Field's illustration of the common underlying structure of "hard-scattering" models of hadron-hadron collisions [66].

In the initial versions of their model Feynman and Field used data from ep and νp collisions and e^+e^- annihilation as a basis for determining the properties of source and fragmentation functions, whereas the quark-quark scattering cross-section (at the time no gluons were considered in the model) involved a black-box function chosen simply to match experimental results. Despite this, the model performed reasonably well predicting both high-p_T single-particle spectra and, after the introduction of certain additional corrections (see [67]), correlations between them, *i.e.* jets. Eventually however, the phenomenological definitions of the model's components have been superseded by ones based on prediction of the recently-introduced theory of quantum chromodynamics — elegantly completing the quark and gluon-based image of *hard scattering* with a realistic description of strong interactions which govern it [68].

1.4.1 Jets in the Hard-scattering Model

According to the model proposed by Feynman and Field, high collimation of jets is a result of a single jet originating from fragmentation of a single parton: local momentum conservation prevents fragmentation products from deviating too strongly from their parent's trajectory. Local momentum conservation is also the cause of back-to-back orientation of dijets — jets originating from two partons which participated in the same scattering — in the transverse plane, even though presence of other particles in a collision (*i.e.* global momentum conservation) means they do not necessarily have to be back-to-back in pseudorapidity.

As a parton in the hard-scattering model can be either a quark or a gluon, one can divide jets into quark and gluon ones depending on what type of parton they originate from. The two types possess significantly different properties, moreover the probability of producing a gluon jet and not a quark one is expected to depend on collision energy [68]. Unfortunately, as both

types of jets ultimately consist of the same kind of particles, no experimental means exist yet which would allow us to distinguish the two.

1.4.2 From Hadron–hadron to Nucleus–nucleus Collisions

As it could be seen above, the theory of hard scattering has been developed entirely for *p*+*p* collisions. Therefore, before we move on to the subject of how hard processes affect or are affected by a medium of deconfined quarks and gluons it will be necessary to formulate the rules of extending their theory into the realm of nucleus–nucleus collisions. This can be achieved by reversing the factorise-into-elementary-collisions approach touched upon in Section 1.3.2; on the basis of the factorisation theorem ([69]) for hard processes in perturbative QCD, they are expected to scale with the number of binary nucleon–nucleon collisions. The most common and widely-established approach to performing such a scaling is the so-called *Glauber model*.

The Glauber Model

The Glauber model was developed in the late 1950s by the 2005 Nobel Prize in Physics laureate Roy Glauber [70]. It addresses a number of issues which make it impossible to approximate collisions of complex systems using a simple geometric description, in particular: the fact that due to their quantum nature, nucleons are "spread" over nuclear volume rather than exactly localised in it, and the fact the combination of quantum effects and the range of electromagnetic and nuclear-force fields generated by nucleons makes the boundary of a nucleus "fuzzy", causing the nucleus to be effectively larger than geometry would imply. That aside, it remains a fairly simple and elegant solution which, if one is aware of its limitations — the most severe being the model assumes constant interaction cross-section and straight-line trajectories of nucleons regardless of how many elementary interactions they participate in, which is known not to be generally true — can even nowadays be useful for describing complex collision systems.

The basis of the Glauber framework is a geometric approach, as illustrated by Figure 1.8. However, rather than being localised all nucleons are distributed randomly across the participating nuclei and can only be described in terms of nuclear density profiles. For large nuclei, one typically employs the Woods-Saxon density function,

$$\rho_A(r) = \frac{\rho_0}{A\left(1 + exp\left[\frac{r-r_0}{a}\right]\right)}, \tag{1.5}$$

with the parameters r_0, a and ρ_0 and where $r = \sqrt{s_A^2 + z_A^2}$. With all this in mind and stepping up from more simple to more complex systems, one can define the nucleus–nucleus *thickness*

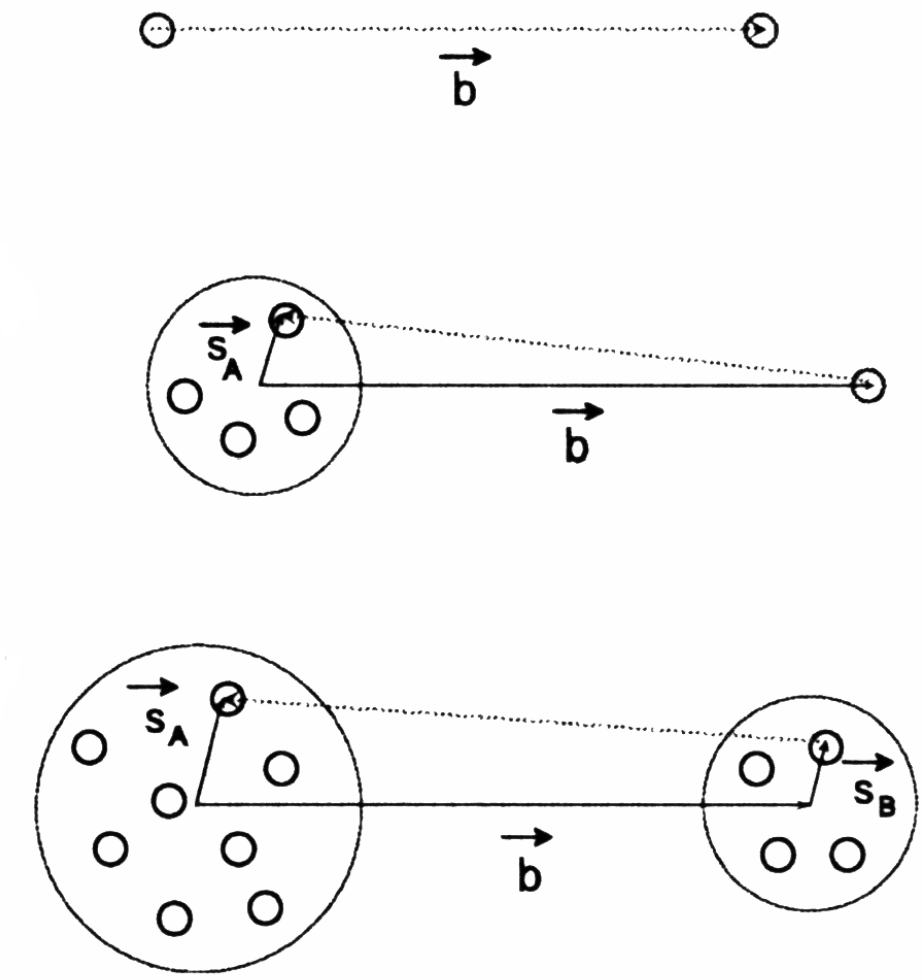

Figure 1.8: A diagram of nucleon–nucleon (top), nucleon–nucleus (middle) and nucleus–nucleus collisions, in the plane perpendicular to the beam axis, as seen from the point of view of the Glauber model. $\vec{b}$ is the impact parameter vector (distance between the two beams), whereas $\vec{s}_A$, $\vec{s}_B$ describe position of a nucleon inside nucleus A or B, respectively [71].

function:

$$T_{AB}(\vec{b}) = \int \mathrm{d}z_A \int \mathrm{d}^2 s_A \rho_A(\vec{s}_A^{\,2}, z_A^2) \int \mathrm{d}z_B \int \mathrm{d}^2 s_B \rho_B(\vec{s}_B^{\,2}, z_B^2) t(\vec{b} + \vec{s}_B - \vec{s}_A), \qquad (1.6)$$

$$\int \mathrm{d}^2 b T_{AB}(\vec{b}) = 1,$$

where $t(\vec{b})$ is the nucleon–nucleon thickness function, which in the limit of point-like nucleons takes the form $t(\vec{b}) \to \delta^{(2)}(\vec{b})$.

The thickness function allows one to calculate a wide range of quantities useful for scaling nucleon–nucleon collisions up to nucleus–nucleus ones. First of all, the probability of having n inelastic binary nucleon–nucleon collisions (with cross-section σ_{in}) in a nucleus–nucleus colli-

sion at the impact parameter $\vec{b}$ can be defined as

$$P(n; AB; \vec{b}) = \left(\binom{AB}{n}\right) \left[1 - T_{AB}(\vec{b})\sigma_{in}\right]^{AB-n} \left(\left(\binom{AB}{n}\right)\right) \left[T_{AB}(\vec{b})\sigma_{in}\right]^{n}, \tag{1.7}$$

which in turn makes it possible to use standard formulae to obtain the average number of such collisions along with its dispersion — the information needed to scale hard processes from *p*+*p* to *A*+*A* events. It is also possible to calculate the cross-section of a nucleus–nucleus collision, the number of nucleons participating in such a collision and so on. Last but not least, one can apply results of these calculations to establish a relationship between the impact parameter, which as it can be seen has got precise theoretical meaning, and experimentally-measurable centrality of a collision.

1.4.3 Experimental Detection of Jets

Given the collimated nature of jets it could naively be expected locating them in an event to be fairly straightforward. To some degree this is indeed the case, as in elementary collision systems such as *p*+*p* or $e + p$ they could often even be selected by hand — however, the situation is dramatically more difficult for more complex systems and even in the simple ones automated solutions are needed in order to evaluate large amounts of data in reasonable time. Consequently, a number of different solutions are employed for this purpose.

First of all, dedicated algorithms have been developed which can go over particle tracks in an event and assign them (or not) to different jets. There are two general classes of jet-reconstruction algorithms: *cone* and k_T, each of them consisting of multiple variants [72]. The former are in a nutshell automated versions of picking jets by eye: a cone is drawn in space (possibly, although not necessarily, starting from a high-p_T seed particle) and updated iteratively until the position of its centroid becomes stable. The latter on the other hand take advantage of very small differences in the momentum component perpendicular to jet axis, between particles belonging to a single jet. Both methods have got their advantages and drawbacks (for instance, cone algorithms make *a priori* assumptions about the shape of a jet, whereas k_T ones by design assign all available particles to jets, thus requiring external background subtraction to be performed beforehand) and both are commonly used, depending on the task at hand and/or properties of the experiment in question.

Unfortunately many situations exist in which jet reconstruction is not feasible. The primary problem here is that although high-p_T particles originate exclusively from hard scatterings, lower-p_T ones can be of either hard or soft origin. As a result, going down in transverse momentum — be it because of the cut-off imposed by collision energy or simply in order not to lose too many jet particles — typically leads to contamination of the hard sample, throwing reconstruction algorithms off. Under such circumstances it is necessary to substitute event-by-event jet reconstruction with statistical methods — attempting to have the jets' collimation in

space, in particular in azimuth, stand out by "accumulating" it over numerous events in the course of a *correlation* analysis. This is the method which has been used in the course of the project described in this dissertation. There is of course background to be accounted for in this approach too (to name just a few sources — resonance decays, momentum conservation and so on), they are however in principle easier to address at this level than while dealing with individual particles. An in-depth discussion of how the correlation method will be provided in Chapter 3.

1.4.4 Jets and the Hot, Dense Medium

The reason for introducing the subject of jets in this dissertation is that as they are produced in partonic rather than hadronic interactions, they can be reasonably expected to be sensitive to the presence in a collision of a medium consisting of unbound partons! There are several different effects such a medium can have on jets traversing it. These include:

- **high-p_T particle yield suppression** — interaction of jet partons with partons of the medium results in drop in observable yield of particles with high transverse momentum;
- **quenching** — an extreme case of yield suppression, expected to occur when a dijet is produced just under the surface of the plasma drop: one of the jets exits the drop almost undisturbed, partons of the other on the other hand undergo so many interactions with the medium that the jet never makes it out [73, 74]. See Figure 1.9 for an illustration;

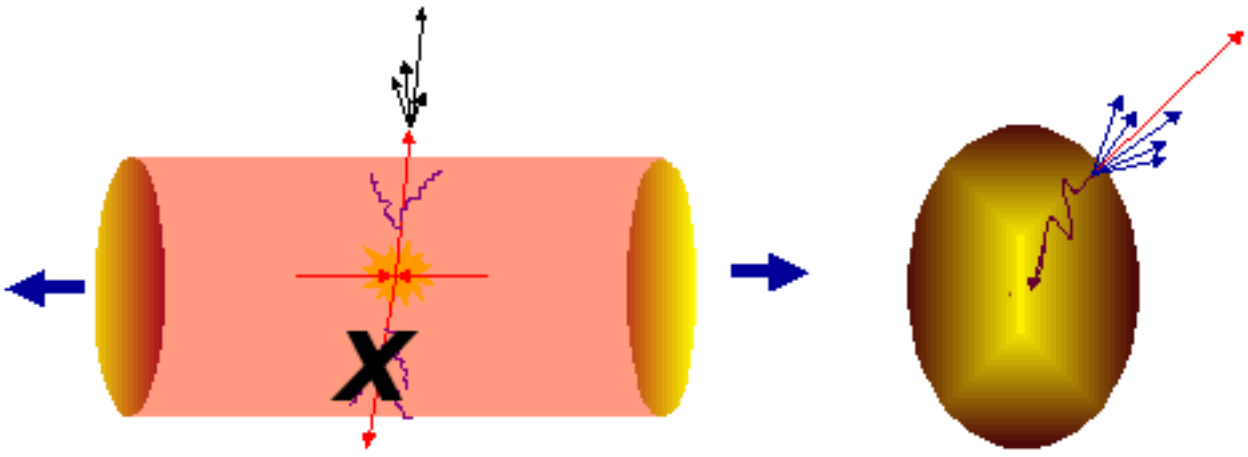

Figure 1.9: A diagram illustrating jet quenching in quark-gluon plasma [75].

- **shock waves** — a recently-proposed phenomenon, based on the present-day that quark-gluon plasma behaves more like a liquid than like a gas: the process of quenching one of the jets results in conical emission of gluon radiation, resulting a structure resembling the Mach cone [76, 77, 78];

- **bending** — also a recent addition to the list: interaction of a jet with the medium could cause the latter to become deflected from its original trajectory. Could co-exist with suppression.

Results from RHIC

Given concept behind the project described in this dissertation has been heavily influenced by results pertaining to hard processes which have been obtained by RHIC experiments, it is only natural to provide a brief overview of these results.

Figure 1.10 shows a combined plot of results from different RHIC experiments pertaining to possible modification of jet properties by quark-gluon plasma, which was printed in 2003 on the cover of Physical Review Letters. BRAHMS, PHENIX and PHOBOS plots present results on high-transverse-momentum particle yield suppression expressed as *nuclear modification factor* — a ratio of yield-per-binary-collision from two systems[12]; high-p_T is clearly visible in central gold–gold collisions (red in BRAHMS and PHOBOS plots) but not in deuteron–gold (green in BRAHMS plot, PHENIX data) or peripheral-gold–gold (blue in PHOBOS plot) events. Last but not least, the two-particle azimuthal correlation function of charged hadrons (STAR plot) features only the near-side peak in central *Au+Au*, whereas both *p+p* and *d+Au* functions show two peaks. All these results are consistent with expectations of QGP formation.

On the other hand, more recent results from both STAR and PHENIX (see Figure 1.11) have shown results consistent with shock waves or jet bending: two-particle correlation functions produced at lower transverse momentum than before show a double-hump structure which could be caused by either of the two. Studies are underway to determine which of the two mechanisms is behind this effect, however no definite results on the subject have been posted yet.

Also quite recently, expansion of analysis of high-p_T angular correlations at RHIC energies into two dimensions — ($\Delta\eta$, $\Delta\phi$) correlations — has resulted in discovery of a *ridge*-like structure on the near side of the correlation function in most central *Au+Au* collisions, as shown in Figure 1.12. This effect is hypothesised to be another signature a hot, strongly-interacting medium [81, 82].

Last but not least, behaviour of transverse-momentum spectra measured by RHIC experiments is consistent with power-law predictions above approximately 2 GeV/c. An example of this can be seen in Figure 1.13: at high p_T, the spectrum clearly diverts from the Boltzmann distribution.

1.4.5 Hard Processes at SPS Collision Energies

The role hard processes play in collision events depends very strongly on the energy of collisions in question: while hard scattering constitutes as much as 98 % of total interaction cross-section

[12] Typically, *p+p* yield is used in the denominator.

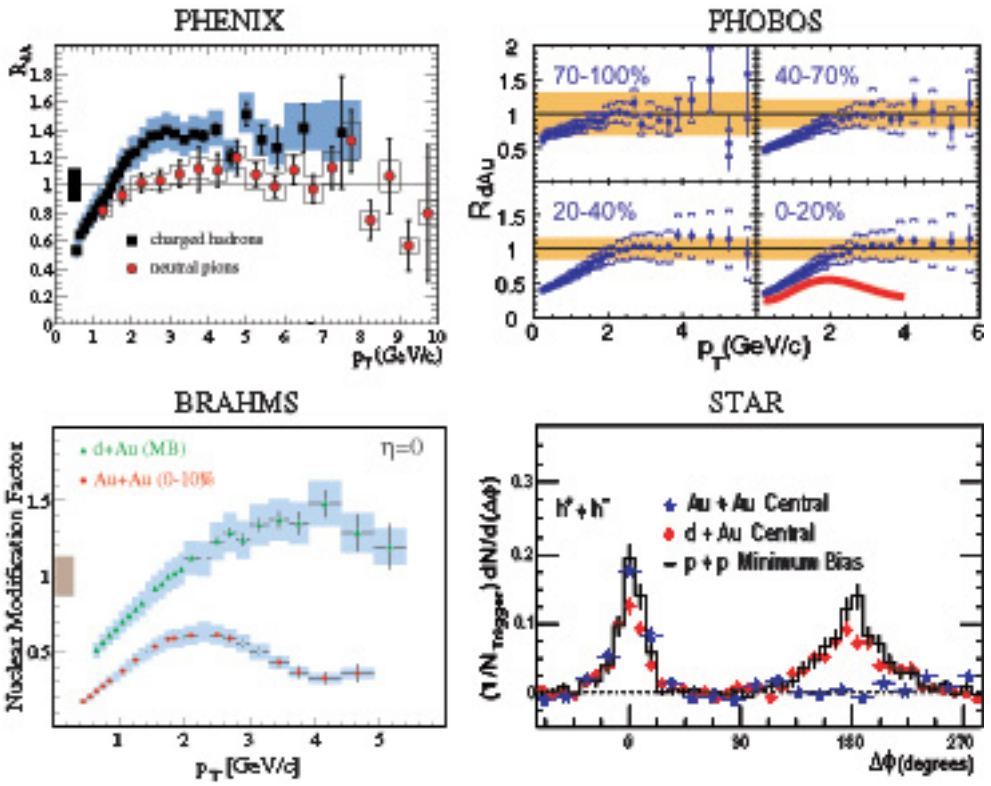

Figure 1.10: The cover picture of Physical Review Letters Volume 91 Issue 7 (published on the 15th of August, 2003), presenting chosen RHIC results pertaining to probing the QGP by its interaction with jets in central *Au+Au* collisions at 200 GeV. In such data, high-p_T particles are suppressed (red data in PHOBOS & BRAHMS plots) and there is only one peak in the two-particle azimuthal correlation function (STAR); both results are as expected if a quark-gluon plasma forms. A QGP is not expected in *d+Au* collisions and this data show no high-p_T suppression (PHENIX) and two correlation peaks.

at LHC energies and still about 50 % at RHIC, it contributes only 2 % at the SPS [84]. As a result, SPS yields of high-p_T hadrons are very small.

Given the aforementioned effect of steeply-falling spectra it is more-or-less necessary to extend the considered range of transverse momentum into the so-called intermediate region of 1–2 GeV/c. This, however, leads to a number of additional issues which need to be considered:

- The current state of knowledge doesn't provide much information regarding the nature of transition from soft to hard physics;
- The intermediate-p_T region is sensitive to Cronin enhancement, an effect which has not been exactly understood yet. Moreover, although it is expected to be quite strong at the SPS its exact magnitude is not known yet;
- Operating quite far from the asymptotic-freedom realm results in large uncertainties in pQCD calculations.

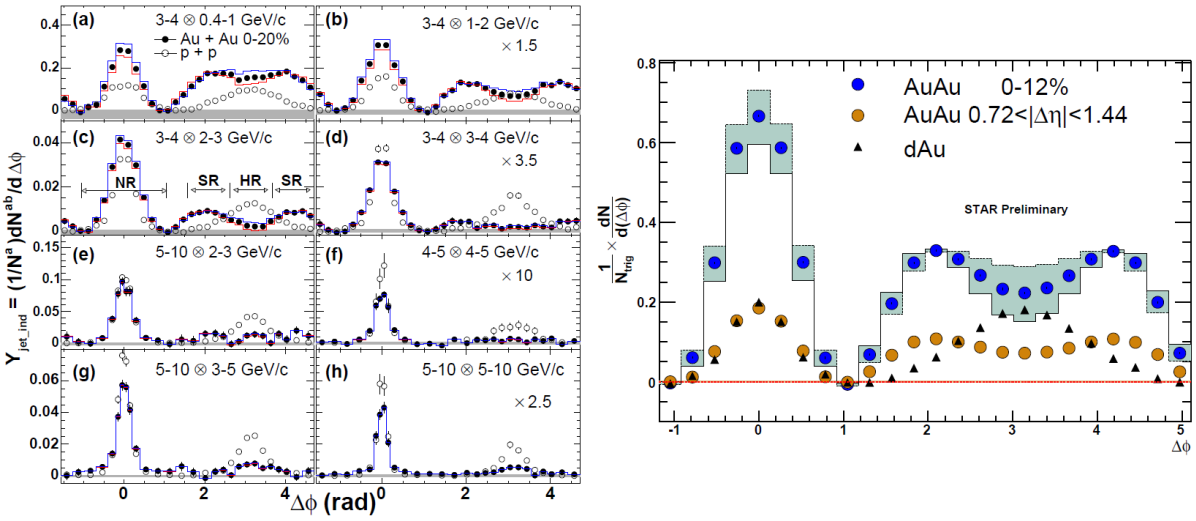

Figure 1.11: Recent two-particle azimuthal correlation functions from PHENIX (left) and STAR (right) at the RHIC [79, 80].

As a consequence of these issues "high"-p_T physics at SPS energies is a very challenging task — not only is it necessary to deal with non-trivial soft background but the hard processes themselves lack a precise quantitative description too. Therefore, for any obtained results to be meaningful it is vital to compare them to available models. How such a comparison was made in the course of this project is described in Chapter 6 of this dissertation.

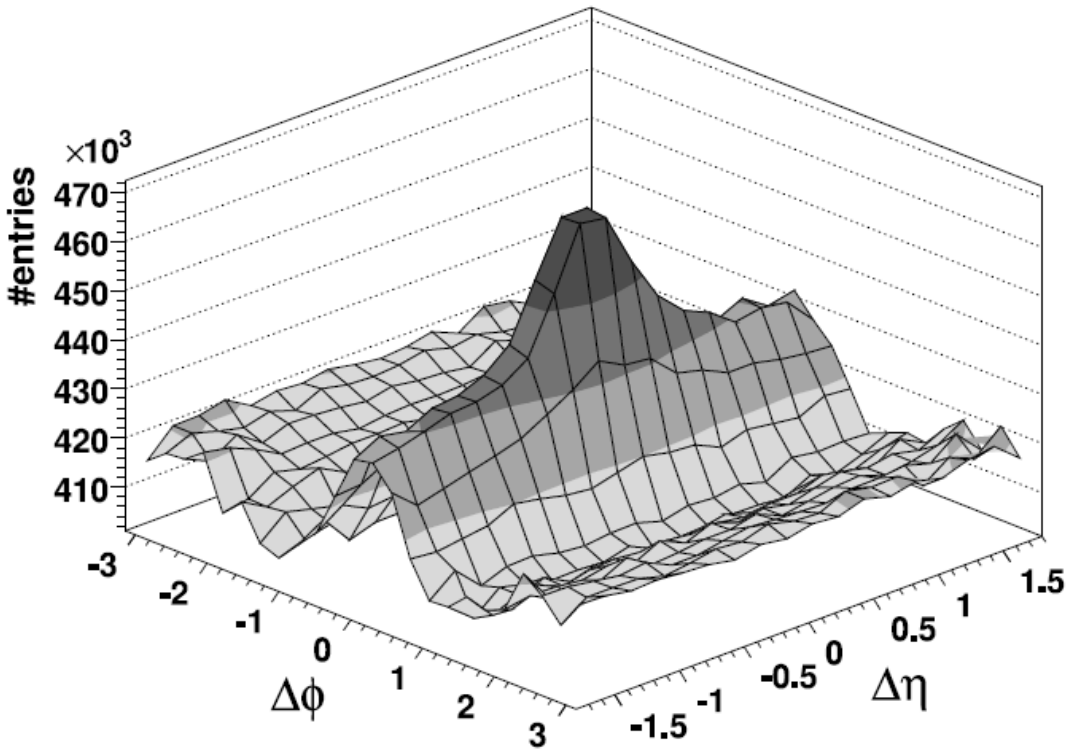

Figure 1.12: A two-particle ($\Delta\eta$, $\Delta\phi$) correlation function from central *Au+Au* collisions at 200 GeV acquired by the STAR experiment, for 3 < p_T^{trg} < 4 GeV/c and p_T^{asc} > 2 GeV/c [82]. The ridge structure is clearly visible for $\Delta\phi \approx 0$ along the whole visible $\Delta\eta$ range.

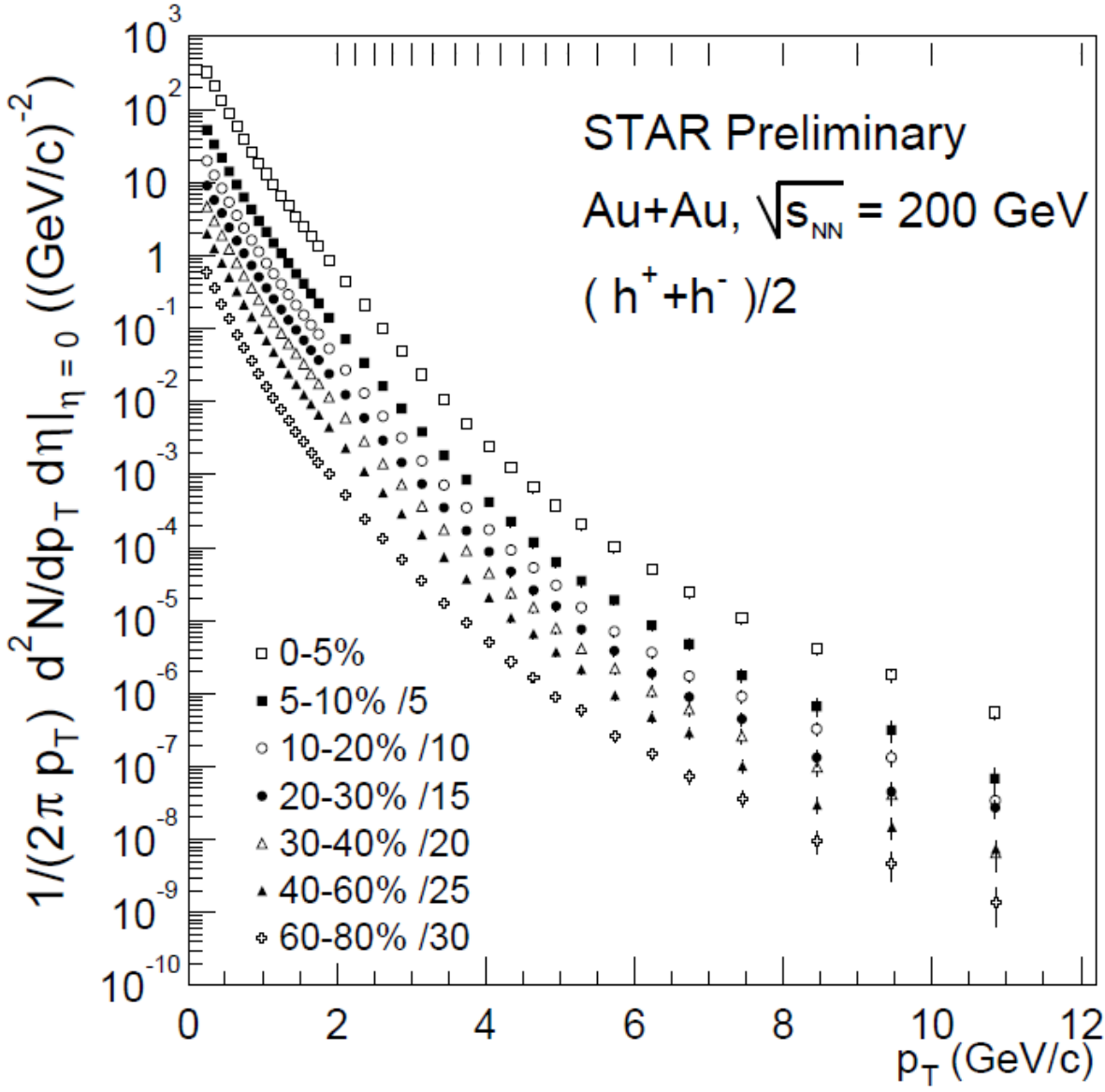

Figure 1.13: Transverse-momentum spectra of charged hadrons from *Au+Au* collisions at $\sqrt{s_{NN}}$ = 200 GeV, measured by the STAR experiment at the RHIC. Deviation from the Boltzmann distribution (*i.e.* the straight line) is clearly visible above $p_T \approx 2$ GeV/c [83].

Chapter 2

The NA49 Experiment

NA49 is a fixed-target experiment at the Super Proton Synchrotron at the European Particle Physics Laboratory CERN, on the Swiss-French border near Geneva. Together with NA44, NA45/CERES, NA50, NA52/NEWMASS, WA97 (now NA57) and WA98, it belongs to the comprehensive high-energy heavy-ion physics program of SPS, specifically designed to investigate the high-multiplicity (up to 450–500 charged particles per unit of rapidity [85]) environment of central Pb+Pb collisions in the search for experimental evidence for the presence of quark-gluon plasma in such reactions.

2.1 The Super Proton Synchrotron

The SPS, officially commissioned on the 17 June 1976, is located underground near the CERN site and has got a circumference of about 7 km. It was originally designed as a source of high-energy protons (originally up to 400, later on upgraded to 450 GeV) for fixed-target experiments, however during its 32 years of operation it has also served as: the world's first proton–antiproton collider, an electron/positron pre-accelerator for injection into the Large Electron-Positron Collider (LEP), and last but not least an accelerator of lead nuclei up to to 170A GeV; the latter capability made it the world's most powerful heavy-ion accelerator until the commissioning of the RHIC in 2000. At present its operations programme includes acceleration of protons and lead nuclei, as well as possibly lighter ions in the near future, for both fixed-target experiments (including production of a secondary neutrino beam for the CNGS[1] project) and injection into the Large Hadron Collider.

[1] CERN Neutrinos at Gran Sasso

2.2 The NA49 Detector

The NA49 detector is a general-purpose, wide-acceptance[2] spectrometer located in the H2 beam line of the North experimental hall of the SPS. Its detection capabilities are provided primarily by four large-volume Time Projection Chambers (TPCs), two of which are located inside magnets, and complemented by Time-of-Flight (TOF) walls, a set of calorimeters and a number of beam detectors. The layout of the complete set-up is shown in Figure 2.2, whereas appropriate section of Appendix A describes in detail the NA49 general co-ordinate system.

2.2.1 The Magnets

NA49 features two identical superconducting dipole magnets about 2.0 and 5.8 m[3] away from the target position, centred on the beam line and offering a maximum combined bending power of 9 Tm at currents of 5 kA. By default, *i.e.* for 158A GeV collision energy, the magnets produce field of 1.5 and 1.1 T, respectively; these values are appropriately scaled down for lower collision energies. The field is not homogeneous due to lack of pole tips, as a result precise determination of its magnitude and orientation is necessary in order for data from in-field TPCs to be usable. Two independent methods have been used here: numeric calculations and detailed Hall-probe measurements in a grid.

Most particles produced in a collision end up traversing the field generated by the two magnets. Thanks to the transverse momentum kick of 1.5 GeV/c provided by the field, all but the fastest particles of opposite charges become deflected in opposite directions in the bending plane.

2.2.2 Beam Detectors and Triggering

Several different beam and triggering detectors are used in NA49, with details of layout depending on the species of beam particles. To begin with, a set of upstream beam counters (S1, S2 in Fig. 2.2) provides precise timing information. These are standard scintillator devices in case of hadron beams, replaced by Čerenkov counters for Pb running in order to minimise the total detector material in the beam line. Secondly, a telescope of beam position detectors (BPDs), small proportional chambers with cathode strip readout, is used to precisely determine the position and, together with the aforementioned S2 counter, charge of incoming beam particles. Next, anti-coincidence of the incoming beam particle with the scintillation counter S4 or the Čerenkov counter S3 provide, for proton and lead-ion beams respectively, triggers on interaction with the target. Finally, there are two centrality-trigger detectors: the cylindrical proportional-tube detector CD which measures centrality in hadron-nucleus collisions by measuring the number of "gray" target protons, and the Veto Calorimeter (VCAL) which does the same in nucleus-nucleus collisions by measuring the energy flux remaining in the beam area after a collision.

[2] It has been designed to register up to 80% of particles produced in a collision.
[3] magnet centres

2.2.3 TPCs and Tracking

Time Projection Chambers, with their superior capabilities in pattern recognition and energy loss measurement, as well as good two-particle and space resolution and low material density in the path of particles, meet the requirements imposed on detectors which are to successfully tackle extreme multiplicities and densities of particles in heavy-ion collisions. NA49 features four such chambers: two "Vertex" TPCs (VTPC-1/2) inside magnets and two large "Main" TPCs (MTPC-L/R) on both sides of the beam behind the second magnet.

The four TPCs of NA49 follow the same design principle of vertical, hanging structure with the field cage consisting of horizontal Mylar strips stretched between vertical, titanium-coated ceramic tubes, the High Voltage plane — also from Mylar strips in order to minimise weight — at the bottom, the support plane containing readout hardware at the top, and the nitrogen gas envelope, between two layers of Mylar foil stretched on a fibre-glass epoxy double frame, surrounding the assembly. The only difference between Main and Vertex TPCs other than their sizes is that in order to eliminate harmful effects of channeling the beam through the detector volume without jeopardising the NA49 material-in-path constraints by inserting a beam pipe, the latter feature a vertical split of the field cage around the line of the beam. Readout is accomplished using proportional chambers as typically used in time projection chambers. The gas mixtures used in the TPCs, chosen specifically to provide low transverse and longitudinal diffusion coefficients (which is especially important in the Main chambers, as they operate outside the magnetic field) as well as moderate drift velocities, are 90/10 Ne/CO_2 for the VTPCs and 90/5/5 Ar/CH_4/CO_2 for the MTPCs; the gases are carefully recirculated, stabilised and monitored for leaking and impurities, especially for oxygen contamination.

As mentioned above, the 62 proportional chambers used in the NA49 TPC system for readout purposes are of fairly typical design (see Fig. 2.3): seen from the drift space, the gating grid (which is used to control when drifting electrons are to be let into the chambers) is followed by a grid-like cathode plane, then by a plane of interspersed sense and field (zero-potential) wires, and finally by a pad plane. Due to high track density in heavy-ion collisions adversely affecting signals available on sense wires, readout is performed by pads only. The pads have got different length and are installed at different angles depending on their position in the detectors in order to match expected topology of tracks introduced by the magnetic field, thus minimising effect of the angle between pads and tracks. The whole readout system is highly compact, with the smallest pads being as narrow as 3 mm, resulting of electronics density of up to 4000 channels per readout module.

Calibration

A number of calibration procedures have to be performed in order for TPC data to be usable. In particular, one needs to: know the drift velocity of ionisation electrons as well as $\vec{E} \times \vec{B}$ and other distortions, determine appropriate gas and electronics gain and so on.

Drift velocity can be determined using appropriate monitors installed as a part of the gas system and this is the approach primarily employed by NA49, sometimes however, for instance if precision higher than what monitors can provide is required, it is useful to be able to use alternative means. In the earliest stage of its running NA49 used the so-called charge step method for that purpose; this approach involves fitting the back edge of the charge distribution of tracks corresponding to the position determination of the drift high-voltage plane. The alternative, which involves inducing tracks in chamber volume with lasers, was not practical because design of NA49 TPCs makes it difficult to guarantee necessary high-precision positioning of such tracks.

Despite not using lasers in drift velocity calculations, the NA49 detector does feature a laser system. It is based on a pulsed Nd-YAG laser with two frequency doublers, along with an automated monitoring-and-steering system and a series of adjustable beam splitters capable of delivering laser pulses into different parts of the entire drift volume of each of the TPCs. This system has been used in studies of both tracking performance and all kinds of track distortions; it has proven especially useful, if not crucial, in controlling the aforementioned $\vec{E} \times \vec{B}$ distortions.

Finally, gain calibration of both electronics and gas is achieved, simultaneously, by measuring charge spectra obtained by releasing a known number of electrons into the TPC volume — which in turn is achieved by injection of radioactive $_{86}$Kr gas. Although this approach is more cumbersome than the alternative solution of generating well-defined pulses on the field wires in readout chambers, as it requires incorporation of a krypton source into the gas system along with having to wait until the injected sample has decayed before normal data taking can resume, unfortunately the latter cannot be used in NA49 due to limitations of front-end electronics. Luckily it has been shown that time evolution of detector properties is uniform over a single SPS running period (typically 6 to 8 weeks), making it possible to perform Kr calibration runs only before and after each period and still achieve accuracy better than 1 %.

2.2.4 Time of Flight

A pair of time-of-flight walls has been installed in NA49 set-up in order to improve identification of relatively low-momentum particles, where dE/dx identification is less reliable, and to assist separation of kaons from protons. The walls, installed on rotating platforms just downstream from MTPCs, are large-area (4.4 m^2 total surface) pixel-scintillators with 1782 individual scintillation detectors. Measurements performed in central Pb+Pb collisions have shown the detector to offer time-of-flight resolution of approximately 60 ps and about 70 % efficiency. TOF hits are matched to extrapolated TPC tracks, thus making it possible to identify particles by both dE/dx and mass (see Figure 2.4). The walls have been set up in a way that offers mid-rapidity acceptance of kaons at different beam energies.

As the analysis that is the subject of this dissertation doesn't require identification of particles and requiring TPC tracks to be associated with TOF hits significantly reduces acceptance, this part of the detector has not been used in this analysis.

2.2.5 Veto Calorimeter and Centrality Selection

As mentioned in Section 2.2.2, centrality selection in nucleus-nucleus collisions is performed in NA49 using the energy of spectator nucleons deposited in the so-called Veto Calorimeter. Constructed originally for the NA5 experiment, the VCAL has got sandwich-like structure with two clearly defined sections — a lead/scintillator one followed by one with iron instead of lead — and is located 20 m downstream of the target, behind a collimator whose purpose is to limit contamination from particles produced in interactions.

On a short time scale the relation between energy deposited in the Veto Calorimeter and the number of observed charged tracks in an event — which is proportional to its centrality — is, as it can be seen in Figure 2.5, mostly linear except for ultra-peripheral collisions, making it quite easy to translate veto energy into (projectile) centrality — one can define it simply as

$$C_{proj} = C_{trig} \cdot \frac{\int_0^{E_{veto}} \mathrm{d}N/\mathrm{d}E_{veto,trig}\mathrm{d}E_{veto}}{\int_0^{\infty} \mathrm{d}N/\mathrm{d}E_{veto,trig}\mathrm{d}E_{veto}} \cdot 100\ \%, \tag{2.1}$$

where E_{veto} is the event's spectator energy measured by VCAL, $C_{trig} = \frac{\sigma_{trig}}{\sigma_{inel}}$ is the fraction if inelastic cross-section accepted by the trigger (σ_{trig} is derived from target thickness and the interaction rate, whereas σ_{inel} is assumed to equal 7.15 barn) and $\mathrm{d}N/\mathrm{d}E_{veto,trig}$ is the spectator energy distribution for the trigger in question [89].

Determination of centrality using spectator energy is more complicated in the long-term picture, as it then becomes necessary to take into account the fact that calorimetric measurements are usually time-dependant — primarily due to the aging of the detector as a result of radiation exposure. With the VCAL signal monotonously degrading over time, it is necessary to introduce additional corrections in order to be able to reliably compare centrality of same-type events from different running periods. In NA49 the method currently used for this purpose, has been developed by A. László; unlike many other such methods it doesn't require large data samples for calibration to work, thus being applicable to all acquired data sets [88].

2.3 Data Acquisition and Event Rates

The requirements set for the NA49 data acquisition system by the number of charged particles observed by detectors are, despite the fact they are even greater for RHIC and LHC experiments, considerable. One of the basic concepts of the experiment was being able to acquire $\propto 10^6$ events per SPS running period, which with 4.8-second spills[4] every 20 s requires collecting at least 20 events per spill. With raw data from a single event taking up up to almost 100 megabytes and the trigger rate of about 10 Hz, this amounts to at least about 4.7 GB per SPS spill.

The heart of the NA49 DAQ system is a VME master crate, fitted with a Motorola 68040-based processor unit and a number of memory units, which steers all data acquisition. It is con-

[4] In case of Pb — for p-beams they are 2.37 s long.

nected, using VICbus and VSB connections, to six slave crates containing 60 read-out boards for the TPCs, connected in turn — over optical links — to front-end electronics cards located on the detectors. A FASTBUS connection to an Aleph Event Builder is used to collect data from TOF, whereas a CAMAC interface is used to acquire information from the Veto Calorimeter along with beam and trigger detectors. A Microchannel interface to the host workstation, an interrupter connected to trigger-logic hardware and a tape interface complete the set-up. All Motorola-based processors run the real-time operating system OS/9, whereas the host workstation which boots them and serves as a file server is based on Unix [90].

In order to match the data-storage speed limitations of the tape system (about 15 MB/s), the data acquired from FEE cards needs to be processed. The primary technique used for this purpose by NA49 has been zero suppression, performed by digital signal processors (DSP) fitted on receiver boards. As the memory buffers of a board could only be accessed by the DSP while the FEEs were not being read, most of the processing had to take place in the 15-second period between spills; this together with limited memory capacity of receiver boards (32 raw events) has limited the final data rate of the detector to 28-30 events per spill for central *Pb+Pb* collisions, increased appropriately for smaller events and/or larger SPS cycle length. The size of a central Pb+Pb event at the time of storing it on tape is about 8 MB.

The DAQ system of the Time Projection Chambers was reconfigured for the year 2000 data-taking period in order to maximise the number of collected events: the number of time bins used for digitisation of TPC pulses was decreased from 512 to 256 by configuring detector electronics to digitise and send only every other sample, thus halving the dead time of the TPC and effectively doubling the capacity of receiving-board buffers, along with programming the DSPs to compress the data sent to the master crate. Complemented by appropriate changes to trigger and beam-line parameters, this approach allowed NA49 to achieve the event size of 3 MB and the rate of 48 events per spill, with the theoretical limit of 64 not reached only due to limitations of the tape system and dead time of other detectors.

2.4 Reconstruction of Data

After an event has been acquired and stored it needs to be *reconstructed* before it can be meaningfully used in an analysis. In case of NA49 reconstruction would be performed off-line, some time after the end of respective data-taking periods, using custom software running on CERN's lxPlus/lxBatch batch farm. The software is responsible for reconstruction of tracks (cluster finding, tracking, fitting), determination of vertices positions, and calculation of dE/dx from TPC information and particle mass from TOF data, as well as application of various calibration and correction factors in the process.

1. The first step of reconstructing a track is to group signals from adjacent read-out pads (x and z coordinates) and time bins (y coordinate) into **clusters**. A number of corrections is

applied at this stage, including corrections for: non-uniformity of the magnetic field and $\vec{E} \times \vec{B}$ effects, pad gain, electronics response, charge loss and so on. Clusters in the vertex chambers are additionally checked for possible merging as a result of high track density. Mean position is calculated for each found cluster and the resulting *points* are stored for further processing;

2. After the cluster finder has done its duty, a pattern-recognition algorithm is launched to group together points belonging to (hopefully) the same tracks. The NA49 **tracker** is multi-stage, with the most simple geometries being used as patterns when the number of available points is large and increasingly more complex ones included as the number of points drops. Tracking begins in MTPCs, after which extrapolation to the target plane is performed in order to collect points in VTPC2 lying close to MTPC tracks. Pattern recognition is then performed on VTPC2 points with extrapolation of VTPC2 or VTPC2+MTPC tracks to the main vertex and collection of VTPC1 points, then on VTPC1 points, and finally on remaining points in MTPCs. The number of points a track recognised by pattern recognition is associated with in each of the chambers is stored for future reference in the *rtrack* structure;

3. A *track fit* is performed on the found track trajectories in order to determine the particles' momentum. Since at this stage neither the primary nor secondary vertex have been located yet, momentum is calculated for the z position (and only z — x and y are, together with all three momentum components, free parameters of the fit) of the first point of each *rtrack*;

4. The fourth step is to obtain *position of the primary vertex*. In NA49 this is done using two independent approaches. To begin with, the so-called BPD vertex is obtained by combining x and y information from Beam Position Detectors with the known z position of the target. Note that since the value of the last co-ordinate is fixed, this method cannot tell whether the vertex is really located in the targer or not. Therefore, in order to reject out-of-target (beam-gas) events a **vertex fit** is performed, based on the beam trajectory from BPDs and reconstructed tracks; in p+p events x and y are usually fixed to their BPD values, whereas in other systems all three co-ordinates are fitted. Both the BPD and the fit vertex are stored for future use, along with the status of obtaining each of them ("vertex flag");

5. Once the primary vertex has been located, the software performs another track fit on *rtracks* in order to determine which of the reconstructed tracks originated from the primary vertex. This time all tracks are forced to originate from the primary vertex (in most cases, the BPD vertex is used for this fit) and momentum is calculated at that vertex. The number of associated points in each TPC which have used in the fit is stored, as well as the result of fits ("track flag");

6. **Ionisation energy loss** (dE/dx) is calculated using a truncated mean of cluster charge for selected track points, momentum and properties of TPC gas. The primary source of dE/dx information in NA49 are the main chambers, however in order to improve resolution it is also calculated for vertex chambers and later combined into a global value from all four. Again, the software stores the number of points used by this step in each TPC;

7. Reconstructed tracks are extrapolated to **Time-of-Flight** walls. If a hit is found in one of the walls in close vicinity of an extrapolated track, information from TOF is stored in association with that track;

8. A number of other steps, *i.e.* detection of secondary vertices, is also performed. These will not be discussed in this dissertation.

The output of NA49 reconstruction software are the so-called *Data Summary Tape* (DST) files, containing streamed data structures used by the reconstruction chain; however, as those files are still relatively large they are usually processed further to *MiniDST* format. While MiniDST files do not contain all the information stored in DSTs, what they do contain is enough from the point of view of most physics analyses and they are much smaller — less than 200 kB per event even for central *Pb+Pb* collisions.

2.4.1 The Simulation Chain

In addition to real experimental data, physics analyses occasionally depend on input from simulations. Depending on the goals of this part of the analysis, two basic scenarios can be considered here:

- **full simulations**, in which all the data under consideration is produced artificially. These are normally used while comparing real data with predictions "as the detector would see them";

- **embedding**, in which case a (typically small) number of simulated particles is injected into and processed together with real data. These are useful when one needs a well-defined observable in an otherwise-realistic collision environment.

In a large number of cases it is beneficial from the analysis' point of view for simulations and embedding samples to undergo exactly the same treatment as experimental data — *i.e.* for both to be processed by the same reconstruction software. As the input for the two is dramatically different, obviously it becomes necessary to introduce an extension to the reconstruction chain which addresses this issue. In case of NA49 this simulation chain consists of the following parts:

1. **Kinematic input** prepared by hand or produced by an *event generator*, be it arbitrary ("Mickey-Mouse" generators) or realistic (*e.g.* PYTHIA, Venus, UrQMD, …). There are

many formats of such data, however the most common set of parameters they provide are x, y and z components of each particle's momentum vector, a unique identifier specifying the species of that particle and, if applicable, an identifier of its parent particle;

2. A **detector simulator**, which uses a detailed description of geometry and material budget of the detector apparatus to simulate effects of particles passing through it, as well as decays of unstable particles and production of secondary ones. The Monte Carlo tool used for this purpose by NA49 is *GNA49*, an adapted version of CERN-developed GEANT package, major version 3;

3. A **detector response simulator** — in case of NA49 a TPC simulation program called MTSIM, which uses properties of TPC gas and read-out in order translate information from GEANT into digitised output of TPC electronics, along with tools implementing signal-threshold cuts and compression normally provided by DAQ. At this point simulated and real-life raw data are virtually identical;

4. In the case of combining simulated and real data it is now necessary to *embed* the former into the latter. The tool GTEMBED used by NA49 does that by adding ADC signals from the two sources on a pad-by-pad basis.

At this point the data is ready to be reconstructed using standard reconstruction software.

The final step of processing simulated input takes place after reconstruction and its purpose is to *match* simulated particles to reconstructed TPC tracks. This is done with the tool GTEVAL by comparing the output of GNA49 with the latter, evaluating proximity of Monte-Carlo and reconstructed TPC points. Obviously, it is generally not possible to obtain a perfect match between the two; instead, mappings are generated which describe the quality of matching a Monte Carlo track to different reconstructed ones in terms of the number of matching points.

Both DST and MiniDST files containing simulated data consist of two branches: the first is made up by Monte-Carlo data from GEANT (momentum, ID, pointer to the parent, simulated TPC points *etc.*) along with maps from GTEVAL, the second contains reconstructed tracks and is identical in its properties to the contents of standard data files.

2.5 Data Sets

The eight years of running of the NA49 experiment can be divided into three phases, in accordance with each phase's different physical goals and, consequently, different types of acquired events. These phases are:

1. 1994–1996 — high-energy *Pb+Pb* runs, dedicated to the search for quark-gluon plasma through probes;

2. 1997–1998 — high-energy light-ion runs;

Code name	System	E_{beam}	$\sqrt{s_{NN}}$	Field	Centrality	Events
00R	p+p	158A GeV	17.3 GeV	std+	$\approx$ 90 % inelastic	1.7M
00X	Si+Si	158A GeV	17.3 GeV	std+	0–12 %	220k
01I	Pb+Pb	158A GeV	17.3 GeV	std+	0–23.5 %	2.9M
01E	Pb+Pb	80A GeV	12.3 GeV	1/2std+	0–7.2 %	265k
00C	Pb+Pb	40A GeV	8.8 GeV	1/4std-	0–7.2 %	180k
00W	Pb+Pb	40A GeV	8.8 GeV	1/4std+	0–7.2 %	350k
02J	Pb+Pb	30A GeV	7.6 GeV	30G+	0–7.2 %	355k
05A	Pb+Pb	30A GeV	7.6 GeV	30G+	0–32.5 %	150k
03A	Pb+Pb	20A GeV	6.3 GeV	20G+	0–7.2 %	290k
05B	Pb+Pb	20A GeV	6.3 GeV	20G+	0–32.5 %	150k

Table 2.1: Data sets acquired by the NA49 experiment which have been used in the present analysis

3. 1999–2002 — *Pb+Pb* runs at a wide range of energies, low-energy light-ion runs and high-energy *p+p* and proton–lead runs, dedicated primarily to the search for quark-gluon plasma through an energy scan.

The analysis described in this dissertation takes advantage of a large number of data sets collected NA49, in particular of those from the third phase. Basic information about the data sets in question is provided in Table 2.1.

2.6 The Future: the NA61/SHINE Experiment

In spite the NA49 experiment having finished taking data many years ago, its detector is by no means no longer needed — it is the core of one of the experiments dedicated to searching for the QCD critical point (see Section 1.2.2), NA61/SHINE [14]. Following the lessons learned during the running of NA49 and in order to meet the needs of all the physics goals of the experiment, a number of upgrades to the original detector has been designed and will, or have already been, installed:

1. A helium beam-pipe in and between the magnets, in order to reduce by a factor of 10 δ-electron contamination in sensitive volumes;

2. A new spectator detector, PSD, to replace the Veto Calorimeter, in order to improve veto-energy resolution by a factor of 5 and uniformity by a factor of 20, as well as possibly to allow for reaction-plane determination;

3. The third, "forward" TOF wall, located between the original two, for identification of low-p_T particles emitted at large polar angles;

4. New read-out hardware for the TPCs, in order to provide a factor-of-10 improvement in event rates — up to about 100 Hz;

5. A small, semi-cylindrical tracking detector based on novel GEM (Gas Electron Multiplier) technology, in order to enhance acceptance for charged particles in the backward hemisphere.

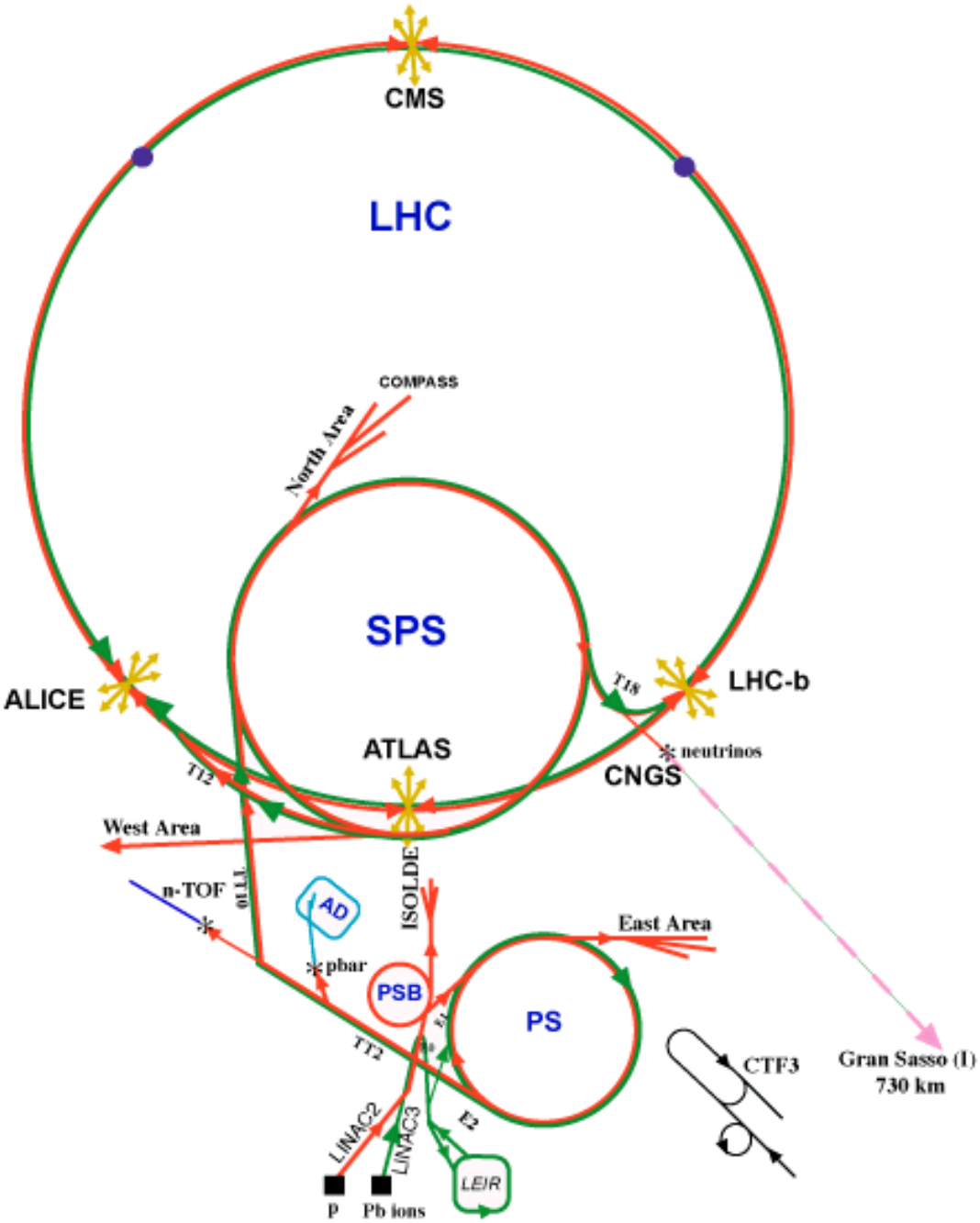

Figure 2.1: A diagram (not to scale) of the CERN accelerator complex, featuring the SPS in the centre. Line colours indicate accelerated particle species: red — protons, cyan — antiprotons, green — ions, pink — neutrinos, blue — neutrons, black — electrons. Abbreviations: LHC — Large Hadron Collider, SPS — Super Proton Synchrotron, AD — Antiproton Decelerator, ISOLDE — Isotope Separator OnLine DEvice, PSB — Proton Synchrotron Booster, PS — Proton Synchrotron, LINAC — LINear ACcelerator, LEIR — Low Energy Ion Ring, CNGS — CERN Neutrinos to Gran Sasso [86].

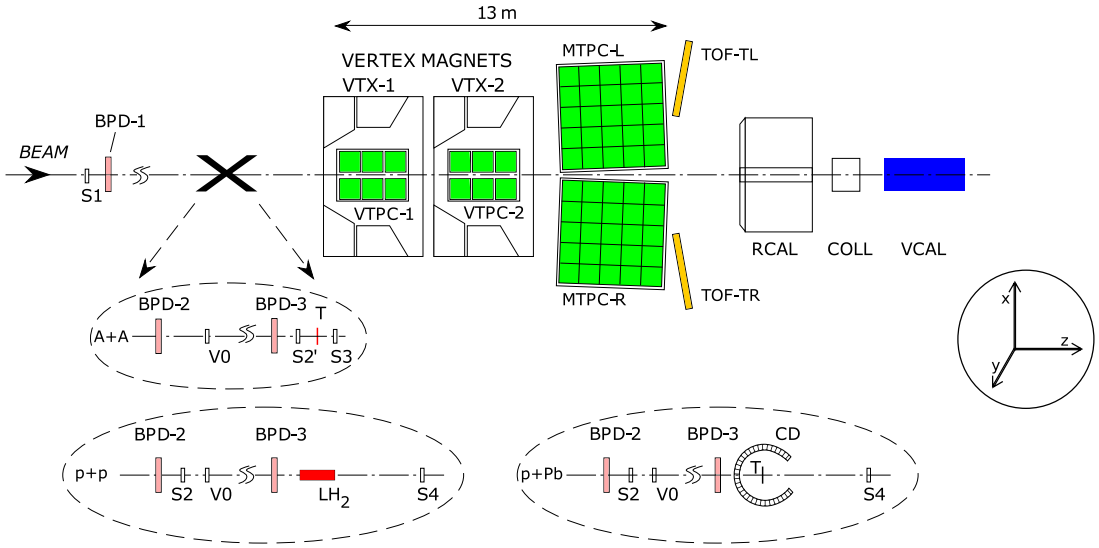

Figure 2.2: Set-up (not to scale) of the NA49 experiment, with different beam definitions and target arrangements. The general co-ordinate system of the experiment is also indicated [87].

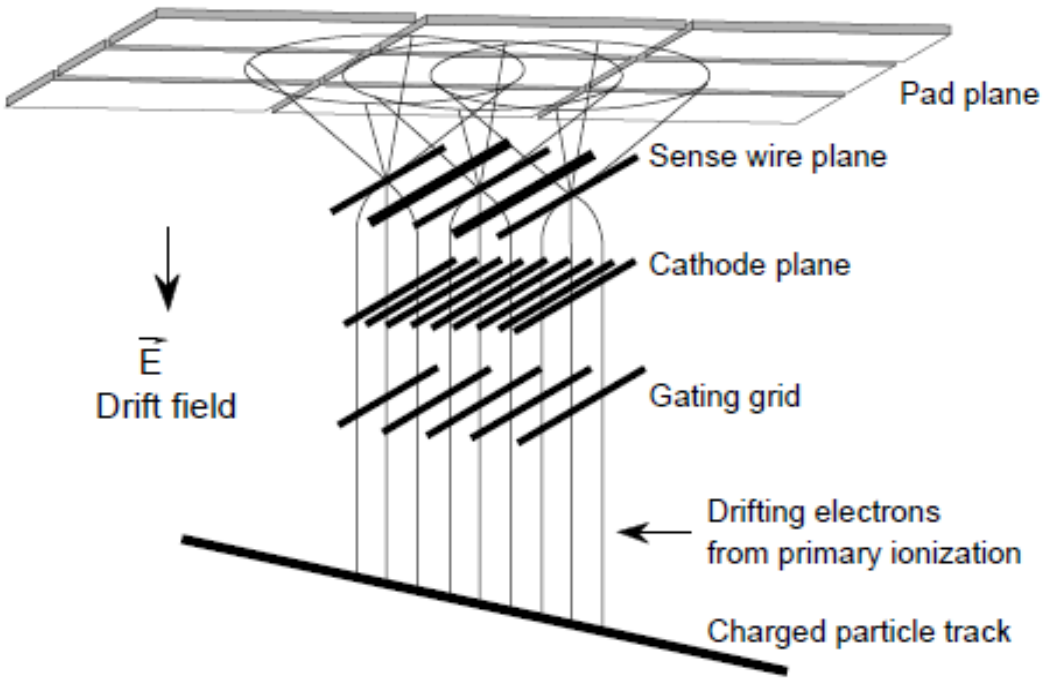

Figure 2.3: Schematic layout of TPC readout chambers, from [87].

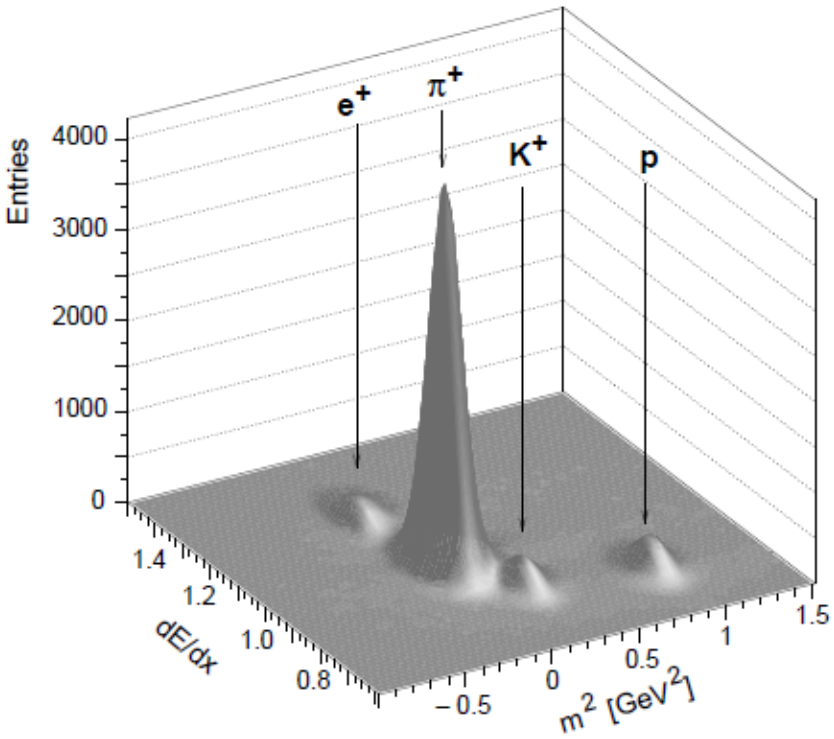

Figure 2.4: Particle identification by simultaneous dE/dx and TOF measurement in the momentum range of 5 to 6 GeV/c for central Pb+Pb collisions at 158A GeV [87].

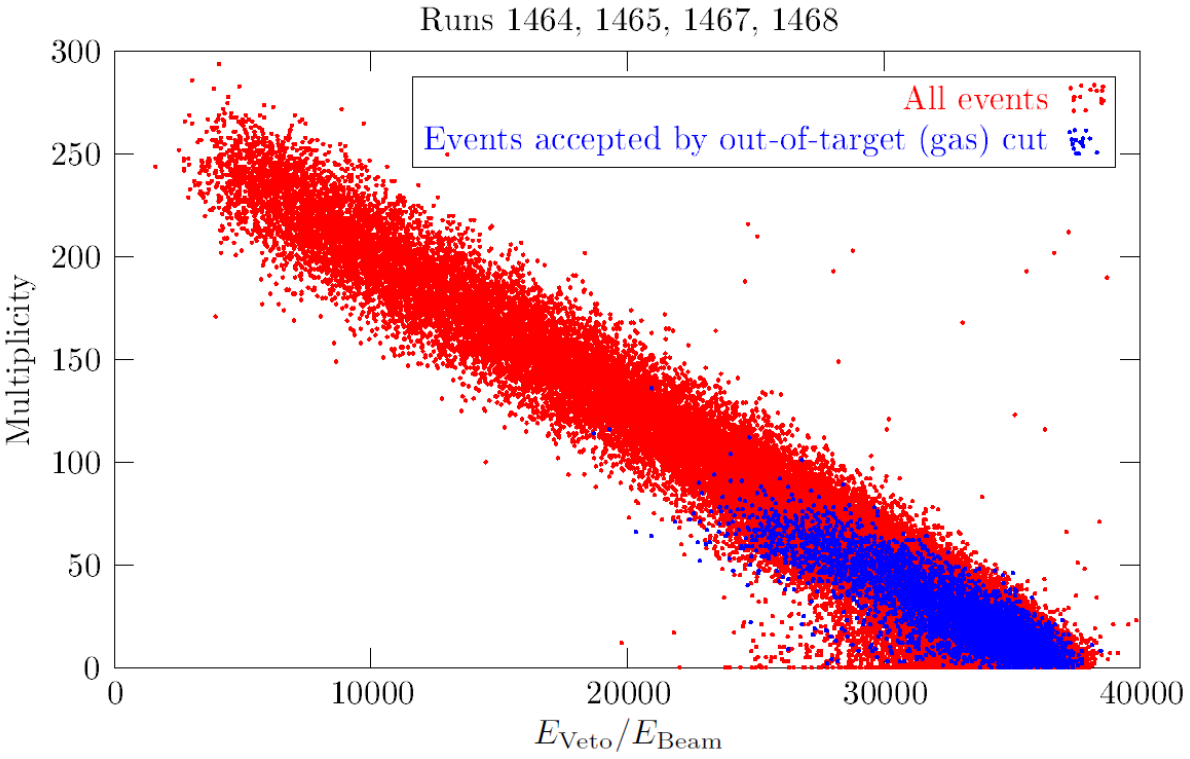

Figure 2.5: Relation between charged-track multiplicity of an event and energy deposited in the Veto Calorimeter of NA49, obtained from minimum-bias Pb+Pb collisions at 158A GeV [88].

Chapter 3

Data Analysis

3.1 Event and Track Cuts

A number of event and track cuts has been applied to data sets in question before they are used in the analysis. The purpose of introducing such cuts is, generally speaking, to remove as much background — by which one means both non-physical artefacts and physical phenomena not pertinent to the analysis in question — as possible from the sample as early as possible, thus not only improving the quality of data but also possibly reducing processing time. However, as in many cases it is not possible to unambiguously distinguish between signal and background particles, cuts tend to remove a bit of both; moreover, excessive cutting can increase statistical errors so much the final results are worse than with less pure input. Eventually, then, the practical goal of introducing cuts is to achieve balance between statistical and systematic uncertainties of results.

Below you will find a list of different cuts used in the analysis described in this dissertation, along with brief rationale behind applying them and example plots of quantities in question[1]. The actual values of those cuts for different data sets can in turn be found in Tables 3.2 and 3.3. Last but not least, note that only primary tracks (*i.e.* those known with high confidence to have originated from the event's primary vertex) are considered in this analysis. This step does not require any special analysis-time cuts, as primary and secondary tracks are distinguished from each other during event reconstruction and stored in separate branches of data files.

- Event cuts:

    1. **Main vertex flag**. This cut allows one to demand appropriate quality of primary-vertex reconstruction[2]. Two values have been considered acceptable in the course of this analysis:
        - 0 — main vertex is the fit vertex but the BPD one has been found too. This is the most common case;

[1] All of which have been produced from 10,000 central (0–5 %) Pb+Pb events at 158A GeV.
[2] See Section 2.4 for more information on the reconstruction procedure.

– 4 — BPD failed but vertex fit is OK, which of course implies main vertex is again the fit vertex. This one is considered acceptable in $p + p$ events — fixing the value of z can be unreliable when a long target is used, plus the fitting procedure for such collisions fixes x and y to BPD values anyway.

For an example distribution of this quantity, see Figure 3.1;

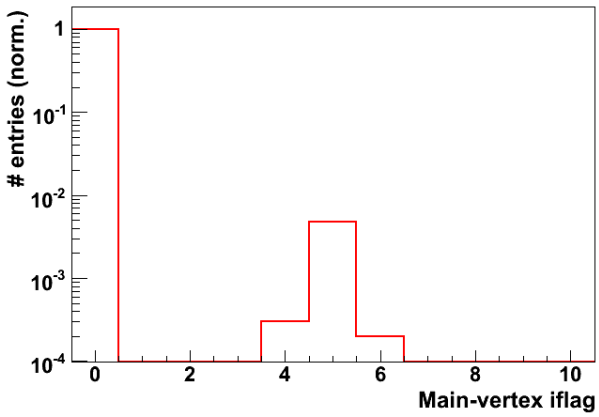

Figure 3.1: Distribution of main-vertex flag values in 10,000 0–5 % *Pb*+*Pb* events at 158A GeV, normalised to unity. Although the vast majority of events possess both the BPD and the fit vertex (flag value 0), events with issues are also present.

2. **Position of the fit vertex**. As mentioned in Section 2.4, it is possible for reconstruction software to occasionally find the "primary vertex" in beam-gas events; performing a cut on the z coordinate of the fit vertex makes it possible to remove most such events. Moreover, further improvement of signal quality can be achieved by restricting the vertex position in x and y as well. For example distributions of these quantities, see Figure 3.2;

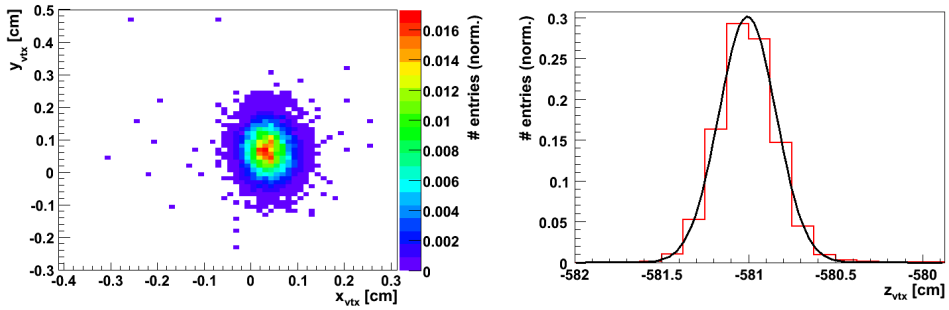

Figure 3.2: Distributions of x/y (left) and z (right) position of the fit vertex in 10,000 0–5 % *Pb*+*Pb* events at 158A GeV, normalised to unity. Fit vertices can be observed to be generally distributed in a three-dimensional Gaussian pattern around the intersection of the beam axis and the target position, with occasional points further away.

3. **Centrality**. Due to low efficiency of the on-line trigger for the most peripheral events it is often necessary in heavy-ion experiments to exclude most peripheral

collisions from analyses. Then again, as the analysis described in this dissertation concentrates exclusively on central and mid-central events, the purpose of centrality cuts it uses is only to select events of interest. In this study we have concentrated on the most central bin of 0–5 %, with some additional results from 5–10 % and 10–20 % events; in the three cases where events with centrality higher than 20 % have not been excluded from the data by an on-line cut (see Table 2.1), more peripheral events have been rejected simply to save processing time. For an example distribution of this quantity, see Figure 3.3.

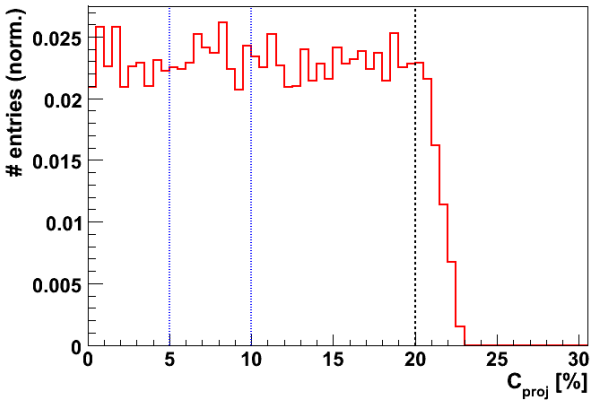

Figure 3.3: Distribution of event centrality (as defined by Equation 2.1) in 10,000 *Pb+Pb* events at 158A GeV (the *01I* data set), normalised to unity. The lack of events above 23 % stems from on-line cuts. Vertical lines indicate the boundaries of centrality bins pertinent to this study.

- Track cuts:

  1. **Rtrack flag**. MiniDST files of NA49 only contain tracks which have been reconstructed correctly, that is — with track flags equal to 0. Then again, it has been found that spectra of observed high-p_T particles in NA49 depend on flags of *rtracks* those tracks originated from, which are stored in MiniDST files. The reason for this is that most tracks with non-zero rtrack flags are tracks which only have points in MTPCs; due to their shortness and the lack of magnetic field in that part of the NA49 detector, such tracks feature very poor momentum resolution. In the analysis described in this dissertation we reject such contamination by requiring rtrack flag value of 0; Table 3.1 shows how this cut affects MTPC-only tracks;
  2. **Track impact parameter** ($\vec{b}$). A possibility always exists that a track classified as primary during reconstruction does not in reality come from the reconstructed primary vertex. Several possible sources of such tracks exist, including beam–gas interactions occurring simultaneously with beam–target ones, pile-up (particles from multiple collisions being observed in a single sampling of a detector) or decays of short-lived particles; uncertainty of tracking and vertex reconstruction can play a

Rtrack	$4.0 > p_T > 2.5$ GeV/c		$2.5 > p_T > 1.0$ GeV/c	
iflags	MTPC-only	rest	MTPC-only	rest
all but 0	5538	163	149735	14799
only 0	0	2673	0	355642

Table 3.1: Number of MTPC-only and other tracks (divided into triggers and associates as in the analysis) in 10,000 0–5 % *Pb+Pb* events at 158A GeV, depending on accepted values of rtrack iflags. Note how only a small fraction of tracks with non-zero rtrack iflag possesses VTPC points.

non-negligible part here as well. Imposing an upper limit on the impact parameter of tracks helps to reduce such contamination. For an example distribution of this quantity, see Figure 3.4;

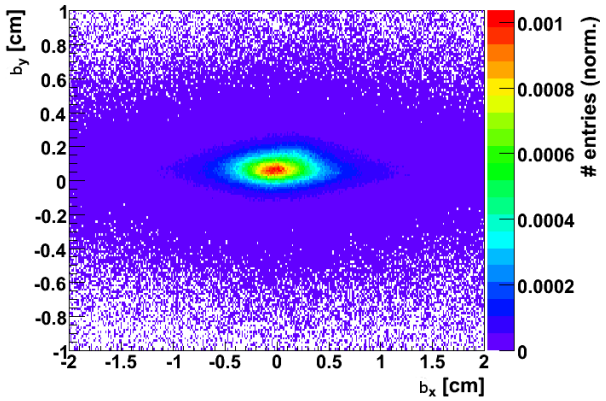

Figure 3.4: Distribution of track impact parameter ($\vec{b}$) in 10,000 0–5 % *Pb+Pb* events at 158A GeV, normalised to unity. Primary tracks can be observed to be generally distributed in a two-dimensional Gaussian pattern around the position of the main vertex.

3. **Number of TPC points**. The number of TPC points associated with a track (for example distributions of this quantity, see Figure 3.5) indicates how long this track is but also to some extent how reliable track information is. Including tracks with a low number of points can pose problems: on one hand real tracks that short are susceptible to distortions, on the other the smaller the number of points the greater the risk of random co-incidence of points being recognised as a track. Last but not least, short tracks feature poor momentum resolution; from the point of view of the analysis described in this dissertation this is particularly important in low-energy events, as in conjunction with low magnetic field (*i.e.* low bending power) and the fact such events feature lower mean track length than high-energy ones it can result in significant contamination of the high-p_T region of phase space with artefacts. In order to avoid such issues, a lower limit is imposed on track TPC points to reject short tracks;

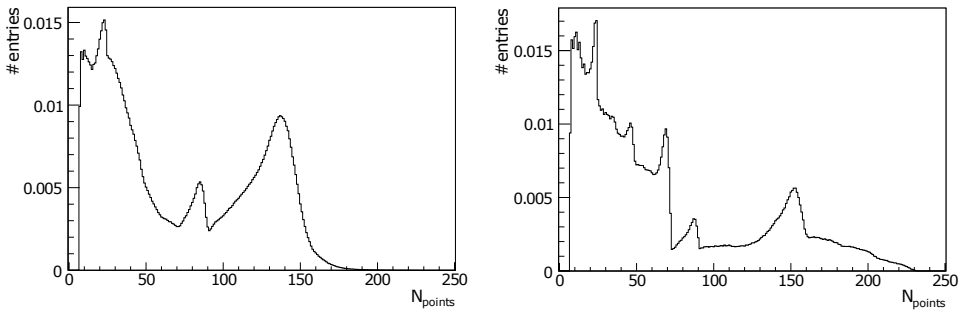

Figure 3.5: Distributions of the number of TPC points (from all chambers) per track in 10,000 0–5 % *Pb*+*Pb* events at 158A (left) and 20A (right) GeV, normalised to unity. The lower-limit cut-off at 7 points stems from settings of the track finder in reconstruction software.

4. **Real-to-maximum TPC point ratio**. Track reconstruction is not perfect, especially when their density is high. In particular, it is sometimes possible for a track to be *split*, *i.e.* for the reconstruction software to consider it as two. Such split tracks can significantly distort the overall image of an event and need to be removed, which is accomplished by comparing the number of points assigned to each track with the possible maximum, calculated basing on the track and detector's properties. Tracks for which a ratio of the two is too small are considered split and therefore rejected. For an example distribution of this quantity, see Figure 3.6.

   Note that the number of real and potential points can be considered either individually for each TPC or for all of them together. In this study we have taken the latter approach;

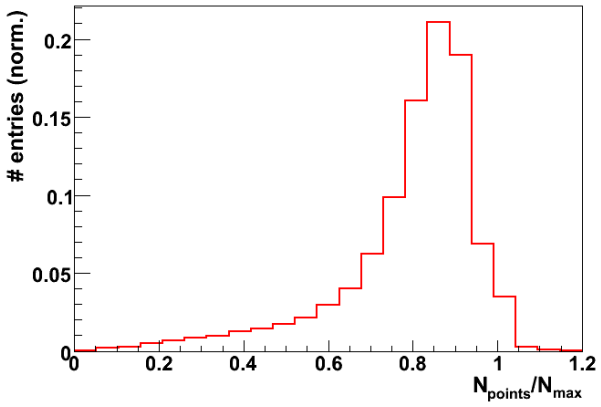

Figure 3.6: Distribution of the global (*i.e.* calculated for all TPCs) real-to-maximum TPC point ratio in 10,000 0–5 % *Pb*+*Pb* events at 158A GeV, normalised to unity. Note a non-zero number of tracks with the ratio larger than 1, which is caused by the fact N_{max} is only approximated.

5. **Broken tracks**. A track is referred to as "broken" if its trajectory contains gaps, that is — if it has no points in one or more of the TPCs even though its trajectory passes through those chambers. It has been observed by A. László that such tracks

Data set	Main-vertex flag	Fit vertex position [cm]			Centrality	% good
		x	y	z		
00C	0	-0.10 – 0.13	-0.24 – 0.23	-581.3 – -580.9	no cut	83
00R	0, 4	-0.30 – 0.40	-0.20 – 0.20	-590.0 – -572.0	N/A	52
00W	0	-0.10 – 0.13	-0.24 – 0.23	-581.3 – -580.9	no cut	84
00X-dedx	0	-0.50 – 0.50	-0.50 – 0.60	-581.0 – -578.0	no cut	63
01E	0	-0.11 – 0.08	-0.17 – 0.22	-581.5 – -580.9	no cut	81
01I	0	-0.10 – 0.20	-0.20 – 0.30	-582.0 – -580.0	0–20 %	91
02J	0	-0.12 – 0.21	-0.17 – 0.11	-581.5 – -581.1	no cut	79
03A	0	-0.22 – 0.17	-0.15 – 0.17	-581.3 – -580.9	no cut	83
05A	0	-0.21 – 0.26	-0.22 – 0.14	-581.7 – -580.3	0–20 %	33
05B	0	-0.25 – 0.21	-0.21 – 0.22	-581.5 – -580.9	0–20 %	36

Table 3.2: Event cuts applied to different data sets used in the analysis, along with percentage of events which pass these cuts in each data set. Legend for main-vertex flag values: 0 — main vertex is the one found by the vertex fit (but the BPD one also exists) 4 — BPD failed but vertex fit is okay (*i.e.* main vertex is fit vertex).

are generally artefacts[3], contaminating the high-p_T region of NA49 phase space [91]. Removal of this contamination involves going over each track's real- and potential-point number in each of the TPCs; a track is rejected if in one of them it has got no real points but more than a specified number of potential points;

6. **Total and transverse momentum**. Detector design and reconstruction algorithms only make it practical to work with particles from a certain range of momentum space; going beyond this range results, if possible at all, in a drop in efficiency and/or an increase in background levels. Although the analysis described in this dissertation uses momentum primarily for the purpose of particle selection and as such is more restrictive than implications of the above, keeping these limitations in mind has allowed us to establish boundaries for varying p_T bins used in the selection process. Distributions of p_T from all data sets used in this analysis can be found in Figure B.2 in Appendix B.

Effective acceptance Figures in Appendix B present acceptance plots for all tracks which have passed the aforementioned event and track cuts. Note that *no* cuts have been applied to (pseudo-)rapidity or azimuthal angle, thus making the shape of distributions of those two quantities depend solely on properties of the detector. As one can see, obtained p_T distributions appear to be free from distortions. On the other hand, acceptance in both y and ϕ is not uniform, which — in particular the latter — has to and will be taken into account while calculating correlation functions.

[3] Resulting *e.g.* from erroneous merging of independent short tracks.

Data set	Rtrack flag	$\vec{b}$ [cm] x	$\vec{b}$ [cm] y	N_{points}	Point ratio	Broken-track threshold	% good
00C	0	-1.11 – 1.17	-0.55 – 0.58	≥30	≥0.5	<10	47
00R	0	-1.31 – 1.52	-0.50 – 0.60	≥30	≥0.5	<10	72
00W	0	-1.11 – 1.17	-0.55 – 0.58	≥30	≥0.5	<10	47
00X-dedx	0	-1.63 – 1.68	-0.49 – 0.63	≥30	≥0.5	<10	69
01E	0	-1.07 – 1.17	-0.45 – 0.53	≥30	≥0.5	<10	46
01I	0	-1.16 – 1.19	-0.47 – 0.61	≥30	≥0.5	<10	53
02J	0	-1.16 – 1.20	-0.63 – 0.58	≥30	≥0.5	<10	47
03A	0	-1.22 – 1.20	-0.62 – 0.62	≥30	≥0.5	<10	47
05A	0	-1.11 – 1.16	-0.62 – 0.60	≥30	≥0.5	<10	56
05B	0	-1.23 – 1.17	-0.66 – 0.65	≥30	≥0.5	<10	57

Table 3.3: Track cuts applied to different data sets used in the analysis, along with percentage of tracks which pass these cuts in each data set. Legend: "point ratio" — ratio of the number of real to potential TPC points associated with all tracks; "Broken-track threshold" — number of potential points a track can have in any TPC where its number of real points is zero (see the text for more explanation).

3.2 Particle Selection

Cuts discussed in the previous section are expected to have removed all significant contamination sources from our track sample. Ideally, the remaining tracks should correspond to actual, physical particles. Now we shall discuss selection criteria applied to those particles in direct conjunction with the analysis in question.

All the correlation functions discussed in this chapter involve measuring the distribution of certain quantities — the difference in azimuthal angle, accompanied in some cases by the difference in pseudorapidity — between two or three particles taken from the same event. One particle in each pair/triplet, dubbed *the trigger*, is required to have relatively high transverse momentum; the other or others we refer to as *associate(s)* and are required to possess lower p_T than the trigger; if this is not the case[4] such a pair/triplet is not considered in the analysis. Such a division of particles has got its roots in application of such correlations to observation of hard processes. In this context, the trigger is required to have p_T high enough[5] to more-or-less make sure it originated from a hard scattering, whereas transverse momentum of associates was chosen to allow them to have originated from the same scattering as the trigger while not qualifying as triggers themselves.

In case of the analysis described here we try not to make assumptions regarding the source of correlations, which however does not prevent us from employing the trigger–associate classification.

[4]Which may happen if p_T bins for trigger and associate particles overlap.

[5]The theory-driven lower limit here is $1.5 - 2.0\ GeV/c$, with actual range depending of course on collision energy, detector capabilities and experimental needs.

It is also possible to measure so-called *non-triggered correlations*, in which case both particles in a pair are taken from the same p_T range and with no "$p_T^{trg} > p_T^{asc}$" constraint. However, analyses relying on that method reach beyond the scope of this dissertation and will not be discussed further.

In the analysis constituting the subject of this dissertation we use $2.5\ GeV/c \leq p_T^{trg} \leq 4.0\ GeV/c$ for trigger particles and $1.0\ GeV/c \leq p_T^{asc} \leq 2.5\ GeV/c$ for associates, unless otherwise specified.

3.3 Correlation Functions

For the purpose of studies discussed in this dissertation one defines three correlation functions:

- two-particle azimuthal correlation function (Equation 3.1),
- two-particle ($\Delta\eta$, $\Delta\phi$) correlation function (Equation 3.2),
- three-particle azimuthal correlation function (Equation 3.3):

$$C_2(\Delta\phi) = \frac{N_{corr}(\Delta\phi)}{N_{mix}(\Delta\phi)} \frac{\int N_{mix}(\Delta\phi')\mathrm{d}(\Delta\phi')}{\int N_{corr}(\Delta\phi')\mathrm{d}(\Delta\phi')}, \tag{3.1}$$

$$C_2(\Delta\eta, \Delta\phi) = \frac{N_{corr}(\Delta\eta, \Delta\phi)}{N_{mix}(\Delta\eta, \Delta\phi)} \frac{\int N_{mix}(\Delta\eta', \Delta\phi')\mathrm{d}(\Delta\eta')\mathrm{d}(\Delta\phi')}{\int N_{corr}(\Delta\eta', \Delta\phi')\mathrm{d}(\Delta\eta')\mathrm{d}(\Delta\phi')}, \tag{3.2}$$

$$C_3(\Delta\phi_1, \Delta\phi_2) = \frac{N_{corr}(\Delta\phi_1, \Delta\phi_2)}{N_{mixABC}(\Delta\phi_1, \Delta\phi_2)} \frac{\int N_{mixABC}(\Delta\phi_1', \Delta\phi_2')\mathrm{d}(\Delta\phi_1')\mathrm{d}(\Delta\phi_2')}{\int N_{corr}(\Delta\phi_1', \Delta\phi_2')\mathrm{d}(\Delta\phi_1')\mathrm{d}(\Delta\phi_2')}, \tag{3.3}$$

where all N components are simply distributions of appropriate angles between trigger and associate particles (pairs of one trigger and one associate in Equations 3.1 and 3.2, triplets of one trigger and two associates in 3.3). In all N_{corr} distributions particles in each pair/triplet come from the same event, whereas in case of N_{mix} distributions each particle comes from a different event; the reason behind introduction of such components will be explained in Section 3.4.

At this point, it is worth pointing out a certain property of correlation functions defined this way: any significant change of amplitude of one side of such a function causes an opposite change on the other side. This fact is particularly easy to realise in a gedankexperiment assuming N_{mix} to be flat, as in this case normalisation of N_{corr} to unity can clearly be seen to propagate to the correlation function. It is important to be aware of this phenomenon while attempting interpretation of their shapes.

Below you will find a short description of why each of the three correlation functions has been introduced, along with what one expects to see analysing them. Since the methods as described here have so far been dedicated to searching for jets, as mentioned in Section 1.4.3, note that this description is partially based on basic assumption of the two-source model that the

only two significant sources of angular correlations are jets and flow. This assumption may or may not be correct in the SPS energy range; this will be addressed as needed now and in detail later.

Note: Many assumptions and considerations presented further on in this section and chapter are valid for all three correlation functions defined above. For brevity, most such points will only be discussed for two-particle azimuthal correlations. All differences between the three approaches will be stated explicitly wherever necessary.

3.3.1 Two-particle Azimuthal Correlations

A correlation function obtained from Equation 3.1 can be affected by a number of different phenomena. Although exact forms and magnitude of these contributions strongly depend on selected transverse momentum bins for trigger and associate particles, collision energy, centrality and system size, the following general effects can be expected:

- **Unmodified dijets** produce Gaussian-like peaks, with generally-different amplitude, on both near ($\Delta\phi \approx 0$) and away ($\Delta\phi \approx \pi$) side;
- **Medium-modified dijets** are expected to modify, and in some cases entirely quench, the shape of the away-side peak while not affecting the near-side one;
- **Flow** introduces sine-like modulation with primary peaks on both near and away side of the function;
- **Resonance decays** manifest themselves in a contribution to the near-side peak;
- **Global momentum conservation** manifests itself in the form of away-side correlation, as a result of associate particles balancing the high-p_T trigger.

3.3.2 Two-particle ($\Delta\eta$, $\Delta\phi$) Correlations

Two-particle azimuthal correlations are, by definition, one-dimensional. If more detailed spatial information about correlations is needed, two-particle *($\Delta\eta$, $\Delta\phi$)* correlations can be used. In the high-p_T realm, the primary reason for expanding angular correlations into two dimensions is that it allows one to search for the ridge phenomenon, as observed at the RHIC (see Figure 1.12). Unfortunately, splitting each $\Delta\phi$ bin into several $\Delta\eta$ bins severely worsens statistical uncertainty of results and as such requires very large data samples in order to allow comprehensive studies.

3.3.3 Three-particle Azimuthal Correlations

Results from RHIC experiments have proven two-particle azimuthal correlations to be highly effective in analysing heavy-ion collisions — not only have they demonstrated the presence

in most-central events of a hot, dense medium consisting of deconfined quarks and gluons but also provided evidence for that medium to be a strongly-interacting "perfect liquid" rather than formerly expected weakly-coupled gas-like plasma [81, 92]. Unfortunately, this approach is not able to provide information on how exactly jets are modified by the medium. Present-day knowledge of heavy-ion collisions tells us there are, as described in Section 1.4.4, two effects expected for strongly-coupled quark-gluon plasma to have on jets traversing it: bending and shock waves. Two-particle correlations are, as a statistical approach, unable to recognise which of the two effects is in fact active: widened, double-humped away-side peak can be explained by a cone appearing in each event just as well as by a deflected jet whose position fluctuates between events.

In response to the aforementioned problem, several different approaches have been developed to allow distinguishing between jet bending and conical flow. One of these approaches, three-particle azimuthal correlations, attempts to do this by combining each trigger particle with *two* associates instead of one — thus making the correlation function sensitive to the distribution of associate particles within events, allowing one to tell apart different predicted jet-modification scenarios (see Figure 3.7).

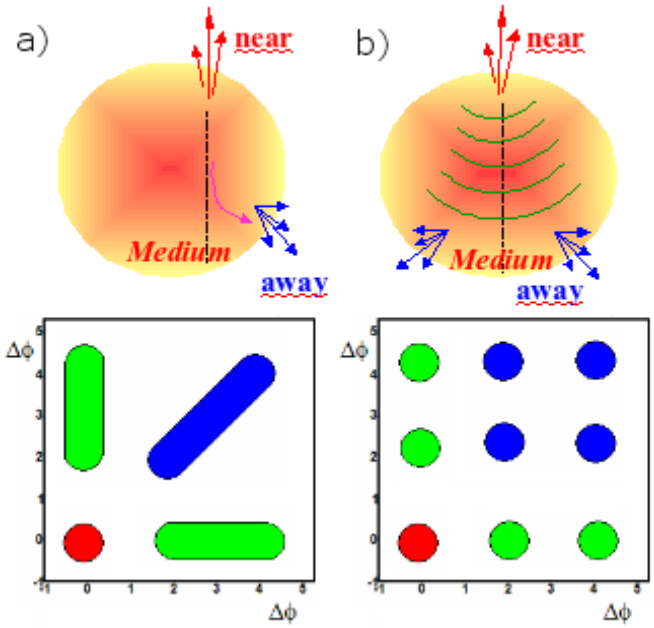

Figure 3.7: Illustrations (top) and diagrams of three-particle correlation functions (bottom) of different scenarios of interaction between jets and the medium: a) jet deflection, b) conical emission. Taken from [48].

Unlike two-particle ($\Delta\eta$, $\Delta\phi$) correlations, three-particle azimuthal correlations do not dilute available statistics. However, the fact particles are considered in triplets rather than pairs complicates extraction of different correlation sources. This will be discussed later on in this chapter.

3.3.4 Function Folding

By default same- and mixed-event distributions of $\Delta\phi$ used in the analysis, and by extension the correlation function itself, can be presented in the full angle of $\left[-\frac{\pi}{2},\ \frac{3}{2}\pi\right)$. On the other hand, as the correlations under consideration are expected to be symmetric around the back-to-back axis it is possible to reduce statistical errors by folding the function in half, into the $[0,\ \pi]$ range. This folding is performed on same- and mixed-event distributions before they are plugged into Equation 3.1, in accordance with the following formula:

$$\begin{gathered} N_{\cdot}^{folded}(\Delta\phi) = N_{\cdot}(\Delta\phi) + N_{\cdot}(\Delta\phi^*) \\ \text{where} \\ \Delta\phi^* = \begin{cases} -\Delta\phi & 0 < \Delta\phi \leq \frac{\pi}{2} \\ 2\pi - \Delta\phi & \frac{\pi}{2} < \Delta\phi \leq \pi \end{cases} . \end{gathered} \tag{3.4}$$

Note that in case of histograms, their bins must be symmetric around 0 and π in order to avoid unnecessary distortions of folding.

In case of two-particle ($\Delta\eta$, $\Delta\phi$) correlations a similar reasoning can be applied to $\Delta\eta$, allowing for reduction of statistical errors by folding it into non-negative range only. From practical point of view, the procedure is virtually identical to that employed for folding in $\Delta\phi$.

3.3.5 Quantification of Peaks

Sometimes it is useful to compare two or more correlation functions in a way that is more quantitative than simply putting them next to each other, for instance when behaviour of different part of the function is examined for dependence on some experimental variable. Examples of such cases which were encountered in the course of the analysis described in this dissertation, have been watching how the slope and/or amplitude of the two peaks of the two-particle azimuthal correlation function changes with collision energy, system size and electric charge of paired particles.

In order to quantify the slope of peaks we have performed function fits on the correlation functions in question (considering both systematic and statistical uncertainties), independently for two $\Delta\phi$ ranges:

- 0–0.75 (*i.e* the first 3 bins) to approximate the near-side peak;
- 1.85–π (*i.e.* the last 4 bins) to approximate the away-side peak.

Since all functions considered here have been folded into $[0,\ \pi]$ we were able to perform simple linear fits on both near and away side without significantly affecting fit quality:

$$C_2^{fit}(\Delta\phi) = slope \cdot \Delta\phi + intercept. \tag{3.5}$$

Results of these fits will be provided as required in Chapter 5; for now, Figure 3.8 presents an example of such a fit performed on central high-energy *Pb+Pb* data.

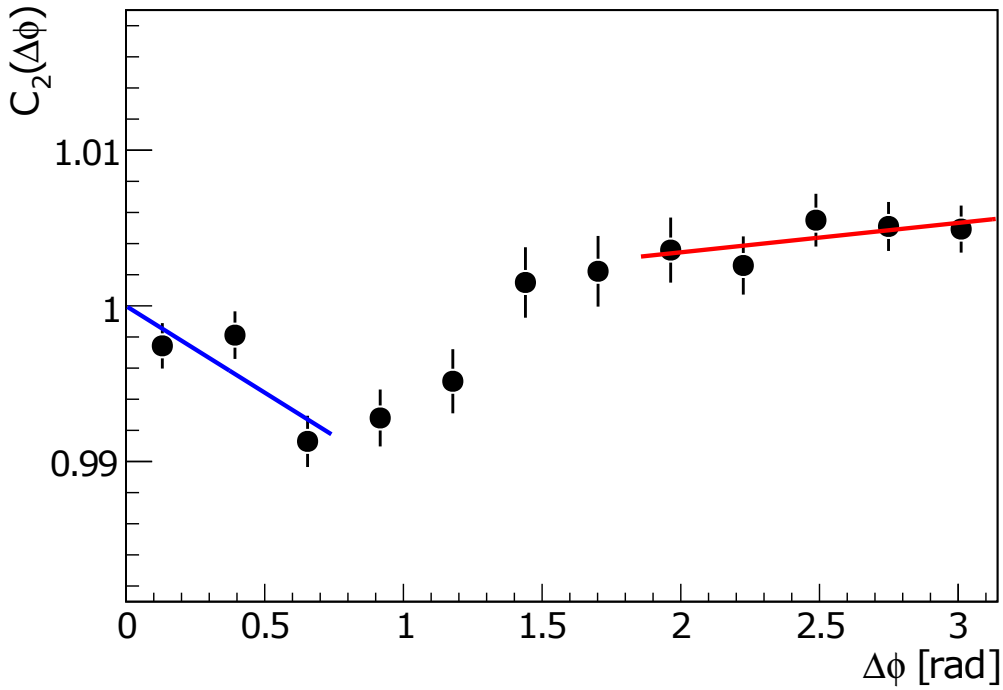

Figure 3.8: The two-particle azimuthal correlation function from central (0–5 %) *Pb+Pb* collisions at 158A GeV (full sample), with linear fits performed on its near- and away-side peak. For clarity, only statistical uncertainties have been plotted.

3.3.6 Per-trigger Yield

Correlation functions presented in this section can be used to, as the name suggests, illustrate correlations between particles, then again they only do it qualitatively. In order to quantify information provided by such functions one introduces so-called *per-trigger conditional yield* — a function which describes the number of associate particles produced per trigger particle at different angles with respect to that trigger:

$$J(\Delta\phi) = \frac{C_2(\Delta\phi)}{\int C_2(\Delta\phi')\mathrm{d}(\Delta\phi')} \frac{N^{TA}}{N_T}, \tag{3.6}$$

where N_T is the number of trigger particles, and N^{TA} — the number of same-event trigger-associate pairs. Assuming that the pair efficiency is the product of the single-particle efficiencies the trigger efficiency cancels out in the equation. Thus, the ratio is corrected for acceptance and reconstruction efficiency associate particles [93].

Note that while such a yield function can in principle be calculated for three-particle correlations just as well as for two-particle ones, its interpretation in such a case would be more

difficult due to more complex relationships between different correlation sources. In practice, three-particle correlations are usually used to produce qualitative results only.

3.4 Azimuthal Acceptance Corrections

In a perfect world, or at least while working with a detector with exactly uniform azimuthal acceptance, one could define an angular correlation function simply as an appropriately-normalised distribution of $\Delta\phi$ and/or $\Delta\eta$ for all acceptable trigger-associate pairs/triplets:

$$C(\alpha) = \frac{\mathrm{d}N}{\mathrm{d}\alpha} = N_{corr}(\alpha), \tag{3.7}$$

where α is $\Delta\phi$ for two-particle azimuthal correlations, $\Delta\eta$, $\Delta\phi$ for two-particle ($\Delta\eta$, $\Delta\phi$) correlations, or $\Delta\phi_1$, $\Delta\phi_2$ for three-particle azimuthal correlations.

Unfortunately, in real-world experiments such a distribution contains not only correlations with physical roots but also effects originating from non-uniformities in the detector's acceptance in azimuthal angle and/or pseudorapidity. Clearly, such artificial correlations must be accounted for if the results obtained in the course of such analyses are to be of any scientific significance.

The method most frequently employed to correct two-particle correlation functions for such effects is *event mixing*. In this approach, in addition to calculating the "raw" distribution from Equation 3.7 each selected trigger particle is paired with associates *from other events*[6]. Such mixed-event distributions do not, by definition, contain any physical correlations, while still featuring acceptance effects. The number of events selected for mixing is analysis-dependent; in general, it is kept relatively low to avoid excessive combinatoric overhead while high enough for the shape of the distribution to be stable. Basing on an investigation of such effects, illustrated by Fig. 3.9, we have decided to use **50 previous events** for mixing with each current one.

Number of mixed events aside, their selection too could positively or adversely affect the shape of mixed-event distributions. In the study described in this dissertation we have employed the **sliding window** approach, with events added to and removed from the window on the first-in, first-out approach; this reduces the number of times each associate particle is used in mixing. On top of that, events from the window are only mixed with the current one (with the former providing associate particles and the latter the triggers) and *never* with each other in order for each possible mixed-event pair to be used only once per analysis.

Last but not least, one may want events to be mixed to belong to certain classes, for instance to have similar multiplicity or position of the primary vertex. The purpose of such a constraint is to reduce so-called residual correlations, believed to at least partially originate from detector acceptance depending on properties of observed events. However, in this study we do **not** apply such classification and simply mix all events in considered centrality classes; the rationale

[6] In case of three-particle correlations each particle in a triplet must come from a different event.

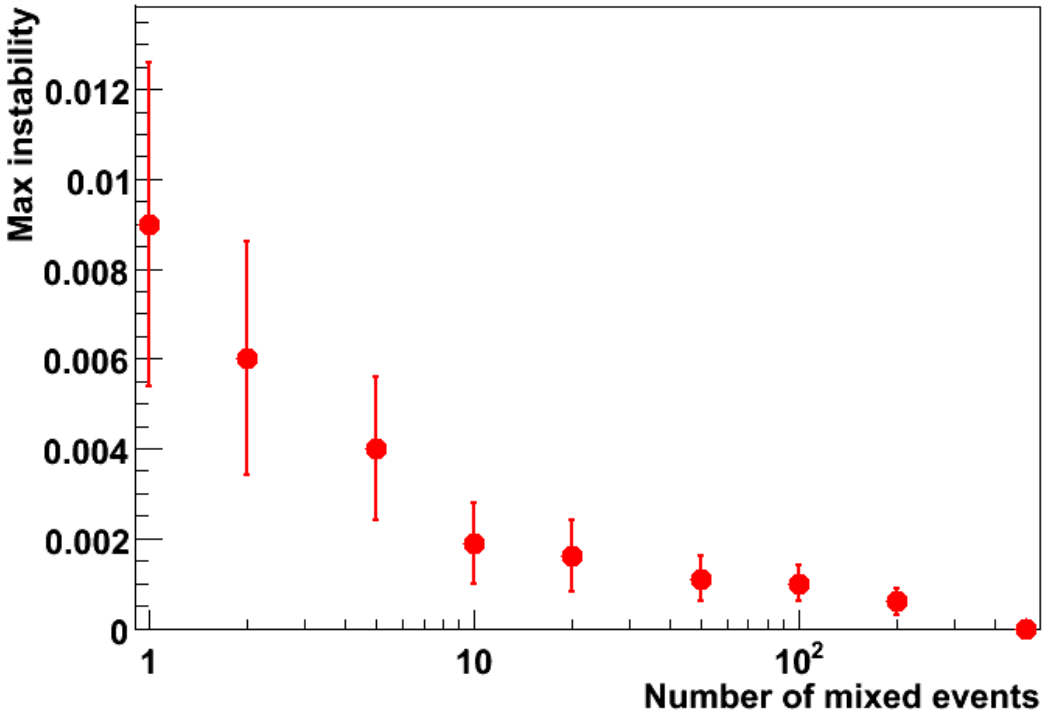

Figure 3.9: Stability of shape of mixed-event $\Delta\phi$ distributions as a function of length of the mixing queue. Abscissa: the number of previous events mixed with each new one. Ordinate: The largest deviation of the $N_{mix\ X}(\Delta\phi)/N_{mix\ 500}(\Delta\phi)$ ratio from unity.

behind this decision will be presented during discussion of systematic errors, in Section 4.2.

With all this in mind one can define an acceptance-corrected correlation function as

$$C(\alpha) \propto \frac{N_{corr}(\alpha)}{N_{mix}(\alpha)}, \tag{3.8}$$

where N_{corr} is the raw distribution, and N_{mix} – the one from event mixing. By adding appropriate normalisation factors one then obtains exact functions as shown in Section 3.3.

Figure 3.10 illustrates what $C_2(\Delta\phi)$ and its two components look like for NA49 acceptance.

3.5 The Two-source Model

Having obtained an acceptance-corrected correlation function there still remains the question of distinguishing different *physical* sources of azimuthal correlations — in addition to hard processes one can expect presence of particles correlated by soft scattering, having originated from the same decay or bulk properties of nuclear matter. The two-source model proposed by Ajitanand and collaborators, whose primary purpose is to allow extraction of hard signal from azimuthal correlations, postulates that the only non-negligible source of such correlations other

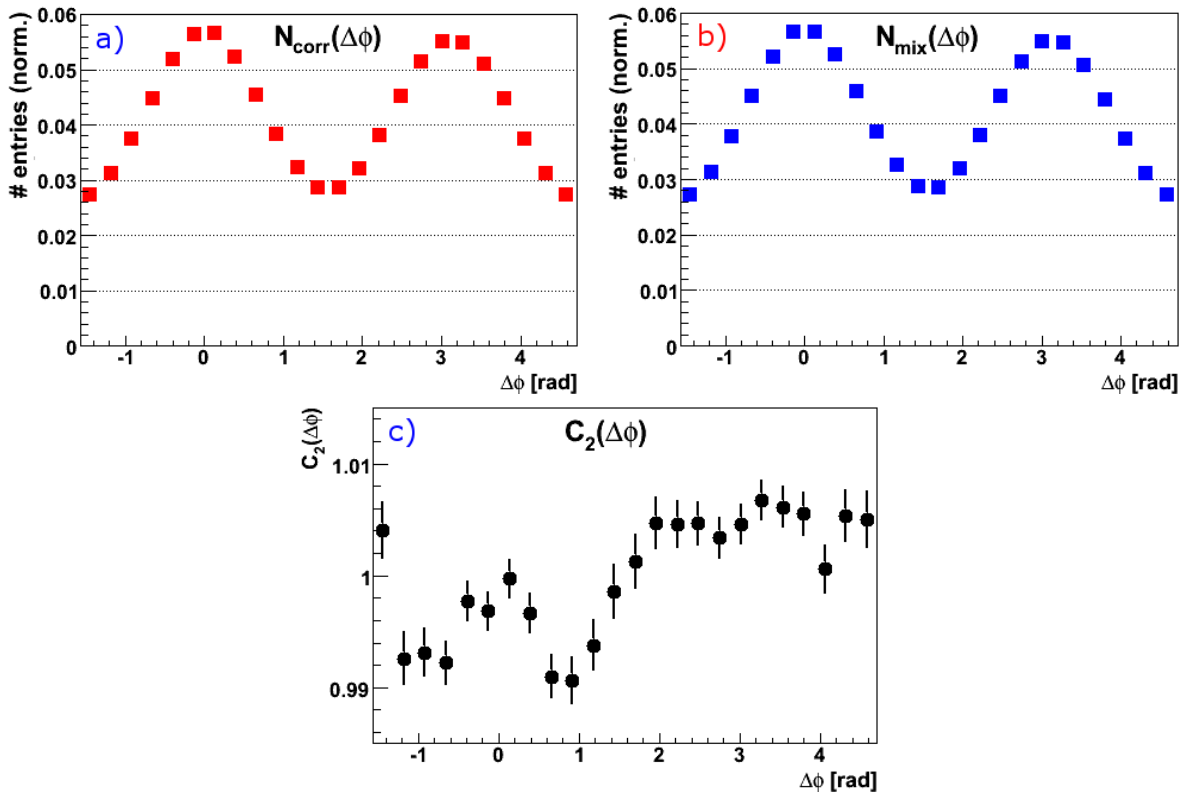

Figure 3.10: Illustration of the acceptance-correction procedure of angular correlation functions, on the example of two-particle azimuthal correlations in central (0–5 %) *Pb*+*Pb* collisions at 158A GeV, full available data sample: same-event distribution (a), mixed-event distribution (b) and the corrected correlation function which is a ratio of the two (c). $N_{corr}(\Delta\phi)$ and $N_{mix}(\Delta\phi)$ have both been normalised to unity and provided with horizontal grid lines to facilitate their visual comparison. It can be observed that while the uncorrected same-event distribution is very strongly dominated by acceptance effects, the procedure is capable of removing them and bringing out the correlation function's details.

than hard processes is flow, as described in Section 1.3.2 [94].

According to the two-source model the composition of a two-particle azimuthal correlation function can be described as follows:

$$C_2(\Delta\phi) = C_2^{jet}(\Delta\phi) + B_2(\Delta\phi), \tag{3.9}$$
$$B_2(\Delta\phi) = a\left[1 + 2\langle v_2^T v_2^A\rangle cos(2\Delta\phi) + 2\langle v_4^T v_4^A\rangle cos(4\Delta\phi)\right],$$

where $\langle v_n^T v_n^A\rangle$ can be approximated as $\langle v_n^T\rangle\langle v_n^A\rangle$, which in turn can be obtained in the course of an independent analysis [95]. Finally, the scaling factor a can be determined using the Zero Yield at Minimum (ZYAM) or Zero Yield at One (ZYA1) methods, described below.

Since flow is assumed not to depend on $\Delta\eta$, the same formula holds, barring different variants of C_2 and C_2^{jet} of course, for two-particle ($\Delta\eta$, $\Delta\phi$) correlations. Then again the situation is quite different for three-particle correlations; methods used to extract jet signal there will be described in the next section.

Eventually, one can modify per-trigger conditional yield from Equation 3.6 to provide information about distribution of *jet*-associate particles per *jet* trigger:

$$\hat{J}(\Delta\phi) = \frac{1}{N_T}\frac{\mathrm{d}N^{TA}_{(Di-)Jet}}{\mathrm{d}\Delta\phi} = \frac{C_2^{jet}(\Delta\phi)}{\int C_2(\Delta\phi')\mathrm{d}(\Delta\phi')}\frac{N^{TA}}{N_T}. \tag{3.10}$$

Controversy Despite being very widely used and appearing to work reasonably well, the two-source model in general and the ZYAM/ZYA1 assumptions are not universally accepted by the heavy-ion physics community. Fortunately in most central collisions, which are of primary interest to this study, it is possible to attempt interpretation of results by looking directly at raw correlation functions, which makes this concern relatively minor in the context of this dissertation. On the other hand, since the study does make certain use of the two-source model and ZYAM it is important to be aware of potential issues. A critical overview of this approach will therefore be provided in Chapter 6.

3.5.1 The ZYAM and ZYA1 Methods

If we accept predictions of the two-source model that no sources of azimuthal correlations other than hard scattering and flow have to be accounted for, we can take advantage of their known properties to estimate their mutual contribution in the data.

As the particles produced in hard processes are expected to be emitted as a back-to-back pair of collimated jets, we can expect their yield in the direction perpendicular to the dijet axis to be negligible — thus removing $C_2^{jet}(\Delta\phi)$ from Equation 3.9 and making it possible to determine the value of a.

The difference between ZYAM and ZYA1 lies in the way of selecting the value of $\Delta\phi$ for which the jet contribution to $C_2(\Delta\phi)$ is assumed to be zero. As the name suggests, in ZYAM we choose the point in such a way that it is the minimum of the resulting yield function, thus ensuring the latter shall never drop below zero; on the other hand, in ZYA1 one simply chooses the point for or the bin around $|\Delta\phi| = 1\ rad$. A combined approach, in which one looks for a minimum constrained to $|\Delta\phi| \approx 1\ rad$, is sometimes used as well.

3.6 Extraction in Three-particle Correlations

Just like in the two-particle case, $C_3(\Delta\phi_1, \Delta\phi_2)$ contains correlations originating from different physical sources — and again extraction of the hard signal is based on the two-source model. However, this is where the similarities between the two cases end: including the second associate particle makes the procedure significantly more complex than when only two particles at a time are considered.

At present three approaches exist which attempt to extract the hard component from three-particle correlations:

1. The method developed by the PHENIX Collaboration at the RHIC. In this approach, trigger-associate triplets are considered in the frame of reference in which the z axis is defined by the momentum vector of the trigger, with correlation functions plotted as a function of polar angle of one of associate particles and the difference in azimuthal angles of both associates (θ^* and $\Delta\phi^*$, respectively, in Figure 3.11) [96];

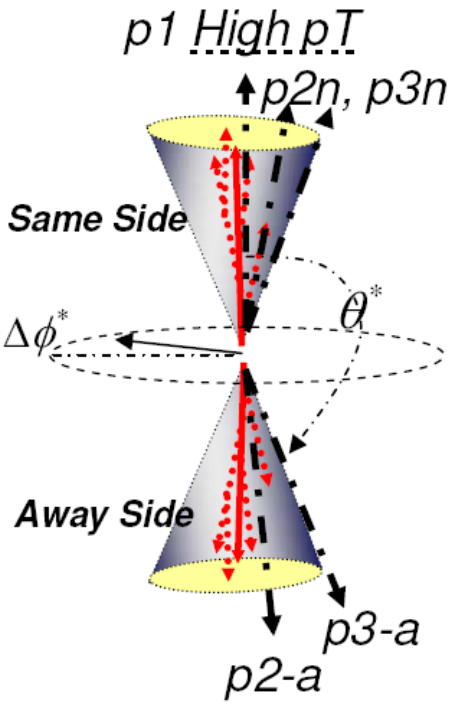

Figure 3.11: Schematic illustration of the coordinate system used for the three-particle correlation analysis by the PHENIX experiment. The high-p_T trigger particle serves as the near-side jet axis, *p2n* and *p3n* indicate associated particles on the near-side, *p2a* and *p3a* indicate associated particles on the away-side [96].

2. The *jet-correlation* method, developed by the STAR Collaboration at the RHIC, which conceptually is a simple extension of two-particle signal extraction [97];

3. The *cumulant* method, also developed by STAR, which is based on expressing ϕ distribution of particles in triplets as two- and three-particle cumulants as introduced by Berger in 1975 ([98]) and comparing them with cumulants produced from models of different processes [99].

In case of non-uniform detector acceptance one would expect the PHENIX method to be preferable, as it has been designed specifically for such an environment; unfortunately, its assumption that dijets are oriented back-to-back not only in azimuthal angle but also in pseudorapidity is controversial, as it doesn't match observations from other RHIC experiments. The cumulant approach on the other hand is strongly model-dependent, which is a problem when working

with high-p_T particles in the SPS energy range (this problem was described in Section 1.4.5). Therefore, the approach discussed further on in this dissertation is the jet-correlation method. This has a side benefit of facilitating result comparison with the CERES experiment at the SPS, which chose the same approach for their analysis [100].

In the context of the jet-correlation signal extraction method, relationship between different components of a three-particle correlation functions can be symbolically written as

$$\begin{aligned} C_3(\Delta\phi_1, \Delta\phi_2) &= (hard \oplus soft) \otimes (hard \oplus soft) \\ &= (hard \otimes hard) \oplus (hard \otimes soft) \oplus (soft \otimes soft), \end{aligned} \tag{3.11}$$

where $C_3(\Delta\phi_1, \Delta\phi_2)$ is calculated from experimental distributions as shown above, $(hard \otimes hard)$ is the component we are looking for and the other components need to be estimated in order to be removed. Expressing this relation quantitatively in accordance with the prescription, we arrive at

$$C_3(\Delta\phi_1, \Delta\phi_2) = C_3^{jet}(\Delta\phi_1, \Delta\phi_2) + a\left(C_2^{jet} \otimes B_2\right)(\Delta\phi_1, \Delta\phi_2) + ba^2 B_3(\Delta\phi_1, \Delta\phi_2). \tag{3.12}$$

The hard-soft term $C_2^{jet} \otimes B_2$ can be obtained by folding two-particle function components from Equation 3.9:

$$\left(C_2^{jet} \otimes B_2\right)(\Delta\phi_1, \Delta\phi_2) = C_2^{jet}(\Delta\phi_1)B_2(\Delta\phi_2) - C_2^{jet}(\Delta\phi_2)B_2(\Delta\phi_1). \tag{3.13}$$

The factor a also comes from two-particle calculations.

The soft-soft component B_3 on the other hand is defined as a sum of two distinct components:

- Soft (flow) correlations between associate particles, described well by a distribution we shall call $N_{mixABB}(\Delta\phi_1, \Delta\phi_2)$: in each triplet, the trigger and both associate particles come from *two* different events. Note that should this distribution be considered on its own it would reintroduce effects of non-uniform azimuthal acceptance into the result, in an attempt to avoid this we divide N_{mixABB} by the three-event mixed-event distribution;
- Soft correlations between trigger and associate particles, which are not present in N_{mixABB}. These can be included analytically:

$$\begin{aligned} B_3^{TF}(\Delta\phi_1, \Delta\phi_2) = {} & 2\langle v_2^T\rangle\langle v_2^{A1}\rangle cos(2\Delta\phi_1) + 2\langle v_2^T\rangle\langle v_2^{A2}\rangle cos(2\Delta\phi_2) \\ & + 2\langle v_4^T\rangle\langle v_4^{A1}\rangle cos(4\Delta\phi_1) + 2\langle v_4^T\rangle\langle v_4^{A2}\rangle cos(4\Delta\phi_2) \\ & + 2\langle v_2^T\rangle\langle v_2^{A1}\rangle\langle v_4^{A2}\rangle cos(2\Delta\phi_1 - 4\Delta\phi_2) \\ & + 2\langle v_2^T\rangle\langle v_2^{A2}\rangle\langle v_4^{A1}\rangle cos(4\Delta\phi_1 - 2\Delta\phi_2) \\ & + 2\langle v_2^{A1}\rangle\langle v_2^{A2}\rangle\langle v_4^T\rangle cos(2\Delta\phi_1 + 2\Delta\phi_2), \end{aligned} \tag{3.14}$$

where all the v_n factors can, like with two-particle correlations, be obtained in the course

of an independent analysis.

With all the background terms and the factor a known all that remains is to determine the value of the factor b. One of the possibilities of doing so is to once again enlist the help of ZYAM or ZYA1 and assume that for some values of $\Delta\phi_1$ and $\Delta\phi_2$ the hard-hard component of the correlation function becomes negligible. With that in mind,

$$b = \frac{C_3(\Delta\phi_1^*, \Delta\phi_2^*) - a\left(C_2^{jet} \otimes B_2\right)(\Delta\phi_1^*, \Delta\phi_2^*)}{a^2 B_3(\Delta\phi_1^*, \Delta\phi_2^*)}, \tag{3.15}$$

with $\Delta\phi_1^*$ and $\Delta\phi_2^*$ chosen to follow either ZYAM or ZYA1.

Note: Given the above reasoning stems from assumptions of the two-source model, one would expect signal extraction of this sort to be unnecessary for most central events, where the flow component is virtually absent. Should this not be the case, such a phenomenon could indicate problems with the two-source model.

3.6.1 Jet-correlation Difficulties

The major difficulty associated with applying the jet-correlation method to three-particle correlation studies is required precision, as the method in question is very sensitive to any uncertainties introduced in the process. Even at RHIC energies one needs to achieve precision of 10^{-4}, both statistically and systematically [97]. At the SPS, where both yield of high-p_T particles and contribution of jets to total particle production are considerably lower, this is even more difficult. For a central *Pb+Pb* collision at 158A GeV, the number of charged particles around mid-rapidity ($2 < \eta < 4$) for the transverse momentum range of $1 < p_T < 2.5\ GeV/c$ is about 21, whereas the dijet charged hadron multiplicity within the same associate p_T range and trigger-particle p_T range of $2.5 < p_T < 4\ GeV/c$ is of the order of 0.05. This yields the signal-to-background ratio of the order of 1/420, meaning that the hard-soft background is a factor of 420 larger than three-particle correlation strength and that the soft-soft background is a factor of 10^5 larger. Result — a need for immensely high precision of 10^{-6}!

The second issue lies with the fact that, as suggested in Section 1.4.5, in the energy range of CERN SPS correlations originating from hard processes and flow may be accompanied by significant contributions from other sources, not considered significant by the two-source model (a critical overview of the model can be found ahead, in Section 6.1.3). This issue is a mixed blessing: on one hand if we want to concentrate on non-jet correlation sources the aforementioned precision requirement can be made much less severe, on the other — given the goal of three-particle correlation studies is to distinguish different scenarios of jet-medium interactions, they may be entirely inapplicable (or at least unnecessary) if non-jet, non-flow sources are dominant.

Last but not least, the jet-correlation extraction method has been designed for use in experiments whose detectors feature practically-uniform azimuthal acceptance, which is obviously

not the case with NA49. To our knowledge the analysis described in this dissertation is the first attempt of using this approach in an azimuthally non-uniform detector set-up, making it possible that in spite of discussions with the method's authors regarding how to address the matter, acceptance effects will not have been entirely accounted for. Moreover, intrinsic complexity of this approach along with the similarity of shape between the signal and acceptance effects make it highly difficult to decide whether the latter have or have not been removed.

In light of the above , it is not possible to tell in advance whether three-particle azimuthal correlations can in fact be applied to NA49 data analysis. Our attempt to evaluate the usefulness of this approach in our case can be found in Appendix E.

Chapter 4

Errors

Analysis procedures described in the previous chapter are of course not perfect, even if only because of applying statistical approaches to data sets of finite, and often quite limited, size. Here we would like to describe what errors are expected to be associated with our results and how we account for them.

4.1 Statistical Errors

Statistical uncertainties of bin values in same- and mixed-event $\Delta\phi$ and ($\Delta\eta$, $\Delta\phi$) distributions are calculated as $\sqrt{N}$, where N is the bin content. The underlying assumption behind this approach is that entries into distributions come from independent, uncorrelated measurements. We know this to be true in the case of same-event distributions, as each event, associate particle and trigger–associate pair are only ever used once. In case of mixed-event distributions on the other hand, where each event is used up to 50 times, this possibility has not been ruled out even though we still only enter each trigger–associate pair only once — however, statistical errors in this case are so small (less than 0.05 %) the effect of any possible discrepancies can be considered negligible.

During scaling, *i.e.* while normalising angular distributions to unity or calculating per-trigger conditional yield, new error values are also obtained by simple scaling: $c\sqrt{N} = \sqrt{c^2 N} = \sqrt{cN_{scaled}}$, where c is the scaling factor.

If folding is requested, errors from each two folded bins are added to each other in quadrature, yielding statistical errors in the form $\sqrt{N^2 + N'^2}$.

Finally, when the two distributions are divided by each other to produce the correlation function, the latter's statistical errors are defined as

$$\delta C = \begin{cases} \sqrt{\frac{\delta N_{corr}^2 \dot{N}_{mix}^2 + \delta N_{mix}^2 \dot{N}_{corr}^2}{N_{mix}^4}} & N_{mix} > 0 \\ 0 & N_{mix} = 0 \end{cases} . \tag{4.1}$$

4.2 Systematic Errors

Following the discussion of statistical errors, in this section we discuss systematic ones. We begin with a brief overview, followed by an in-depth description of procedures and results for different sources, accompanied by example plots.

The following sources of systematic errors are considered pertinent to the analysis described in this dissertation:

1. contamination of the sample by secondary tracks incorrectly classified as primary — estimated by varying the track impact parameter ($\vec{b}$) cut;

2. contamination by split tracks — estimated by varying the cut on the ratio of the number of a track's points in all TPCs to the estimated maximal number of such points (N_{points}/N_{max});

Furthermore, if function folding is in effect a lower-limit estimation of systematic uncertainties can be obtained by examining asymmetry of $\Delta\phi$ distributions with respect to the back-to-back axis; this is done by comparing bins which from the point of view of physics are supposed to have content differing only by statistical fluctuations.

All the three contributions are added in quadrature to obtain final systematic uncertainties of correlation functions. Since these uncertainties generally change between bins, let alone between different data sets, it would be impractical to list them all here. Instead, they will be shown along with functions they pertain to, plotted as gray boxes added to points, in the Results chapter. That said, for illustrative purposes Figure 4.1 presents systematic uncertainties obtained for two-particle azimuthal correlation functions, both in the full range of azimuthal angle and folded into $[0, \pi]$.

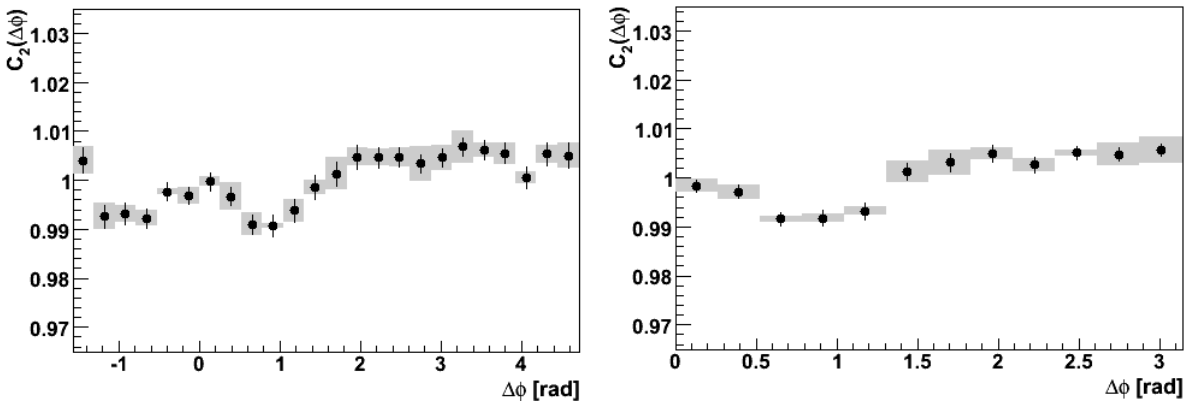

Figure 4.1: An example of systematic errors, shown as gray boxes, on full-range (left) and folded (right) two-particle azimuthal correlation functions from 0–5 % *Pb*+*Pb* events at 158A GeV.

In addition to the above, a number of other sources have been investigated and found to be negligible:

1. Finite two-track resolution of the NA49 apparatus;

2. Indiscriminate selection of events for mixing;

3. The cut on the minimal number of track points;

4. The "broken tracks" cut.

These sources are not included in final systematic uncertainties.

4.2.1 Included Sources

As mentioned above, contamination by secondary and split tracks is estimated by varying the thresholds of cuts on $\vec{b}$ and N_{points}/N_{max}, respectively. Example distributions of the two quantities, (from central *Pb+Pb* collisions at 158A GeV) are shown in Figure 4.2. Basing on such distributions, two sets of values have been chosen for each cut around those used in the analysis proper, close enough to the main ones for the change not to significantly affect the correlation function's statistical errors. The correlation functions obtained by independently varying the two cuts (examples of whose can also be found in Figure 4.2), are then subtracted from each other, and the maximum of these subtractions is selected as the value of the error for the given $\Delta\phi$.

In order to estimate systematic uncertainties originating from folding we compare histogram bins which are merged, as described in Section 3.3.4, to see how much they differ from each other. The procedure must of course account for statistical uncertainties of compared bins in order to avoid double-counting such errors. By that logic, the folding-related component of systematic uncertainty has been defined as:

$$\delta_{sys}^{fold}(C_2) = \begin{cases} A(\Delta\phi) & A(\Delta\phi) > 0 \\ 0 & A(\Delta\phi) \leq 0 \end{cases}$$
$$\text{where} \tag{4.2}$$
$$A(\Delta\phi) = |C_2(\Delta\phi) - C_2(\Delta\phi^*)| - \sqrt{[\delta_{stat}C_2(\Delta\phi)]^2 + [\delta_{stat}C_2(\Delta\phi^*)]^2},$$

with $\Delta\phi^*$ defined as shown in Equation 3.4.

4.2.2 Neglected Sources

Two-track resolution The fact that two-track resolution of the apparatus is finite means that if two tracks lie very close to each other in space, some or all of their points may be impossible to tell apart in the data. This effect is particularly important when track density in a collision is high, *i.e.* in high-energy heavy-ion collisions. In two-particle angular correlations it could be visible as depletion of the centre of the near-side peak of the function, especially in the ($\Delta\eta$, $\Delta\phi$) case. In order to estimate the role of this issue in the analysis described in this dissertation we have applied a cut on minimal distance between two tracks, which is described in detail in

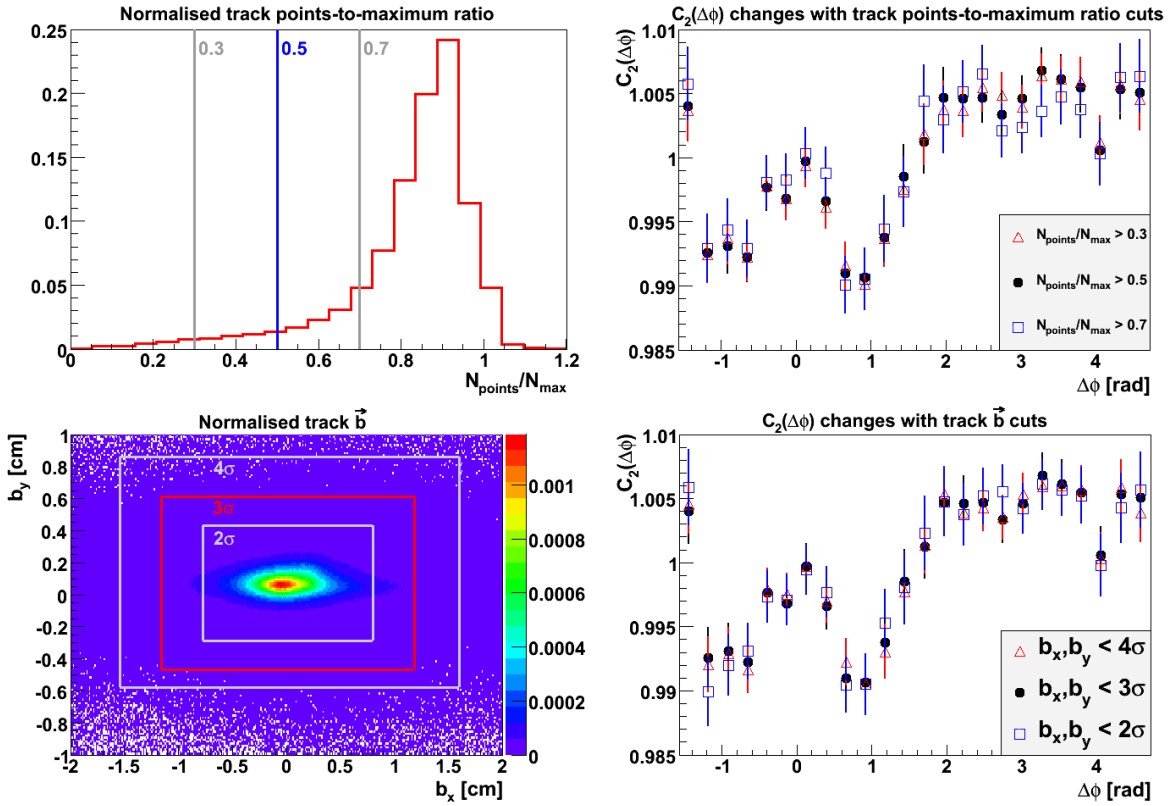

Figure 4.2: **Left**: Distributions of the track impact parameter (top) and the TPC N_{points}/N_{max} ratio (bottom) obtained from 25,000 0–5 % *Pb+Pb* at 158A GeV events. Lines superimposed on the histograms indicate the values used in the process of estimating systematic errors on the correlation function, with coloured labels indicating those used in the analysis proper. **Right**: Correlation functions resulting from variation of those parameters.

Appendix C, to the data to produce correlation functions expected to be free from such effects, then compared them to those without such a cut. As one can see in Figure 4.3, the effect is very small even in the two-dimensional case (1D: up to 0.2 % at 0 and 0.05 % elsewhere; 2D: up to 2 % at (0,0) and 0.5 % elsewhere) and as such can be neglected in error calculations.

Event-mixing classes Another possible source, this time applying to mixed-event distributions N_{mix} rather than to correlation functions themselves, could be selection of events for mixing — it is known that for many classes of analyses, the shape of such distributions depends on whether one mixed events of similar type (classified *i.e.* by multiplicity) or indiscriminately. In order to estimate the magnitude of this effect in the analysis in question we have compared $N_{mix}(\Delta\phi)$ obtained by indiscriminate mixing with those from the case of mixed events having their multiplicity differ by no more than 20 %; example results of such a comparison can be found in Figure 4.4. As it turns out, the difference between the two cases is so small (less than 0.1 %!) the effect of mixing selection can be considered negligible.

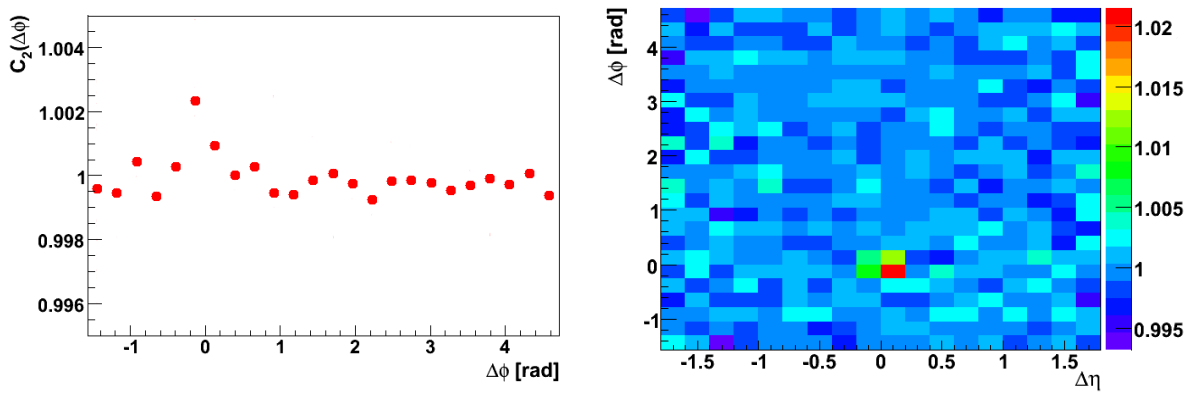

Figure 4.3: Ratio of two-particle azimuthal (left) and two-particle ($\Delta\eta$, $\Delta\phi$) (right) correlation functions obtained with (in nominator) and without (in denominator) the minimal-distance cut on track pairs. All four functions have been produced from the whole available sample of 0–5 % *Pb+Pb* at 158A GeV events.

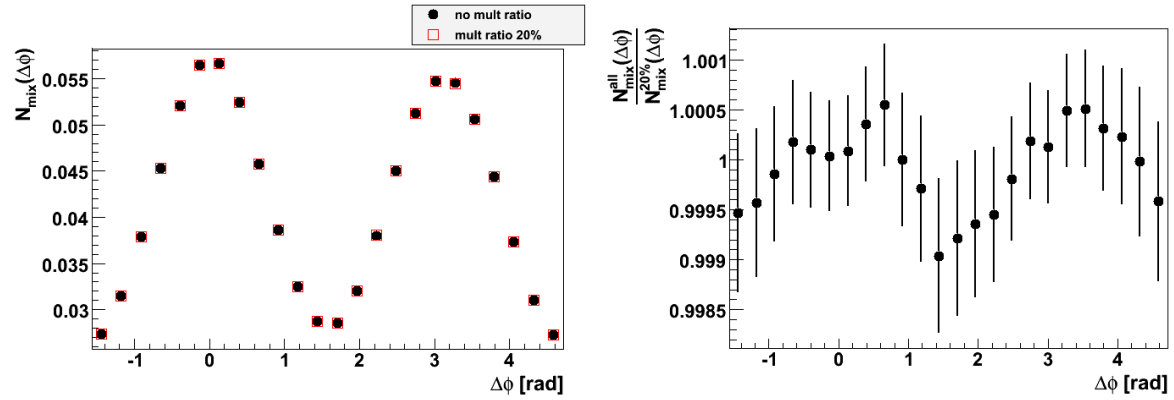

Figure 4.4: **Left**: Two-particle azimuthal mixed-event distributions obtained from 250,000 central (0–5 %) *Pb+Pb* events at 158A GeV, obtained either indiscriminately (full black dots) or requiring the multiplicity of mixed events to differ by no more than 20 percent (open red squares). **Right**: A ratio of the two distributions.

Number-of-points cut The next possible source of systematic errors is the contribution of short tracks, controlled by cutting on the minimum number of track points from all TPCs. Two two-particle azimuthal correlation functions obtained for different values of this cut — no limit and 30 — from central *Pb+Pb* collisions at 20A GeV, can be found in Figure 4.5; a low-energy data set has been used instead of the 158A-GeV one because this effect becomes more relevant with decreasing collision energy. It can be observed that introducing the N_{points} cut visibly increases statistical errors (it removes approximately 40 % tracks in the associate p_T range and up to as much as 70 % tracks in trigger range); as for the vast majority of points this uncertainty entirely accounts for the difference between the two functions, addressing these differences again in the form of contribution to systematic uncertainties has been declared unnecessary.

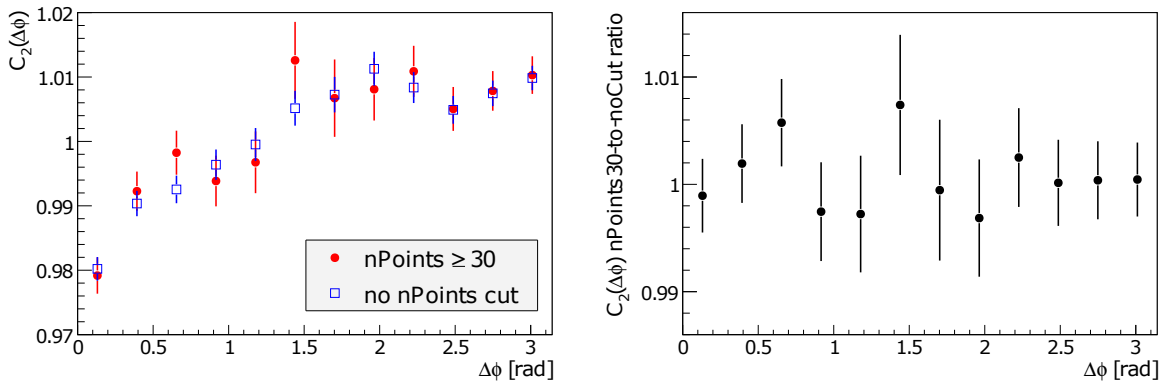

Figure 4.5: **Left**: Two-particle azimuthal correlation functions from full available sample of central (0–5 %) *Pb*+*Pb* events at 20*A* GeV obtained for two thresholds on the minimum number of track points from all Time Projection Chambers: for full red circles a minimum of 30 was required, for open blue squares no threshold was set. **Right**: A ratio of the two functions.

Broken-track cut Finally, A. László's broken-track cut could also affect the shape of correlation functions. In order to estimate this particular effect we have compared two-particle azimuthal functions obtained with the cut threshold set to its default value and with the cut disabled, respectively. Again, as shown in Figure 4.6, the effect on the correlation function was found to be negligible — less than 0.2 %.

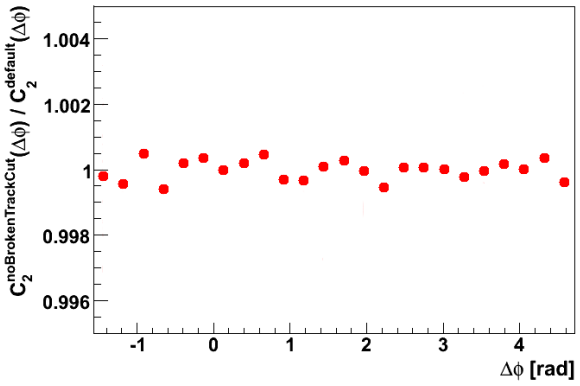

Figure 4.6: A ratio of two-particle azimuthal correlation functions from full available sample of central (0–5 %) *Pb*+*Pb* events at 158*A* GeV, obtained without (in nominator) and with (in denominator) A. László's broken-track cut.

4.2.3 Discussion of Magnitude

Systematic uncertainties measured in the course of this study are generally of similar magnitude as statistical ones. In quite a large number of bins, statistical errors are in fact larger than systematic ones; there are only a few case of the opposite and even there the ratio of the two doesn't

exceed approximately 1:2. Folding doesn't appear to significantly modify this behaviour, thus confirming the viability of employing it to improve overall quality of results. Last but not least, combined systematic and statistical errors remain small enough comparing to the measured signal to allow drawing meaningful conclusions from observed function shapes.

4.2.4 Effects of Contamination

A risk always exists that some fraction of background tracks make it into the data sample despite the cuts. In case of NA49 such background can, due to properties of the detector, be expected to manifest itself in the p_T range of trigger particles. A question arises: how would such tracks, appearing where the cross-section on particle production is quite low — according to our simulations of central *Pb+Pb* collisions, particles with p_T between 2.5 and 4 GeV/c are on average produced in every other 158A GeV event and only in every fifth 20A GeV event — and as such capable of significantly distorting the trigger sample, affect the correlation function?

In order to estimate that effect we have taken advantage of simulated data sets produced for the purpose of comparison of our results with models, as described below in Section 6.3. Two two-particle azimuthal correlation functions were produced: one containing only model data (100,000 central *Pb+Pb* events at 20A GeV) and one with manually-added background tracks with the following properties:

- transverse momentum chosen at random from our default trigger-particle range of 2.5–4 GeV;
- randomly distributed in η range of 2–4;
- randomly distributed in the full angle of ϕ.

Such tracks were randomly injected into model data after cuts at a rate of **0.05** per event. This particular value has been chosen on purpose: with the trigger-particle rate in experimental data of the same type being 0.25 per event, it provides a good worst-case estimation by assuming all the surplus with respect to simulated data (about 0.2 per event, as mentioned above) to have originated from background contamination.

Examining the ratio of the two correlation functions, provided in Figure 4.7, it can be noted immediately the observed discrepancies both are no larger than 0.5 % and remain within statistical errors of measurements. Therefore, it can be concluded that two-particle azimuthal correlation functions are not sensitive to contamination of the trigger-track sample.

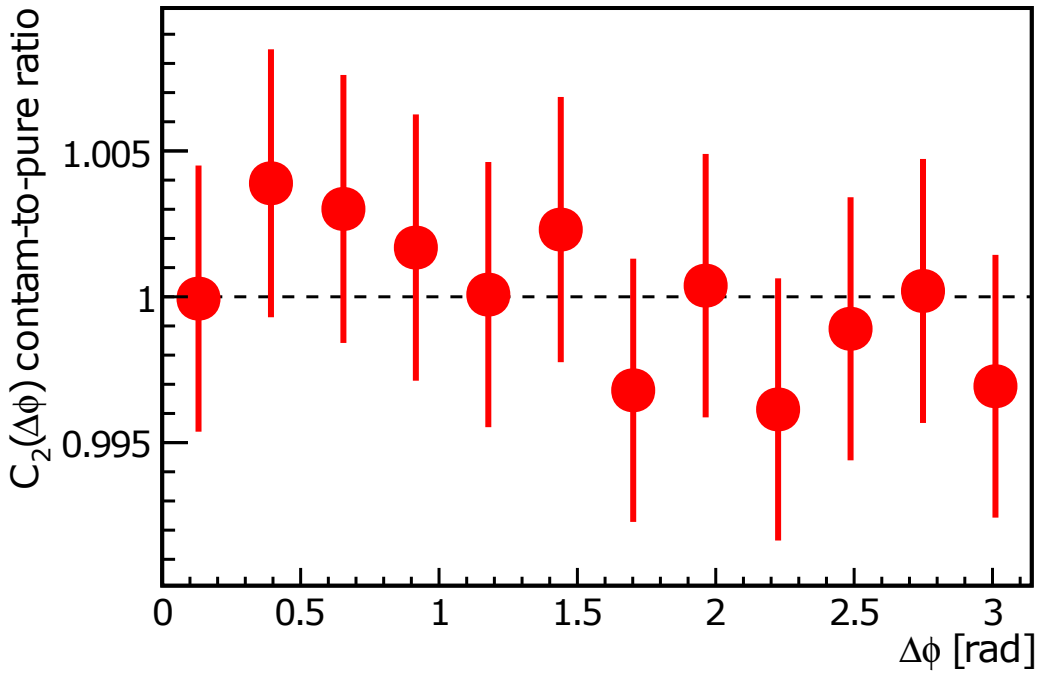

Figure 4.7: A ratio of two-particle azimuthal correlation functions from 100,000 simulated central *Pb+Pb* events at 20*A* GeV, produced to examine the effect of random trigger-like background tracks on correlations. Nominator: function based on unmodified model data. Denominator: function from model data mixed with random trigger-like tracks. All errors are statistical only.

Chapter 5

Results

This chapter is devoted to presenting results obtained using two-particle angular-correlation techniques from NA49 data in the course of the study described in this dissertation. They have been sorted into a number of sections, each dedicated to a different part of the analysis. Additionally, Appendix E presents our first take on three-particle azimuthal correlations in NA49.

As a reminder, the following systems — detailed descriptions of whose can be found in Table 2.1 — have been analysed in the course of this study:

- *Pb*+*Pb* at 158A GeV, centrality 0–5 %;
- *Pb*+*Pb* at 158A GeV, centrality 5–10 %;
- *Pb*+*Pb* at 158A GeV, centrality 10–20 %;
- *Si*+*Si* at 158A GeV, centrality 0–5 %;
- *p*+*p* at 158 GeV;
- *Pb*+*Pb* at 80A GeV, centrality 0–5 %;
- *Pb*+*Pb* at 40A GeV, centrality 0–5 %;
- *Pb*+*Pb* at 30A GeV, centrality 0–5 %;
- *Pb*+*Pb* at 20A GeV, centrality 0–5 %.

Events and track cuts applied to these data sets have been listed in Tables 3.2 and 3.3, respectively; no cuts have been made on azimuthal angle or rapidity (see example acceptance plots in Figure 5.1 as well as Appendix B for their complete collection). Particles were divided by transverse momentum into triggers and associates, with $2.5\ GeV/c \leq p_T^{trg} \leq 4.0\ GeV/c$ and $1.0\ GeV/c \leq p_T^{asc} \leq 2.5\ GeV/c$ in all parts of the study unless explicitly stated otherwise.

On all function plots we indicate statistical errors with lines and systematic ones with boxes.

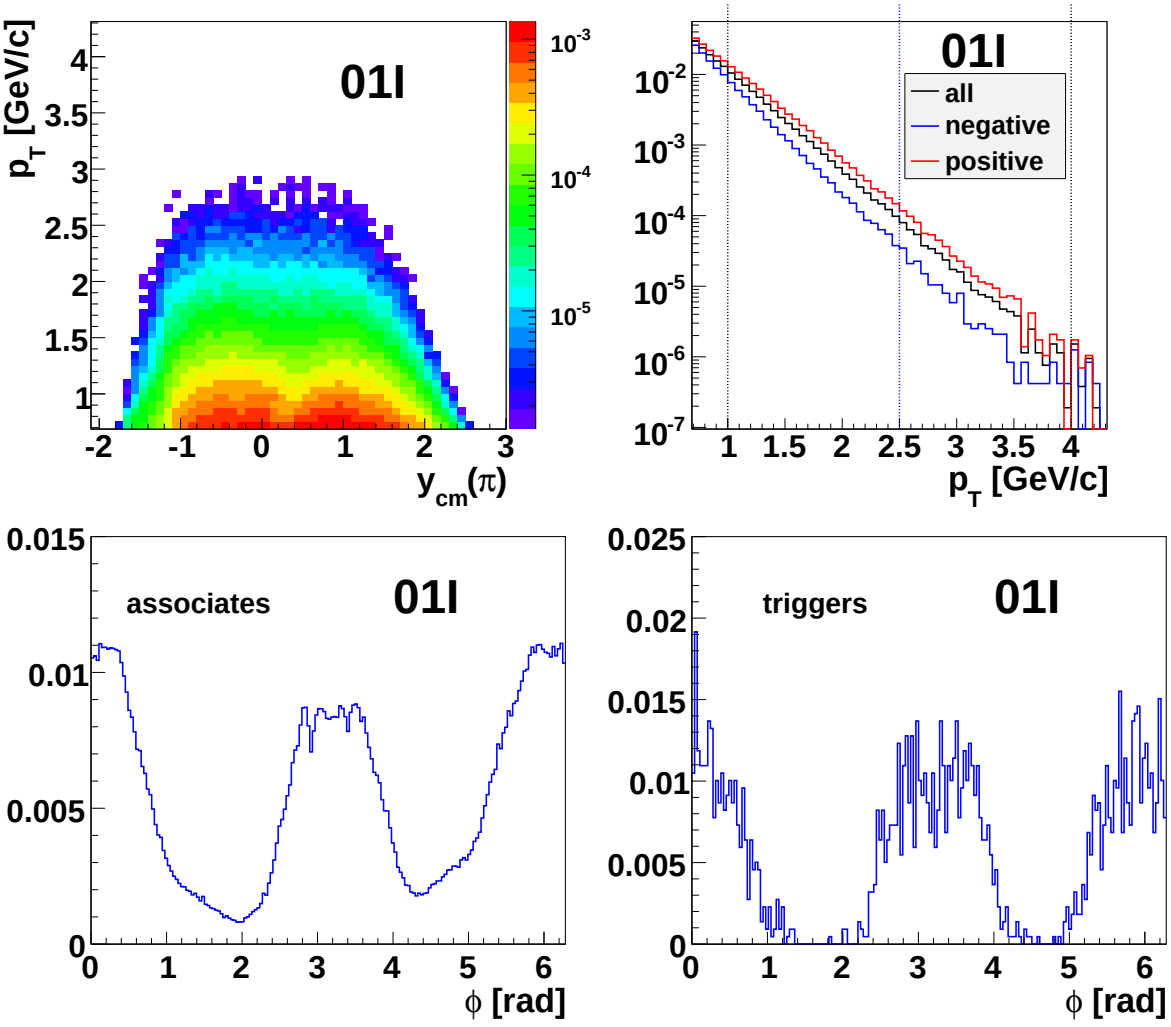

Figure 5.1: Distributions of transverse momentum *vs.* pion-mass rapidity (top left), transverse momentum (top right), azimuthal angle of associate particles (bottom left) and azimuthal angle of triggers (bottom right) in 10,000 0–5 % *Pb*+*Pb* at 158*A* GeV events, provided as an example of acceptance plots for analysed data sets. See Appendix B for their full collection.

5.1 Two-particle Azimuthal Correlations

The primary purpose of this part of the analysis has been to determine whether it is possible to observe modification of shape of the away side of the correlation function in central *Pb*+*Pb* collisions at top SPS energy, as well as to attempt determining whether this modification is caused by medium–jet interactions. This has been done by investigating two-particle azimuthal correlation functions in four scans:

1. Centrality scan of *Pb*+*Pb* events at 158*A* GeV;
2. Different pairings of the electric charge of trigger and associate particles, in central *Pb*+*Pb* events at 158*A* GeV;
3. System-size scan of central collisions at 158*A* GeV;

Centrality	v_2^T	v_2^A	v_4^T	v_4^A
0–5 %	0.022 ± 0.003	0.01395 ± 0.00027	0.011 ± 0.003	0.00282 ± 0.00027
5–10 %	0.073 ± 0.003	0.04079 ± 0.00029	0.006 ± 0.003	0.00533 ± 0.00029
0–20 %	0.117 ± 0.003	0.06570 ± 0.00026	0.017 ± 0.003	0.00518 ± 0.00026

Table 5.1: Second- and fourth-order flow coefficients used in the analysis. Only statistical errors are listed [101].

4. Energy scan of central-*Pb*+*Pb* data.

Moreover, we have compared some of our results with those obtained by other experiments at the SPS and RHIC.

5.1.1 Centrality Dependence in *Pb*+*Pb* Collisions at 158A GeV

The top row of Figure 5.2 shows two-particle azimuthal correlation functions produced from the *011* data set, for three centrality ranges: 0–5, 5–10 and 10–20 %. Lines overlaid on each function illustrate flow contribution to each range, estimated using v_2 values obtained independently using the reaction-plane method (see Table 5.1) and scaled in accordance with the ZYAM assumption. Finally, per-trigger conditional yield for each centrality bin can be found in the bottom row of the figure.

Results of the centrality scan show a wide plateau on the away side of the correlation function for most central collisions, visible even before flow subtraction. Conversely, away side of conditional yield in the two more peripheral bins is Gaussian-like. These observations are consistent with predictions of presence of quark-gluon plasma in most-central high-energy heavy-ion collisions.

Last but not least, Figure 5.3 shows the correlation function from the 0–5 % bin folded into $[0,\ \pi]$, which will be used as reference in comparison with other, smaller NA49 data sets used in this analysis. This particular centrality bin has been chosen due to not only considerations related to available sample sizes but also in light of potential issues pertaining to subtraction of flow from correlation functions; in most central collisions contribution of flow is negligible, making it possible to avoid such issues by comparing the functions themselves. In order to improve clarity of such comparisons we have decided to, rather than use the function itself, parametrise it with polynomials and use that instead. The function we have used is shown in Equation 5.1:

$$\begin{cases} ax^3 + bx^2 + cx + d & \Delta\phi < 1.45 \\ ex + f & \Delta\phi \geq 1.45 \end{cases}, \tag{5.1}$$

where the value *1.45* has been chosen instead of exactly $\pi/2$ to make the function continuous. This parametrisation fits the data it has been based on with $\chi^2/NDF = 3.26/6$.

5.1.2 Inter-experiment Comparison

In Figure 5.4 we compare two-particle correlation functions and per-trigger conditional yield obtained from central heavy-ion collisions by two different experiments at the CERN SPS: the NA49 function from 0–5 % *Pb+Pb* events at 158*A*, as shown in Figure 5.3, is compared to a preliminary function obtained at the same beam energy in 0–5 % *Pb+Au* collisions, by the NA45/CERES Collaboration [100]. The comparison is facilitated by the fact both analyses have used the same transverse momentum bins for trigger and associate particles.

Good agreement can be observed between results from NA49 and CERES.

For reference, Figure 5.5 provides per-trigger conditional yield from central *Au+Au* collisions at 200 GeV/nucleon, from PHENIX and STAR experiments at the RHIC[1] [79, 102]. Unfortunately the two experiments use different centrality and transverse-momentum bins in their studies, making a direct comparison between the two impossible; still, by looking at most similar bins from their latest materials on the subject it is possible to observe at least qualitative agreement between them.

5.1.3 Trigger and Associate Particle Charge Dependence

One of the properties of particles in a jet is that since they originate from fragmentation of a single parton, they must observe local charge conservation. Of course the same can be said about particles from resonance decays so seeing such conservation does not guarantee that what is observed is really jets — it can however be shown that they are *not* present by observing charge not to be locally-conserved.

In case of two-particle azimuthal correlations local charge conservation, or lack thereof, can be investigated by observing the amplitude of the near-side peak while imposing restrictions on the charge of trigger and associate particles. Figure 5.6 shows correlation functions obtained from like-sign pairs compared to those from unlike-sign ones, as well as charge-unrestricted functions shown earlier to serve as reference.

The figure shows clear enhancement of the near-side peak for unlike-sign pairs comparing to the one for like-sign pairs, in both most central and more peripheral events; see Figure 5.7 for a fit-based quantitative illustration based on linear-fit values from Table 5.2. This effect is consistent with expectations regarding local charge conservation.

5.1.4 Transverse-momentum Dependence of Central *Pb+Pb* Collisions at 158*A* GeV

Another test which can help one tell apart medium interactions from other effects as a source of two-particle azimuthal correlation is dependence of away-side shape on transverse momentum of

[1] Comparison of RHIC and SPS results will be presented later.

	Near-side fit		
Pairs	slope	intercept	χ^2 / NDF
unlike-sign	-0.024 $\pm$ 0.007	1.008 $\pm$ 0.003	0.006 / 1
all	-0.011 $\pm$ 0.004	1.0000 $\pm$ 0.0018	3.98 / 1
like-sign	-0.006 $\pm$ 0.005	0.9962 $\pm$ 0.0022	5.67 / 1

Table 5.2: Peak-fit results for correlation functions from central *Pb+Pb* collisions at 158A GeV presented in Figure 5.6.

associate particles. Quoting Fuqiang Wang from STAR Collaboration, one of the major experts in the field of high-p_T azimuthal correlations [103]:

> A stringent test of statistical momentum conservation is the pt_assoc dependence. Stat. mom. conservation has identical shape cos(dphi), independent of pt_assoc. At RHIC we see dramatic evolution in the away-side shape as function of pt_assoc.

For completeness, in our case we have examined the function's dependence on both p_T^{asc} and p_T^{trg}. Please note that although in some parts of the scan the two bins overlap, we still only investigate triggered correlations; this means that in order for an associate particle to be paired with a trigger particle from the same event, its transverse momentum **must** be lower than that of the trigger. The data on which the scan has been performed has again been the 0–5 % centrality bin of *Pb+Pb* events at 158A GeV. The result can be found in Figure 5.8.

It can be observed that for the available range of trigger and associate transverse momentum, the correlation function undergoes no qualitative changes of shape. One can also note how correlations become very weak as both trigger and associate particles are chosen from lower and lower p_T ranges. The reason behind this is that in such cases our correlation functions become more and more similar to those from non-triggered correlations, sensitive only to anisotropic flow — which is virtually absent in central collisions.

5.1.5 System-size Dependence at 158A GeV

Figure 5.9 shows how the correlation function from central heavy-ion (*Pb+Pb*) collisions at 158A GeV compares to those from central light-ion and nucleon-nucleon events at the same energy, namely — from the 0–5 % centrality bin of the *Si+Si* data set *00X-dedx* and the *p+p* set *00R*. The two functions are shown on two separate plots, with *Pb+Pb* results overlaid on each of them.

As the figure illustrates, overall correlation strength becomes significantly larger as the system size decreases; this is shown quantitatively, basing on linear-fit values from Table 5.3, in Figure 5.10. Moreover, no flattening of the away side visible in central heavy-ion events appears to be present in *Si+Si* and *p+p* collisions — indeed, with the minimum more-or-less in the same place for all systems the away-side peak becomes narrower with decreasing system size.

	Away-side fit		
System	slope	intercept	χ^2 / NDF
Pb+Pb	0.0019 ± 0.0021	1.000 ± 0.006	1.03 / 3
Si+Si	0.07 ± 0.06	0.91 ± 0.15	5.94 / 3
p+p	2.0 ± 0.8	-3.0 ± 2.1	1.15 / 3

Table 5.3: Peak-fit results for correlation functions from collisions at 158A GeV presented in Figure 5.9.

5.1.6 Energy Dependence in Central *Pb+Pb* Collisions

Examining energy dependence of the correlation function in most central (0–5 %) heavy-ion collisions provides one with useful information about the mechanism behind the flattening of the away-side peak at the top SPS energy and beyond. Figure 5.11 compares the function at 158A GeV ($\sqrt{s_{NN}}$ = 17.3 GeV) with those at 80A, 40A, 30A and 20A GeV ($\sqrt{s_{NN}}$ = 12.3, 8.8, 7.6 and 6.3 GeV, respectively). A comparison is also made with PHENIX results from *Au+Au* collisions at the top RHIC energy, $\sqrt{s_{NN}}$ = 200 GeV [93]; note that these are not the latest results on the subject published by a RHIC experiment, they are however the only ones in which exactly the same centrality and p_T bins have been used as at the SPS and their precision is already better than of our results.

As the figure shows, both the shape and amplitude of the function's away side appear to remain mostly unchanged throughout the scan. A quantitative illustration of these effects as a function of energy has been provided, basing on linear-fit values from Table 5.4, in Figure 5.12. It is also interesting to note that while RHIC results from higher p_T bins, as shown in Section 5.1.2, clearly show double-humped away-side structure which has been hailed a signature of strongly-interacting QGP, in this bin the away side is almost flat. On the other hand, amplitude of the near-side peak clearly decreases with decreasing collision energy, up to the point where around 30–40A GeV the it flattens out and then turns into a depletion.

We are waiting with excitement for the first heavy-ion results from the LHC to see how the near- and away-side peak behave at beyond-RHIC collision energies.

5.2 Two-particle ($\Delta\eta$, $\Delta\phi$) Correlations

In case of this part of the analysis our primary purpose has been to attempt observation of the ridge phenomenon and its evolution. Under perfect circumstances one would achieve this by performing a collision-energy and system-size scan similar to what we have done for azimuthal correlations, then again limited size of most NA49 data sets makes this this approach infeasible in practice. It was, however, possible to perform a transverse-momentum scan of central *Pb+Pb* collisions at 158A GeV, similar to the one from Section 5.1.4. Results of such a p_T scan can be found in Figure 5.13.

Energy	Near-side fit		
[GeV]	slope	intercept	χ^2 / NDF
158A	-0.011 $\pm$ 0.004	1.0000 $\pm$ 0.0018	3.98 / 1
80A	-0.005 $\pm$ 0.008	0.997 $\pm$ 0.003	0.74 / 1
40A	0.004 $\pm$ 0.007	0.9914 $\pm$ 0.0027	4.93 / 1
30A	0.011 $\pm$ 0.008	0.984 $\pm$ 0.003	0.0007 / 1
20A	0.037 $\pm$ 0.008	0.975 $\pm$ 0.003	0.89 / 1
$\sqrt{s_{NN}}$ = 200	-0.033 $\pm$ 0.005	1.0201 $\pm$ 0.0021	0.20 / 2
Energy	Away-side fit		
[GeV]	slope	intercept	χ^2 / NDF
158A	0.0019 $\pm$ 0.0021	1.000 $\pm$ 0.006	1.03 / 3
80A	0.003 $\pm$ 0.004	1.000 $\pm$ 0.011	3.27 / 3
40A	0.003 $\pm$ 0.004	1.001 $\pm$ 0.009	1.26 / 3
30A	0.001 $\pm$ 0.004	1.006 $\pm$ 0.011	3.77 / 3
20A	0.001 $\pm$ 0.005	1.005 $\pm$ 0.012	1.74 / 3
$\sqrt{s_{NN}}$ = 200	0.0012 $\pm$ 0.0022	0.994 $\pm$ 0.006	1.35 / 5

Table 5.4: Peak-fit results for correlation functions from central *Pb+Pb* collisions presented in Figure 5.11.

Despite having folded the distributions in both $\Delta\phi$ and $\Delta\eta$ the range in which one could vary p_T^{trg} and p_T^{asc} without introducing unacceptably large statistical uncertainties is quite limited. The next three figures attempt to facilitate interpretation of results as they are by taking a different look of chosen two-particle ($\Delta\eta$, $\Delta\phi$) correlation functions from the p_T scan. In Figure 5.14, three of such functions have been re-plotted as three-dimensional surfaces and in automatic, non-common scales to emphasise their details. On the other hand, Figure 5.15 presents how $\Delta\phi$ projections of low- and high-$\Delta\eta$ regions of the correlation function behave with changing transverse momentum.

As shown in all the figures presented in this section, the near-side region of our ($\Delta\eta$, $\Delta\phi$) functions features no structures uniform in $\Delta\eta$ in any of the examined transverse-momentum bins.

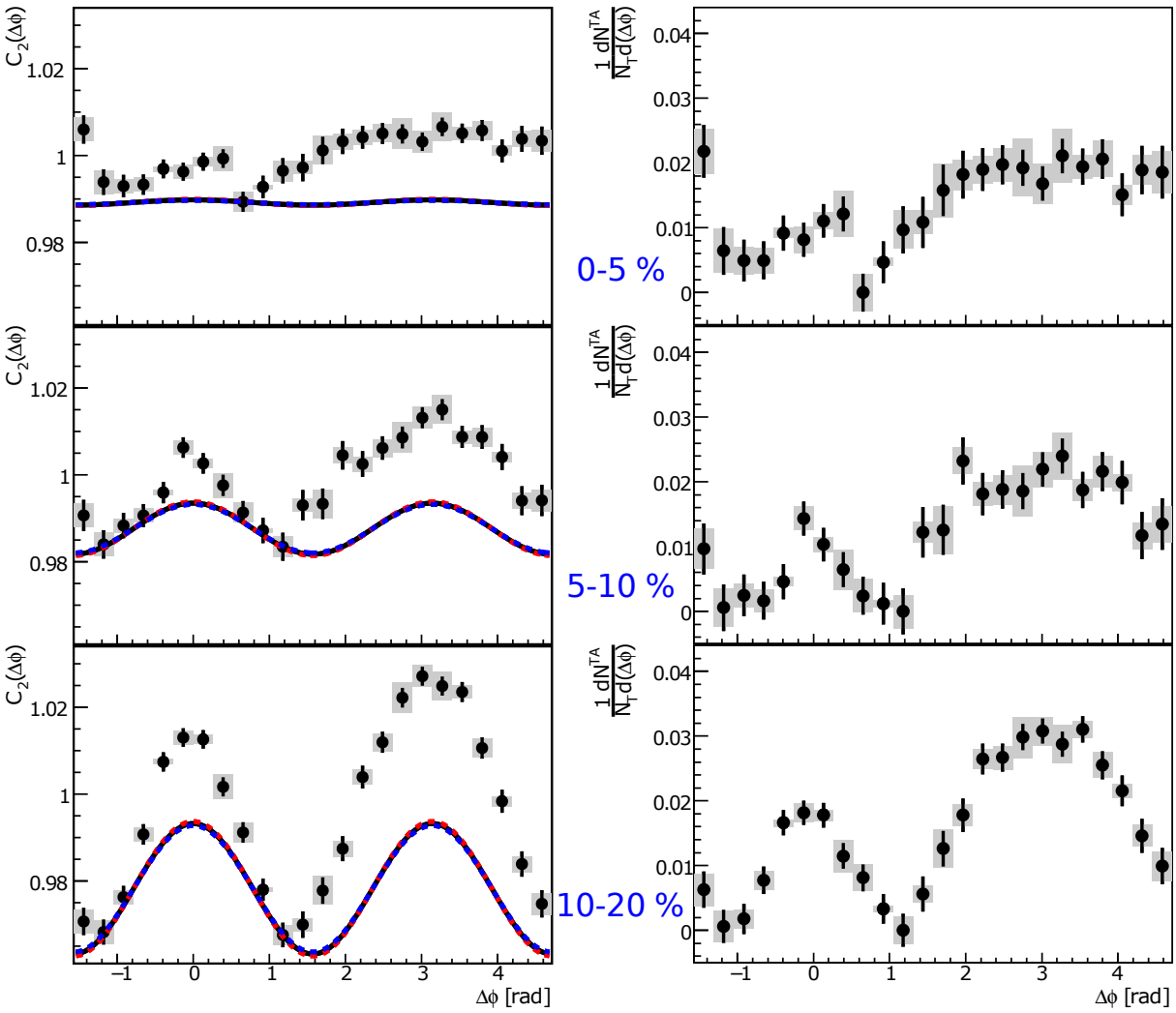

Figure 5.2: **Left**: Two-particle azimuthal correlation functions (with both statistical and systematic errors) of charged hadrons in *Pb+Pb* collisions at 158*A* GeV, for centrality bins 0–5 % (top), 5–10 % (middle) and 10–20 % (bottom). Solid black lines illustrate ZYAM-normalised flow contribution to the function, with the dashed coloured lines indicating modulation due to statistical uncertainties on flow coefficients. **Right**: Per-trigger conditional yield of associate particles obtained by normalising the flow-subtracted correlation function, again in three centrality bins.

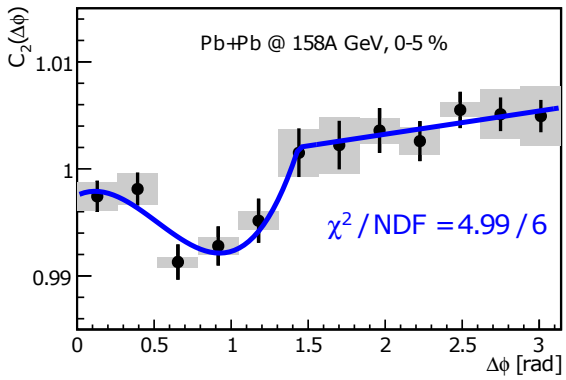

Figure 5.3: Two-particle azimuthal correlation function from 0–5 % *Pb+Pb* collisions at 158A GeV, folded into $[0, \pi]$. The blue line indicates a function fit to the data which will be used later.

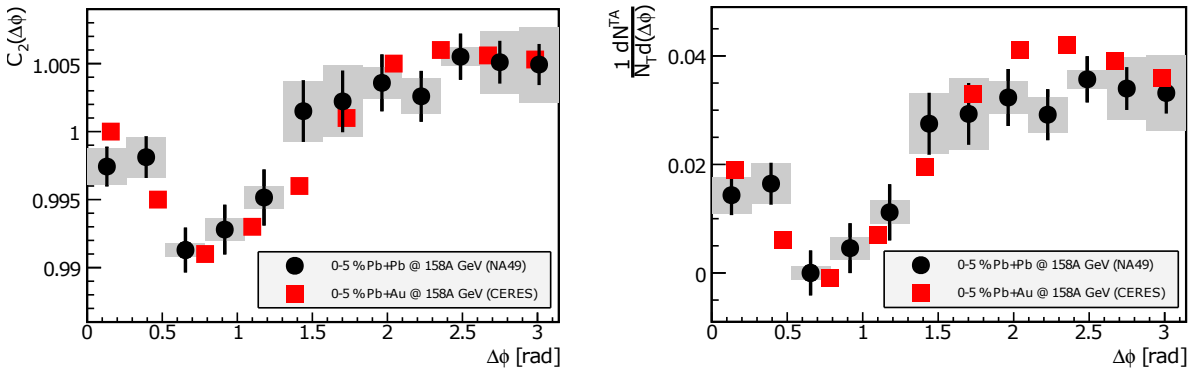

Figure 5.4: Two-particle azimuthal correlation functions (left) and per-trigger conditional yield (right) from different SPS experiments for most central (0–5 %) heavy-ion collisions at the top SPS energy. Black circles: *Pb+Pb* at 158A GeV (NA49, with statistical errors as lines and systematic ones as boxes. Red squares: *Pb+Au* at at 158A GeV (CERES, preliminary), with statistical errors only [100].

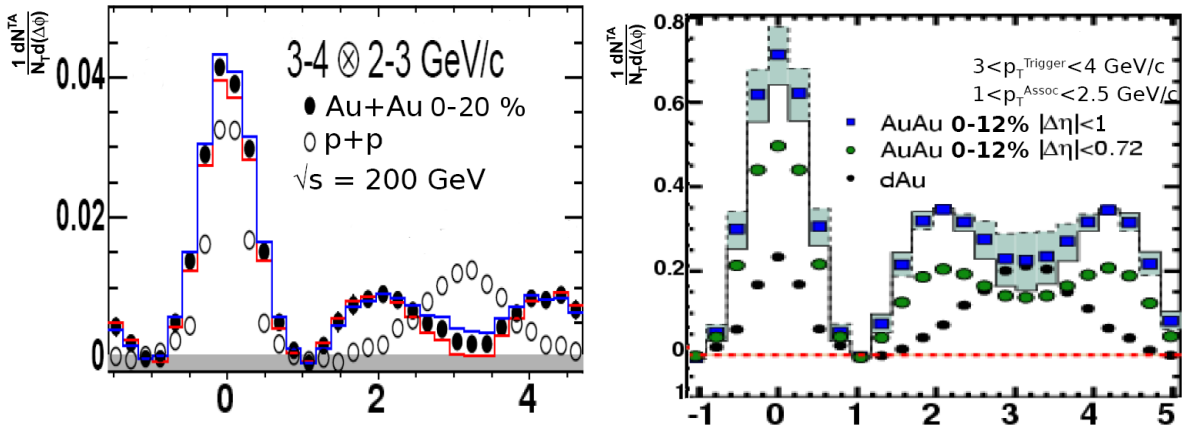

Figure 5.5: Pet-trigger conditional yield in central *Au+Au* collisions at $\sqrt{s_{NN}}$ = 200 GeV measured by two large RHIC experiments. **Left**: Results from PHENIX: centrality 0–20 %, $3 < p_T^{trg} < 4$ GeV/c, $2 < p_T^{asc} < 3$ GeV/c [79]. **Right**: Results from STAR: centrality 0–12 %, $3 < p_T^{trg} < 4$ GeV/c, $1 < p_T^{asc} < 2.5$ GeV/c [102]. Reference from *p+p* (PHENIX) and *d+Au* (STAR) events at the same energy has also been provided.

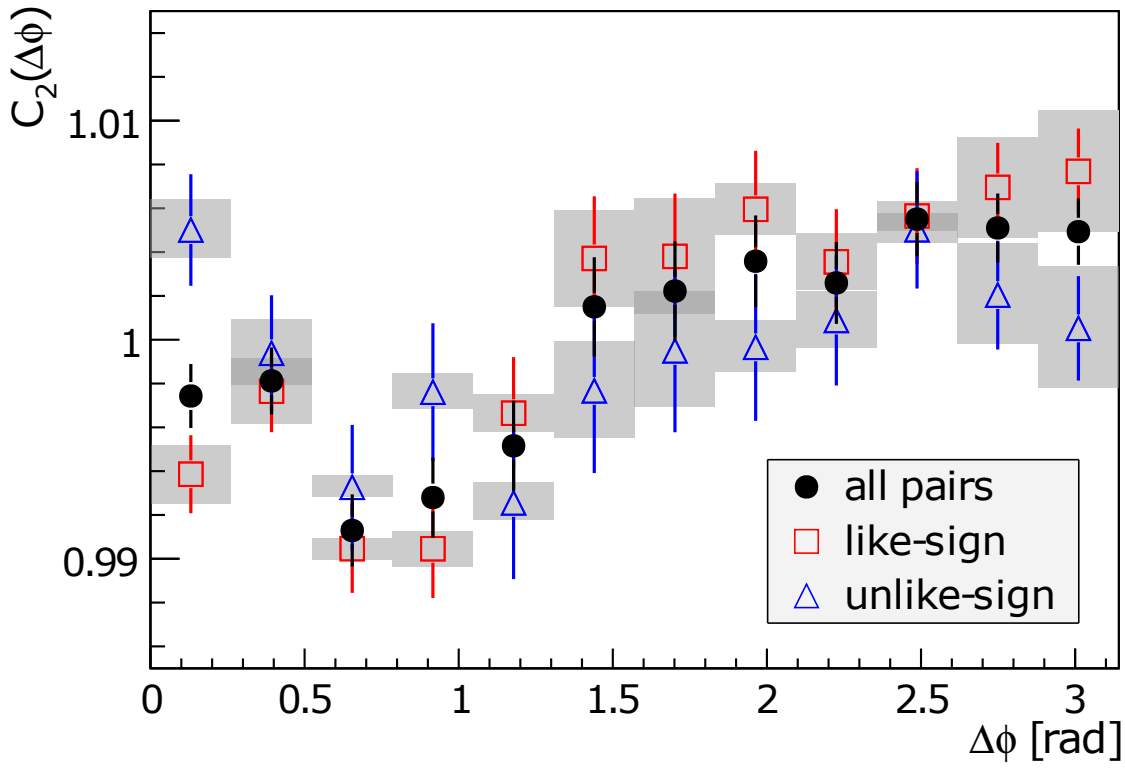

Figure 5.6: Two-particle azimuthal correlation functions from central (0–5 %) *Pb+Pb* collisions at 158*A* GeV, for different combinations of electric charge of trigger and associate particles: like-sign pairs (open red squares), unlike-sign pairs (open blue triangles) and no constraints (black full circles). In order to improve clarity of the plot, systematic errors have been omitted for the unconstrained case.

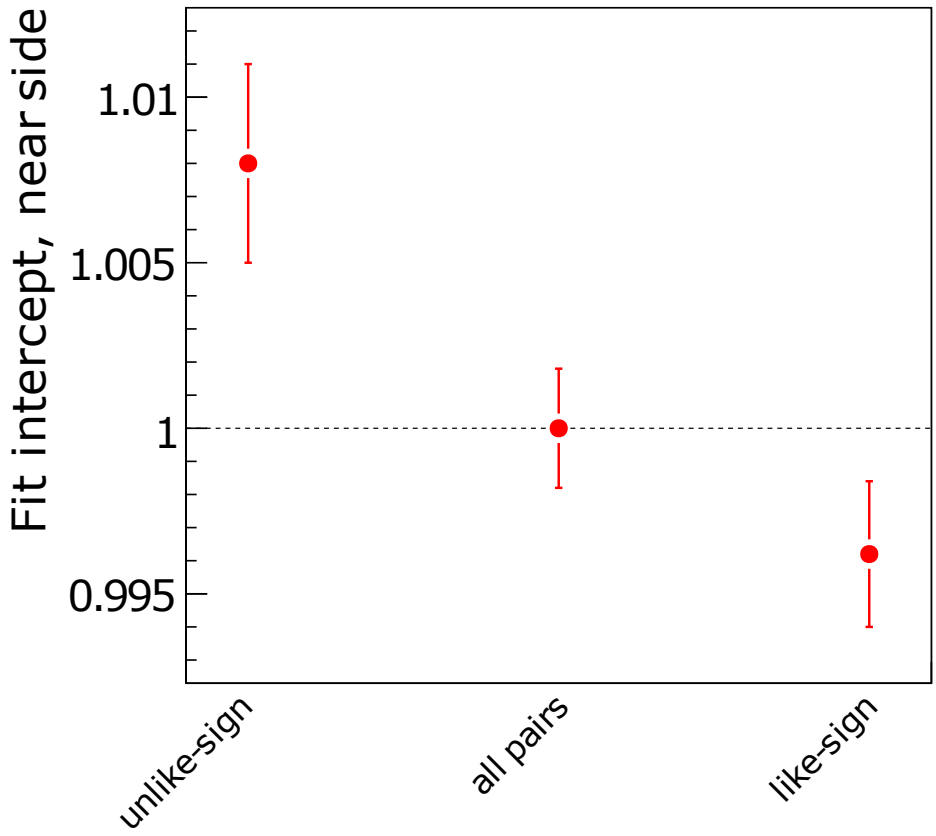

Figure 5.7: Near-side peak amplitude of the two-particle azimuthal correlation function in central *Pb+Pb* collisions at 158A GeV, defined simply as the intercept of a linear fit of the near-side peak and as such equal to $C_2(0)$ obtained from that fit (see Equation 3.5 and Table 5.2), for different combinations of trigger and associate electric charge.

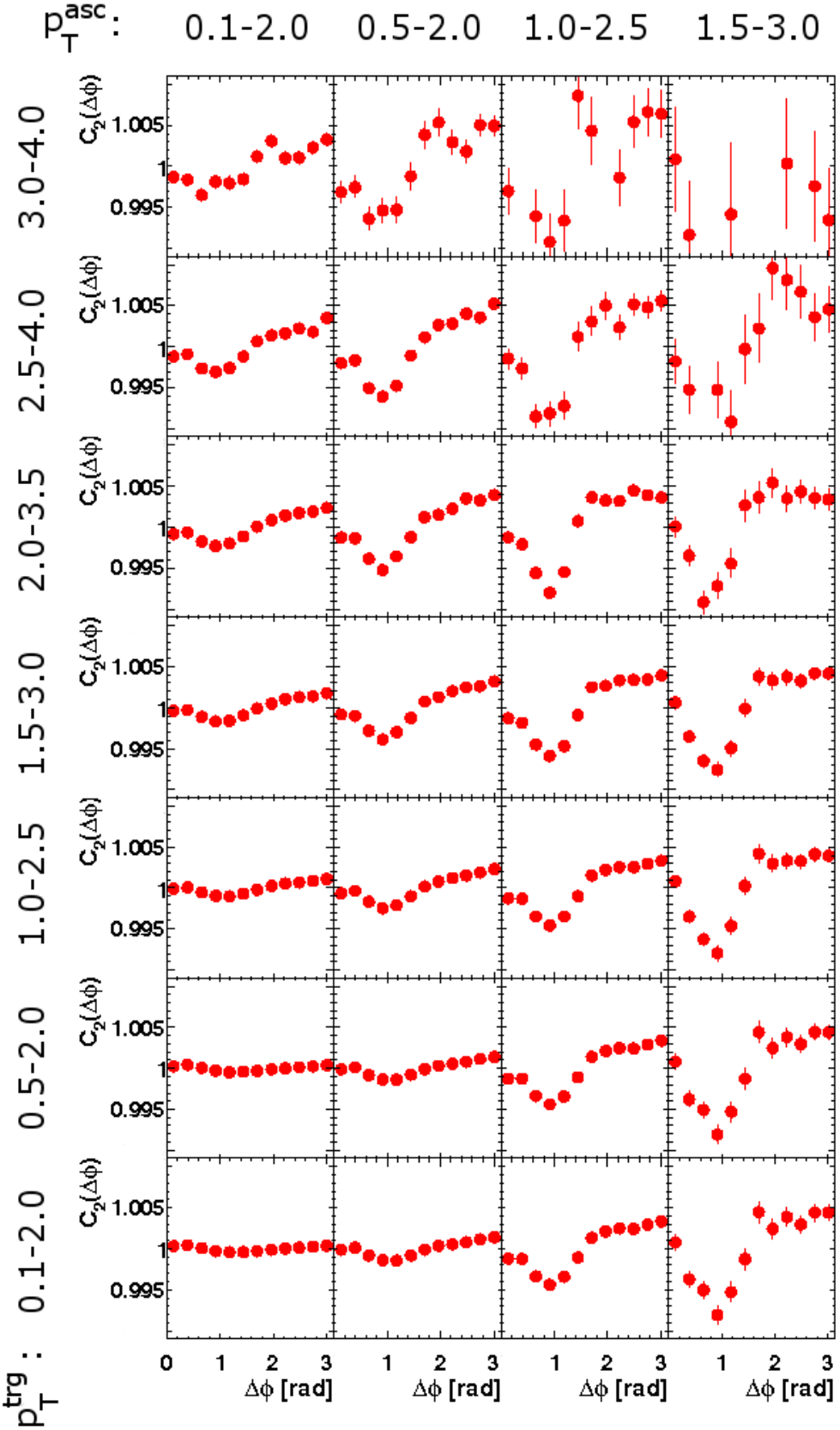

Figure 5.8: Two-particle azimuthal correlation functions obtained for different ranges of associate transverse momentum and fixed trigger p_T, in central (0–5 %) *Pb+Pb* collisions at 158A GeV.

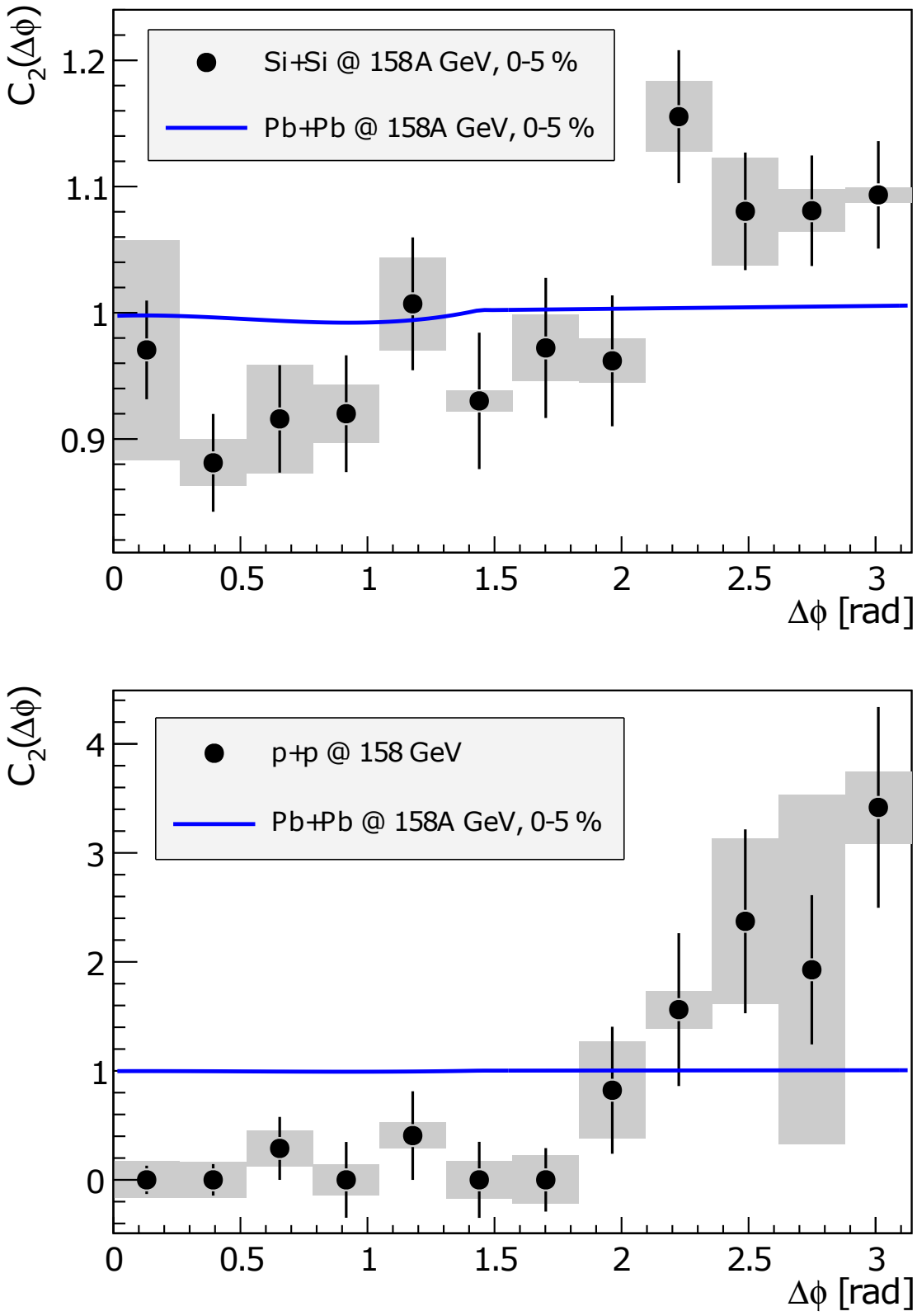

Figure 5.9: Two-particle correlation functions from central *Si*+*Si* (top) and *p*+*p* (bottom) events at 158*A* GeV, compared to central-*Pb*+*Pb* results at the same energy.

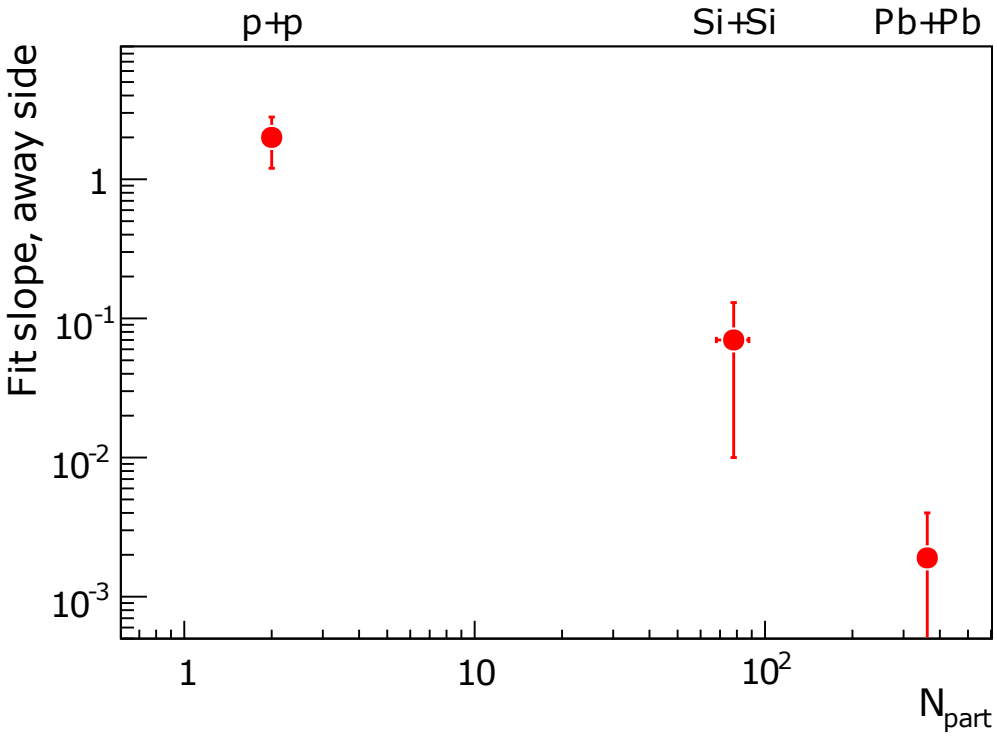

Figure 5.10: Away-side peak amplitude of the two-particle azimuthal correlation function in *p*+*p*, 0–5 % *Si*+*Si* and 0–5 % *Pb*+*Pb* collisions at 158A GeV, defined as the slope of a linear fit of the peak (see Equation 3.5 and Table 5.3), as a function of system size expressed as N_{part}.

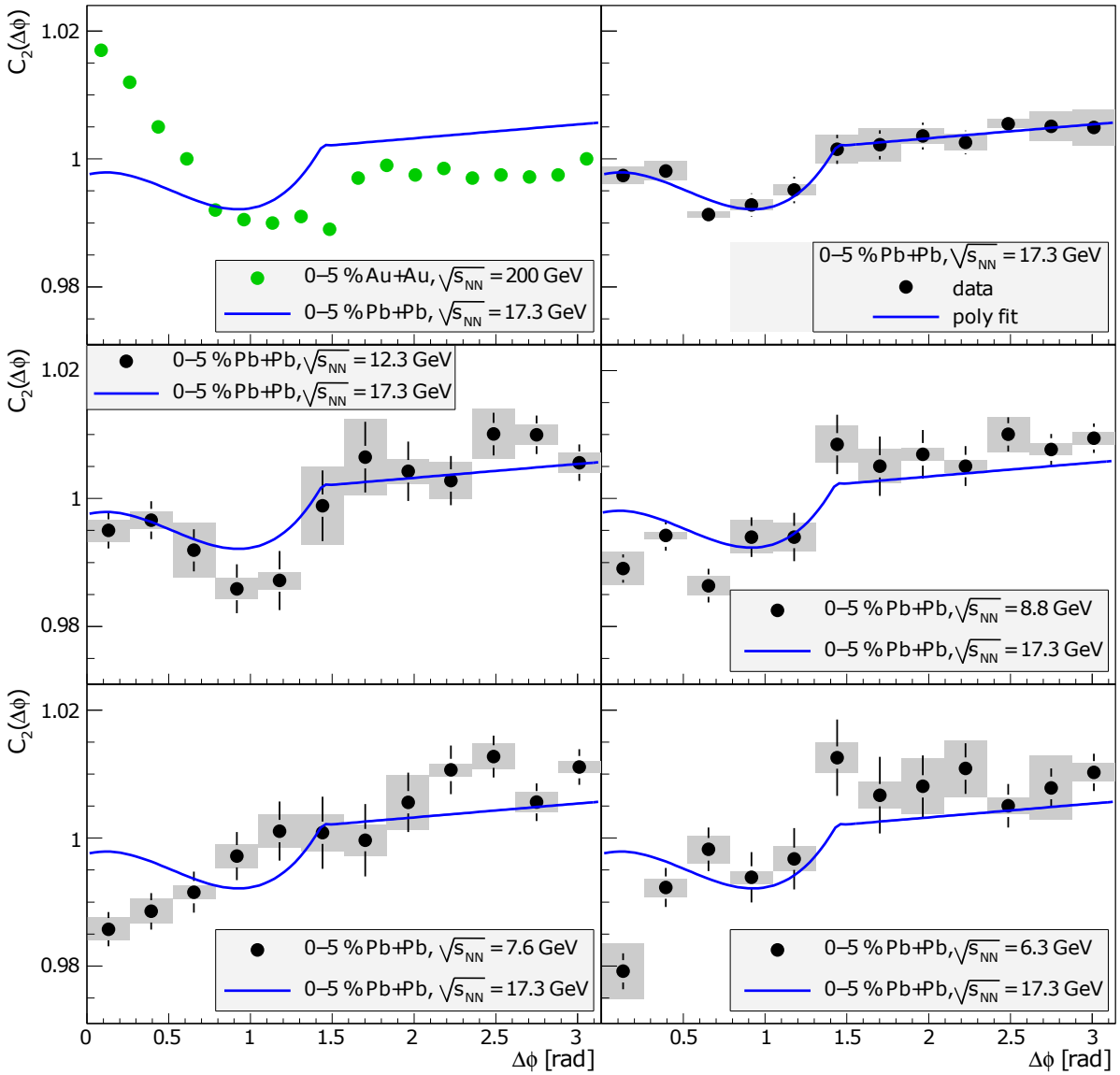

Figure 5.11: Two-particle correlation functions from central (0–5 %) heavy-ion collisions at the SPS (*Pb+Pb* events at 158A, 80A, 40A, 30A and 20AGeV) and RHIC (*Au+Au* events at $\sqrt{s_{NN}}$ = 200 GeV [93]). All function plots have been overlaid with a function fit of *Pb+Pb* at 158A GeV data.

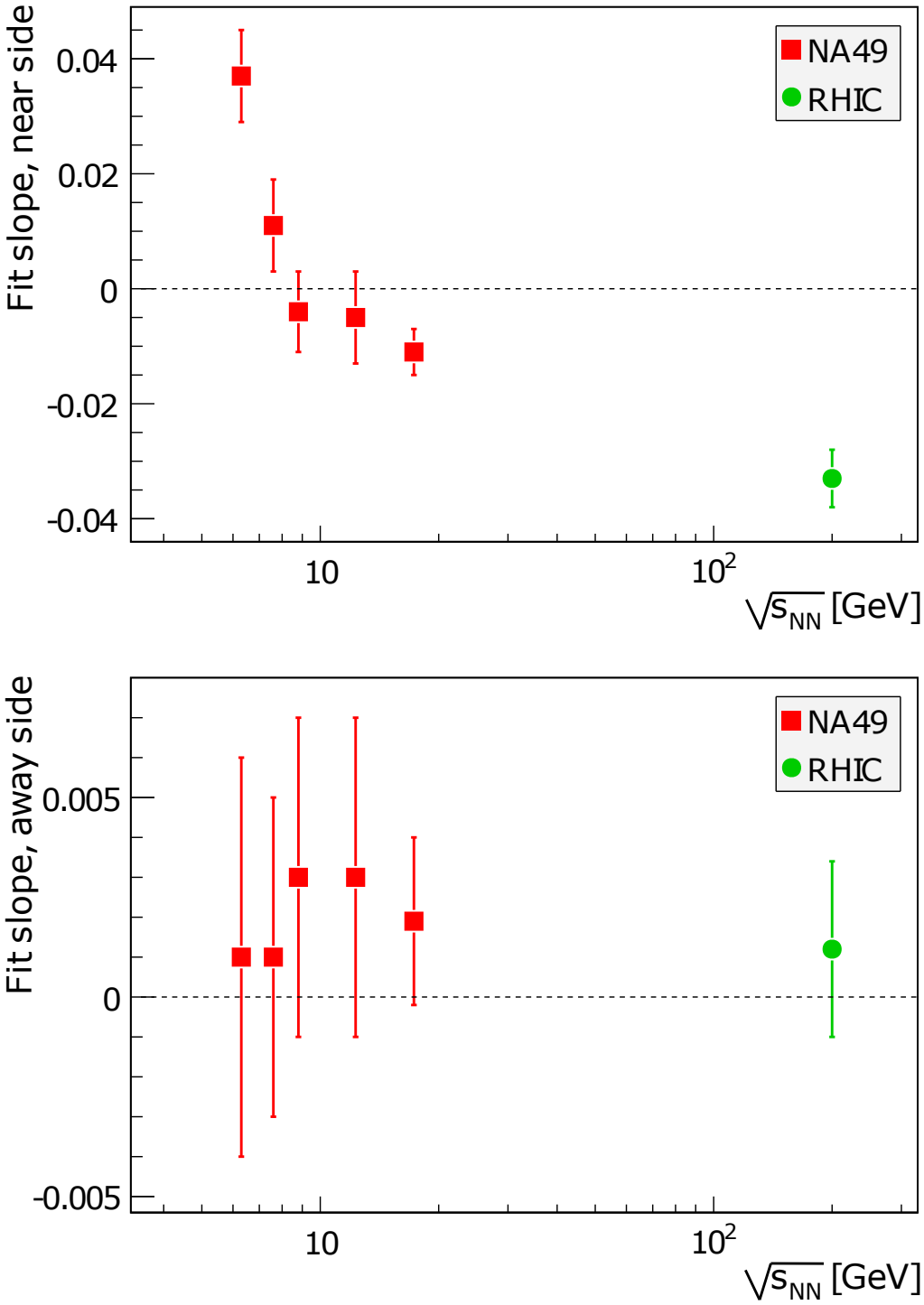

Figure 5.12: Amplitude of near- (top) and away-side (bottom) peak of the two-particle azimuthal correlation function in central (0–5 %) heavy-ion collisions, defined for each peak as the slope of that peak's linear fit (see Equation 3.5 and Table 5.4), as a function of collision energy. RHIC data from [93].

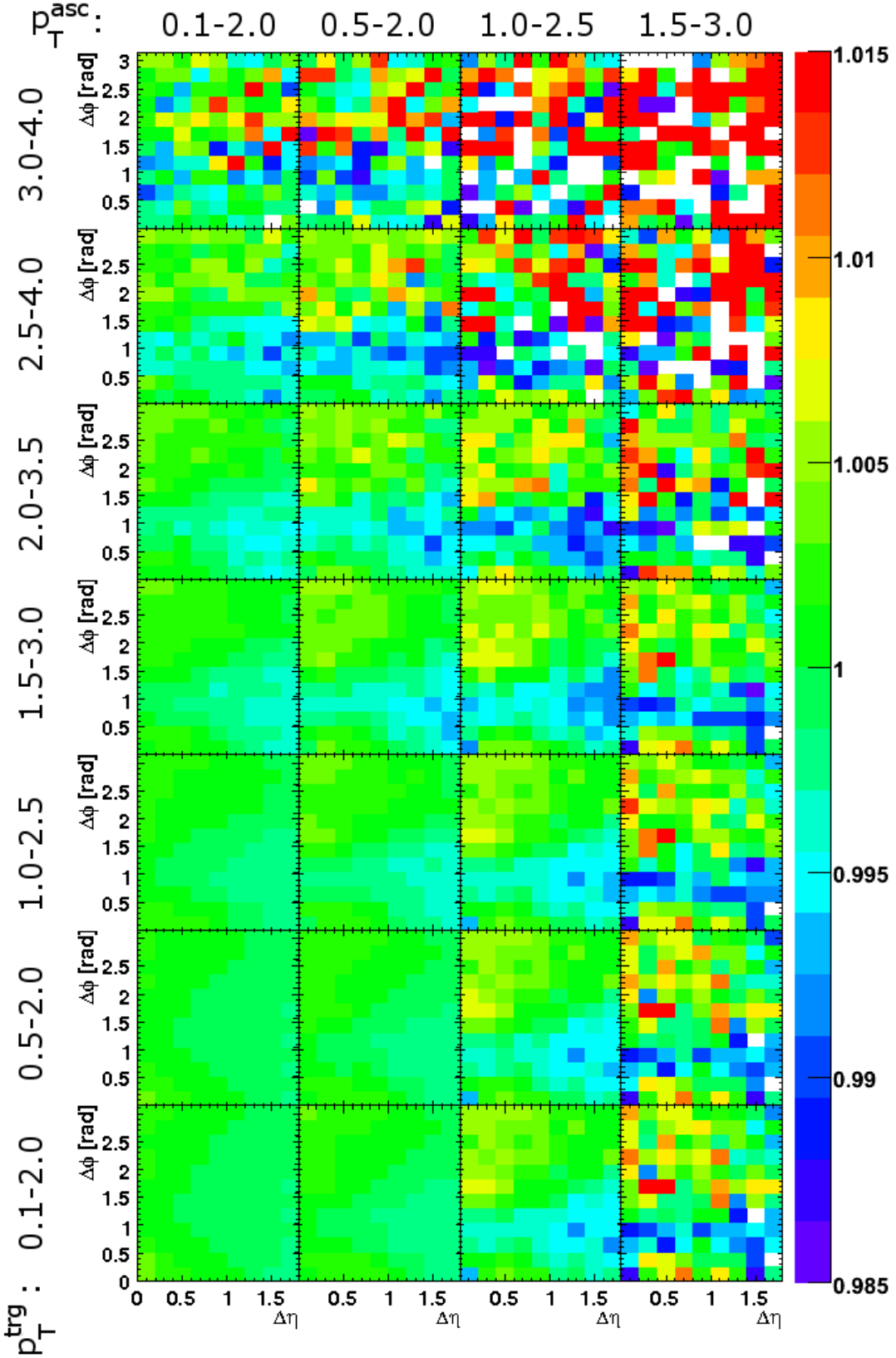

Figure 5.13: Two-particle ($\Delta\eta$, $\Delta\phi$) correlation functions from central (0–5 %) *Pb+Pb* collisions at 158A GeV, produced for different bins of trigger and associate p_T. Errors (statistical only) can be deduced from fluctuations of the signal.

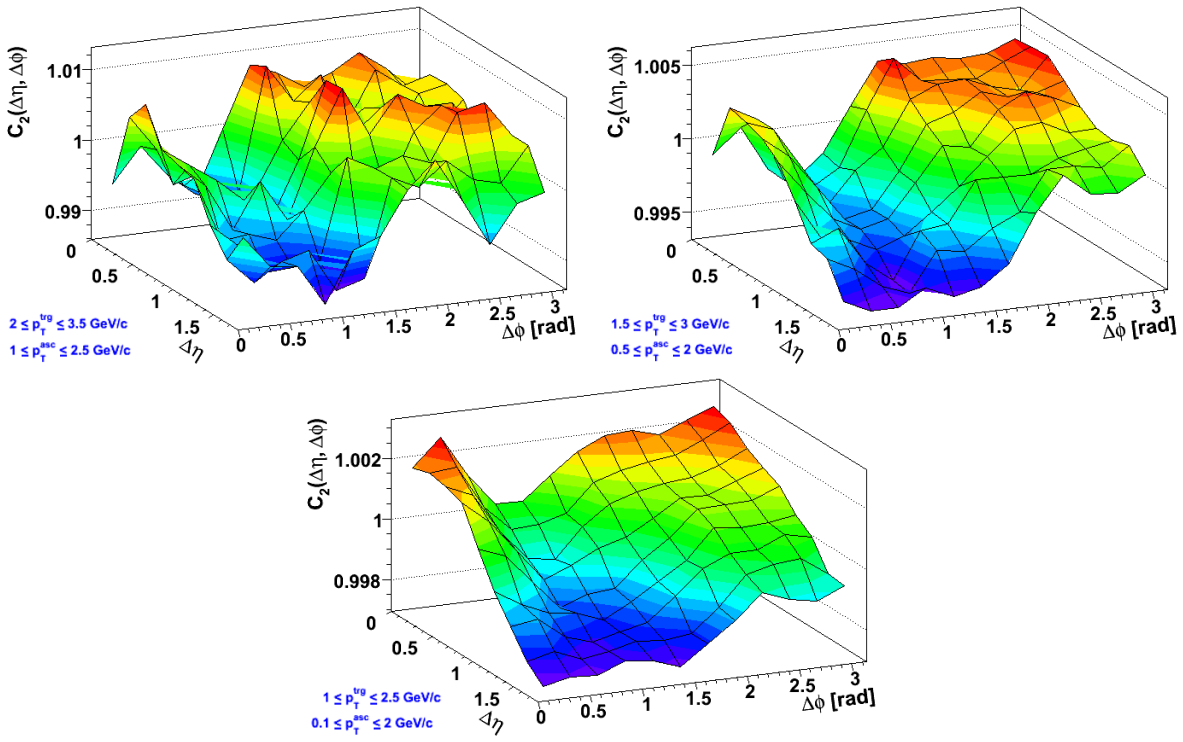

Figure 5.14: Chosen two-particle ($\Delta\eta$, $\Delta\phi$) correlation functions from 0–5 % *Pb+Pb* collisions at 158A GeV presented as surface plots, each in its own, automatic axis range. **Top left**: $2.0\ GeV/c \leq p_T^{trg} \leq 3.5\ GeV/c$, $1.0\ GeV/c \leq p_T^{asc} \leq 2.5\ GeV/c$; **Top right**: $1.5\ GeV/c \leq p_T^{trg} \leq 3.0\ GeV/c$, $0.5\ GeV/c \leq p_T^{asc} \leq 2.0\ GeV/c$; **Bottom**: $1.0\ GeV/c \leq p_T^{trg} \leq 2.5\ GeV/c$, $0.1\ GeV/c \leq p_T^{asc} \leq 2.0\ GeV/c$.

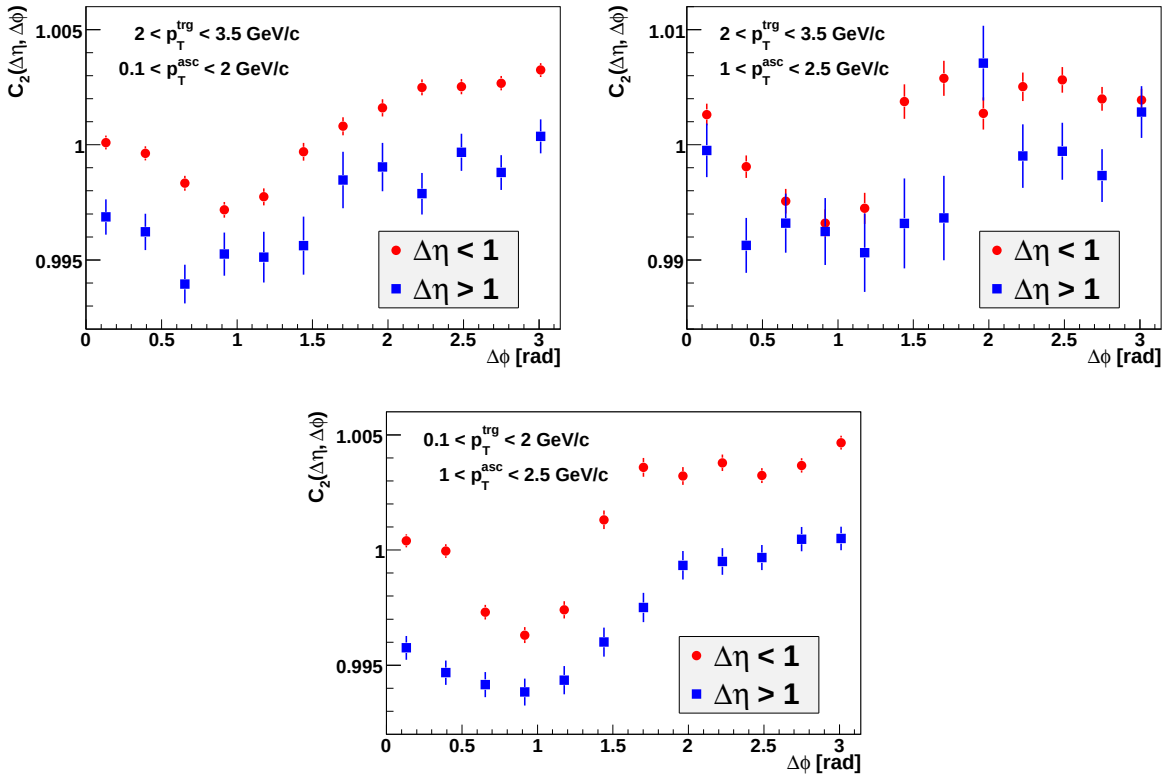

Figure 5.15: $\Delta\phi$ projections of the $\Delta\phi < 1$ and $\Delta\phi > 1$ slices of two-particle ($\Delta\eta$, $\Delta\phi$) correlation functions from 0–5 % *Pb+Pb* collisions at 158A GeV, for different ranges of p_T^{trg} and p_T^{asc} as indicated in the plots. Statistical uncertainties only.

Chapter 6

Interpretation and Comparison with Models

In this chapter, we attempt to interpret the obtained results in the context of original motivation of this project, *i.e.* what long-range — primarily, two-particle azimuthal — correlations can tell us about production of quark-gluon plasma in central heavy-ion collisions, postulated to occur at top SPS energies.

6.1 Two-particle Azimuthal Correlations

6.1.1 Away Side

The earliest results, *i.e.* the centrality scan of *Pb*+*Pb* events at 158A GeV (Figure 5.2), showed the away side of the correlation function to be flattened in most central collisions but Gaussian-like in more peripheral bins, even after flow subtraction; additional corroboration of these results is provided by good agreement with functions produced, under similar conditions but from a much larger event sample, by the CERES Collaboration (see Figure 5.4). Such behaviour could be considered consistent with the scenario of jet modification by the medium, especially given the comparison of correlation functions from different combinations of electric charge of trigger and associate particles (Figure 5.6) did not exclude local charge conservation, which could originate from parton fragmentation, from taking place. Last but not least, no flattening of the away side was observed in *p*+*p* and central *Si*+*Si* collisions at 158A GeV — again, showing this phenomenon to be heavy ion-specific.

Afterwards however, an energy scan of central heavy-ion collisions at the SPS (Figure 5.11) shows the aforementioned flattening of the away side to be persistent throughout the range of available collision energies. Indeed, the shape of the correlation function's away side appears to exhibit *weak or no* energy dependence — even when going to as low energy as 20A GeV! Should this flattening be caused by jet modification in the quark-gluon plasma, these results are at significant odds with present-day expectations that such a state is only produced at higher

energies. Interestingly enough, energy-independent flattening of the away side persists while considering correlation functions produced for the same centrality and transverse-momentum bins by the PHENIX experiment at the RHIC, even though using different p_T bins at the top RHIC energy yields the characteristic double-hump structure which has been hailed a signature of strongly-interacting QGP.

All in all, it appears unlikely that away-side modification of two-particle correlation functions in central *Pb+Pb* collisions at the top SPS energy originates from interactions between jets and quark-gluon plasma produced in such collisions. On the other hand, a number of effects we have observed could be considered consistent with the hypothesis that what we have observed on the away side of the function global is an effect of global momentum conservation:

1. Results from the system-size scan, where the away-side peak becomes higher and more narrow as the number of particles produced in a collision decreases (Figure 5.2) can be qualitatively explained by the fact that the fewer low-p_T associate particles are available, the larger their transverse momentum must be and the less they can spread around the back-to-back axis in order to balance the high-p_T trigger;

2. The aforementioned weak energy dependence of away-side shape in central *Pb+Pb* collisions may be explained by momentum-driven particle distribution "saturating" for large-enough systems and not being affected by relatively small changes in particle multiplicity as a function of collision energy;

3. The shape of the away side in central *Pb+Pb* collision at 158A GeV exhibits very weak sensitivity to selection of associate transverse momentum (Figure 5.8).

A potential problem here could be that results from the two more peripheral bins of our *Pb+Pb* centrality scan do not directly agree with the momentum-conservation hypothesis — functions from these two bins do not possess flattened away side despite having come from events with multiplicity larger than in central events at lower energies, which do yield flattened functions. However, it should be kept in mind that working with more peripheral events requires one to use conditional yield rather than raw correlation functions for comparison due to non-negligible flow contribution to the latter — which makes one susceptible to all the possible issues related to the validity of the two-source model and the ZYAM approach, which were hinted at in Section 3.5 and will be discussed in more detail momentarily. Consequently, at this point we treat results not based directly on raw correlation functions as less reliable.

In order to either further support or debunk the hypothesis of global momentum conservation as a source of two-particle azimuthal correlations at SPS energies, it would be useful to compare produced real-world results to a well-defined reference source. A model needed for this particular comparison should ideally possess the following properties:

- feature well-defined global momentum conservation;

- incorporate mechanisms of jet production, preferably ones that can be turned on and off as needed;
- be known to be agreed with by experimental results in nucleon–nucleon and nucleus–nucleus collisions at SPS energies;
- optionally, allow for simulation of quark-gluon plasma and its interactions with other collision components.

The last point is mostly ongoing work but luckily can often be done without. Moreover, at present no models are established on the market which would allow us to distinguish global and local momentum conservation so it is necessary to stick with one which reliably handles both. That said, models do exist which match our other requirements. A description of the model we have chosen, UrQMD, along with results of the comparison can be found below, in Section 6.3.

6.1.2 Near Side

Even though the study described in this dissertation has been, following mainstream considerations regarding how multiparticle angular correlations can be applied to searching for the quark-gluon plasma (which have been outlined in earlier chapters) along with earlier results from RHIC experiments and CERES, strongly focused on the away side of two-particle correlation functions, certain interesting observations have been made on the near side as well. Possibly the most interesting phenomenon observed here has been how the near-side amplitude of two-particle azimuthal correlation functions drops with decreasing collision energy, in particular the fact it turns into a depletion very close in energy to where other experimental results suggest the onset of deconfinement to take place [104]. While this effect is possibly trivial, should it be shown that it *is* in fact tied to deconfinement it could have far-reaching consequences for the field of correlation studies of heavy-ion collisions. Comparison of experimental and simulated results in Section 6.3 will therefore investigate both the near and the away side of two-particle azimuthal correlation functions.

6.1.3 Critical Overview of the Two-source Model

Despite being very widely used, the two-source model in general and the ZYAM/ZYA1 assumptions are not universally accepted by the heavy-ion physics community. It is held by some researchers in the field, with Miklos Guylassy, one of the fathers of the concept of jet quenching, among them, that even though the model and the assumptions were successfully compared to PYTHIA simulations by their creators, they are in fact too naive to adequately describe real data [105]. In particular, the following reservations have been expressed:

- whether all correlation sources other than jets and flow can really be neglected, in particular when considering trigger particles from the semi-hard p_T range;

- whether uncertainties introduced by the extraction procedure are small enough comparing to the extracted signal itself, in particular when the contribution of hard processes to total particle production is small.

Both of these issues become of utmost importance when studying angular correlations in the SPS energy range, where we are limited to both working with triggers from the semi-hard region and a small contribution of hard processes to total particle production.

Regarding other sources , it has been and still is argued by some researchers that global momentum conservation contributes to correlation functions in a non-negligible way — possibly as much as flow — even at RHIC energies [106]; some experimental results from the RHIC (*e.g.* [107], see Figure 6.1) suggest it may indeed be the case. Additionally, in the SPS energy range there is also the question of contribution of Cronin enhancement; this is not exactly known but basing on extrapolations is expected to be large [108, 109, 110].

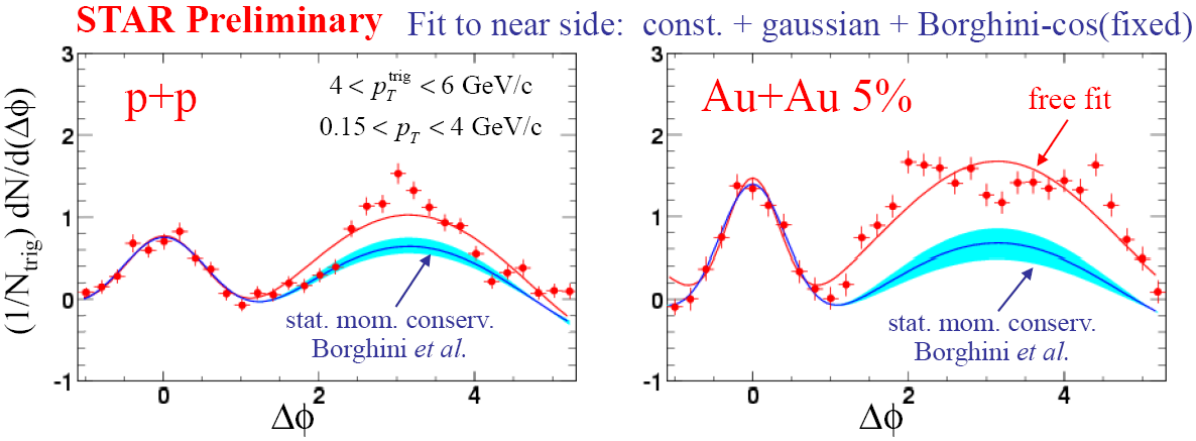

Figure 6.1: Two-particle azimuthal correlation functions obtained by the STAR experiment from *p+p* and central *Au+Au* collisions at 200 GeV/n compared to model predictions of global momentum conservation [107].

As for the matter of precision , this issue can manifest itself in two ways. On one hand, the problem may lie with basic assumptions of the two-source model being too crude, in particular regarding the manner in which a jet is expected to interact with the medium. This is particularly important in case of three-particle correlations — indeed, works have been presented which suggest secondary emission to be much more complex than originally thought (*e.g.* [111, 112]). On the other hand, the method itself may be sound but its sensitivity to external disruptions could be so large that uncertainties they introduce may be of the same order of magnitude as the extracted signal itself [105]. The "prime suspect" here has traditionally been flow: even though all experimental results so far which implied the possibility of the presence of jets in an event actually *modifying* the event's flow were either not conclusive or retracted at a later time, it cannot

be denied that flow measurements possess non-negligible statistical and systematic (resulting *e.g.* from method-dependent degree of contamination of observed values of v_2 and v_4 by non-flow components) uncertainties. How such uncertainties can affect extraction of the jet signal from data can be seen in Figure 6.2; it can be imagined that under appropriate circumstances the method could in fact introduce non-existent structures to one's results, possibly falsifying interpretation of results.

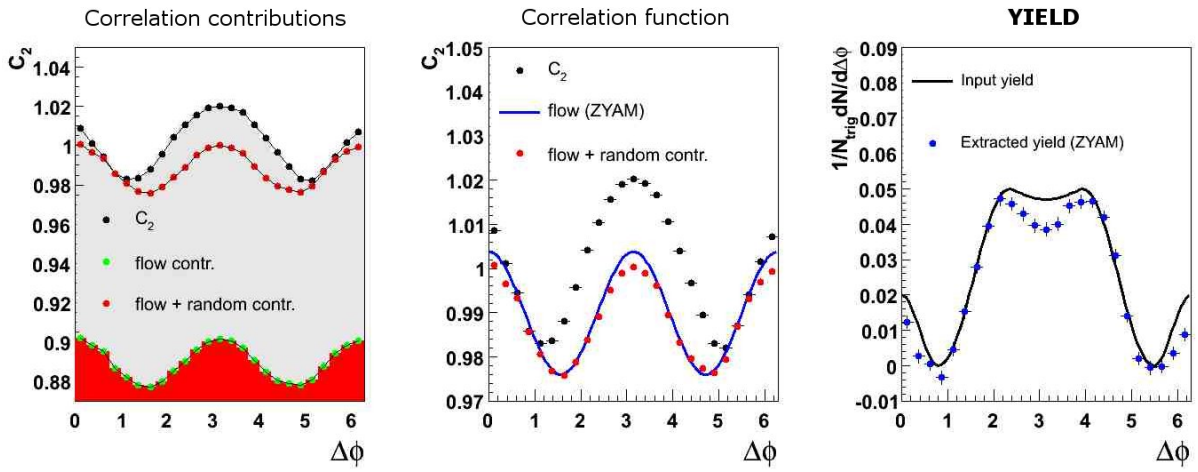

Figure 6.2: A toy-model demonstration of how uncertainties of flow can affect jet-signal extraction from a correlation function. **Left**: different correlation contributions introduced by the toy model: a "dijet", flow and random modulation of flow. **Middle**: A correlation function produced using this model. **Right**: per-trigger conditional yield extracted from this function compared to actual input. It can be observed that even quite small flow uncertainties could lead to noticeably different yield [113].

6.2 Two-particle ($\Delta\eta$, $\Delta\phi$) Correlations

The fact that no ridge-like structure has been observed in any of the trigger- and associate-p_T bins accessible in our study could on its own be interpreted in a number of ways, for instance as a result of trigger bias (correlations at RHIC energies show, as discussed above, a pronounced, multi-particle near-side peak, whereas at the SPS this "peak" is vastly dominated by the high-p_T trigger particle with few or no associates travelling in the same direction; this could have an effect on how quark-gluon plasma interacts with the near-side jet) or simply as being obscured by statistical uncertainty resulting from limited sample size (unlikely, as RHIC results show the ridge signal to be of similar order as that of the away side, but nevertheless possible). However, as even at RHIC energies the ridge phenomenon has not been entirely understood yet, drawing such conclusions would be a mere speculation. On the other hand, the lack of the ridge is also consistent with the momentum-conservation hypothesis formulated basing on our two-particle azimuthal-correlation results: if the away-side plateau is an expression of conservation laws

rather than of jets and their interactions with the medium, one would naturally expect no such interaction-related effects to be present on the near side either.

Another interesting effect observed in two-particle ($\Delta\eta$,$\Delta\phi$) correlations is a dip appearing in some p_T bins near $(0, 0)$[1]. Investigation of this phenomenon has shown it to be about an order of magnitude stronger than two-track resolution effects of the NA49 detector, moreover a similar dip is also visible in CERES results. Since the presence or absence of this effect affects neither the ridge ($\Delta\phi \approx 0$ but large $\Delta\eta$) nor the away side ($\Delta\phi \approx \pi$), discussing it reaches beyond the scope of this dissertation; then again, it does indicate a possible direction for future studies of two-particle angular correlations at the CERN SPS.

6.3 Comparison with the String-hadronic Model UrQMD

The model used for comparison to experimental results obtained in the course of this project is the string-hadronic *Ultra-relativistic Quantum Molecular Dynamics* (UrQMD) by M. Bleicher *et al.*, known to reproduce quite well many processes observed in nucleon–nucleon, nucleon–nucleus and nucleus–nucleus collisions in the energy range of the SPS [114, 115].

UrQMD is a Monte-Carlo implementation of microscopic transport theory, involving covariant propagation of hadrons on classical trajectories along with stochastic binary scatterings, formation and fragmentation of colour strings and decay of resonances. Particularly interesting from the point of view of the analysis descried in this dissertation is version 2.3 of the model, made available in May 2008 — the first release to include, through incorporation of the PYTHIA model [116], production of jets, making it applicable as a source of reference material for this analysis.

Four simulated data sets, two with *p*+*p* and two with *Pb*+*Pb* collisions, of 100,000 events each have been produced for the purpose of the comparison. In each case the beam energy was 158A GeV, the impact parameter was fixed to 0 fm, propagation time was set to 40 fm/c and all other settings were left at their default values. Additionally, two of the samples — one *p*+*p* and one *Pb*+*Pb* run — had jet production switched off by setting *CTOption(44)* set to 0. ASCII output from UrQMD is converted into ROOT files and then fed into the same analysis code as real data.

Figure 6.3 shows the correlation functions obtained from UrQMD data, both with and without jet production enabled, to those from real *p*+*p* and central-*Pb*+*Pb* events. For clarity, error bars have been disabled on simulated functions; they can be deduced from fluctuations of bin values.

As a follow-up we have also produced UrQMD data sets with *Pb*+*Pb* collisions at 20A, 30A, 40A and 80A GeV, then compared them with respective real-data azimuthal correlation

[1]The effect appears also to be present near zero in two-particle azimuthal correlations but as a result of averaging over $\Delta\eta$ is much weaker, to the point where it can be considered negligible comparing to our measurement uncertainties.

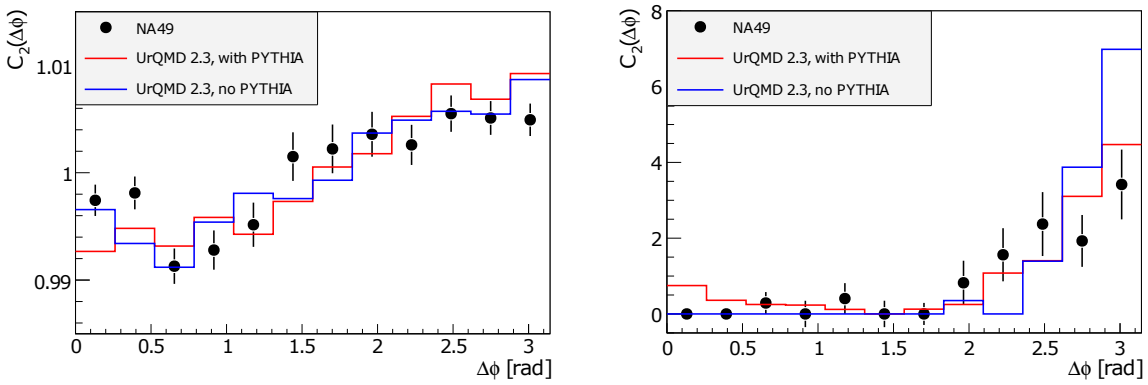

Figure 6.3: Comparison of experimental and simulated two-particle azimuthal correlation functions for central *Pb+Pb* (left) and *p+p* (right) collisions at 158A GeV. Black points: experimental data (statistical errors only); red lines: UrQMD data with jets; blue lines: UrQMD without jets.

functions from Section 5.1.6. Each simulated set contained 100,000 events, produced with the same settings as highest-energy samples and jet production enabled. The comparison can be found in Figure 6.4.

Finally, *Pb+Pb* at 158A GeV events from UrQMD (with PYTHIA) have also been used to produce two-particle ($\Delta\eta$, $\Delta\phi$) correlation functions — or to be exact, we have produced simulated counterparts of the three real-data correlation functions from Figure 5.14. They can be found in Figure 6.5. In order to improve clarity of real-data and UrQMD functions Figure 6.6 contains ratios of the two, presented as $\Delta\eta = 0$ slices so that statistical error bars are visible (systematic ones are of similar order); discrepancies between experiment and simulations, which at least for lower p_T bins, are clearly visible.

As one can see , the agreement between away-sides of two-particle azimuthal correlation function from NA49 data and UrQMD is remarkable even though no systematic uncertainties have been plotted for the former. Note that as the model does not consider the possible presence of quark-gluon plasma in central heavy-ion events, the fact the agreement can be observed for both *p+p* and *Pb+Pb* collisions speaks against interactions of particles with such a medium as a source of flattening of the away-side peak. This hypothesis can be strengthened further by noting that the shape (in *Pb+Pb* events, the amplitude too) of the "peak" remains consistent with the model even after disabling jet production. On the other hand, UrQMD-based results are consistent with the momentum-conservation scenario — which as a side note would suggest the two-source model *not* to be correct, at least for the SPS energy range.

Conversely, UrQMD result do not reproduce the shape of the near side of two-particle azimuthal functions. This is particularly well visible in the energy scan — while for real-data functions the near-side amplitude decreases with decreasing collision energy, for UrQMD functions it stays roughly constant, seeming merely to fluctuate throughout the scan. Furthermore, dis-

abling jet production in UrQMD causes the correlation function to behave differently in *Pb+Pb* collisions than in *p+p* ones at the same energy. This phenomenon needs to be investigated in the future.

Last but not least, agreement between NA49 and UrQMD results observed for two-particle azimuthal correlations does not appear to hold so well in the two-particle ($\Delta\eta$, $\Delta\phi$) case: not only are inconsistencies on the near side more pronounced than for azimuthal functions, certain differences can also be seen as one progresses to the away side. It remains to be seen whether this behaviour can be looked into within sample-size limitations of NA49 data.

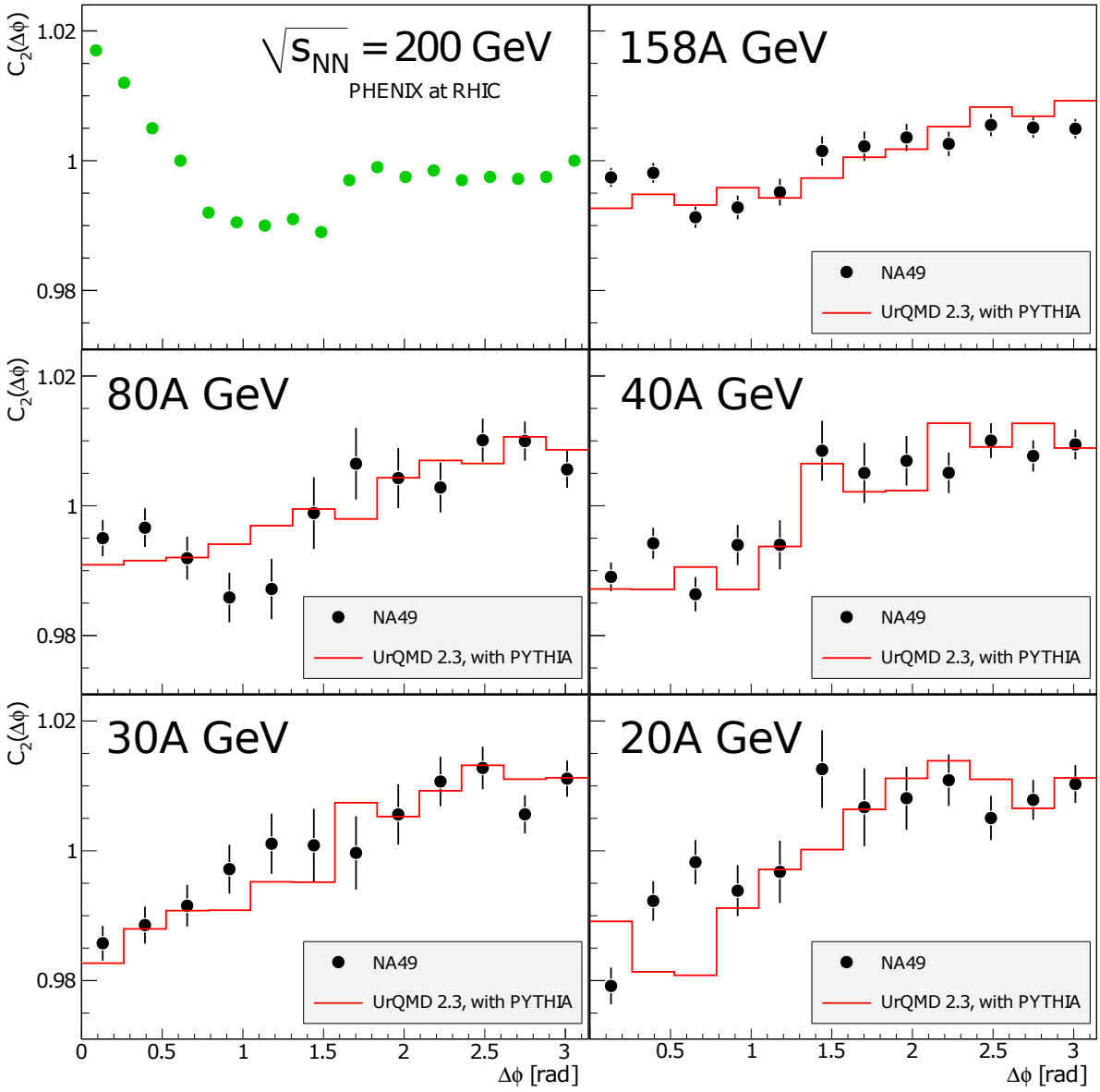

Figure 6.4: Comparison of experimental and simulated two-particle azimuthal correlation functions for central *Pb+Pb* collisions at 158A (top right), 80A (middle left), 40A (middle right), 30A (bottom left) and 20A (bottom right) GeV. Black points: experimental data (statistical errors only); red lines: UrQMD data. An experimental correlation function from central *Au+Au* collisions at $\sqrt{s_{NN}}$ = 200 GeV has been provided for reference [93].

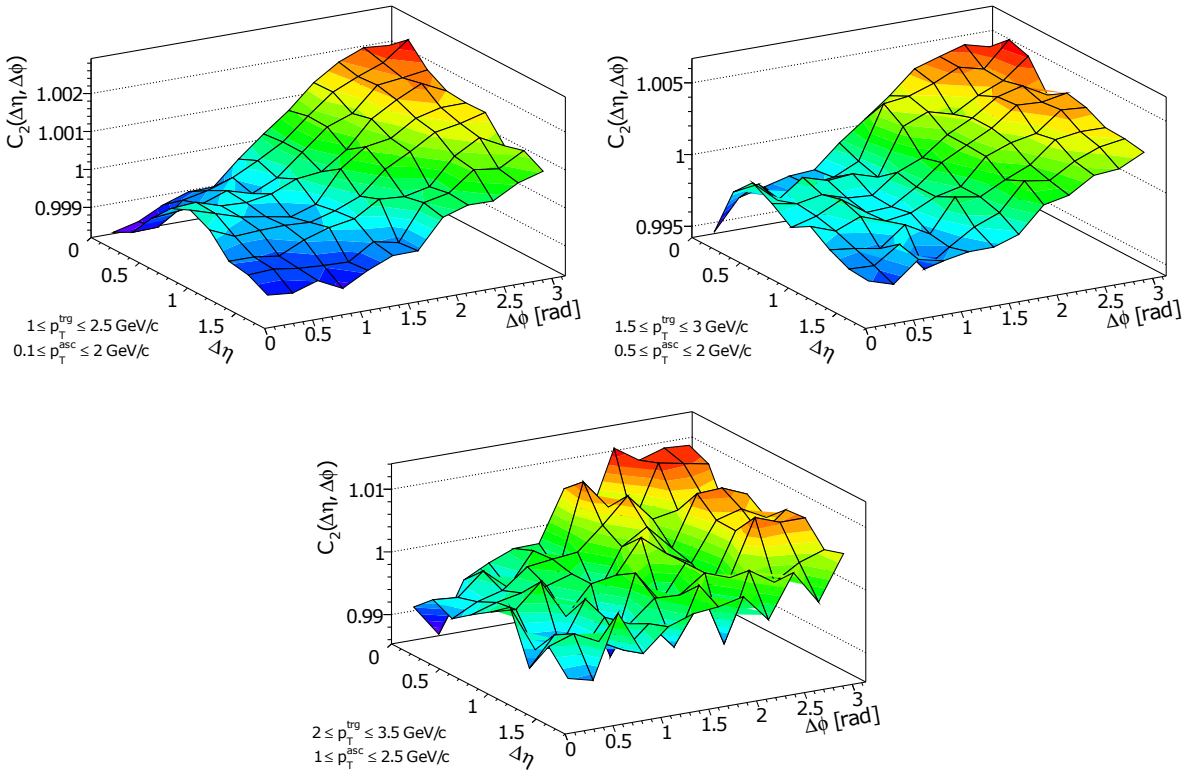

Figure 6.5: Two-particle ($\Delta\eta$, $\Delta\phi$) correlation functions from central *Pb+Pb* collisions at 158A GeV simulated using UrQMD 2.3, for different transverse-momentum bins. **Top left**: $2.0\ GeV/c \leq p_T^{trg} \leq 3.5\ GeV/c$, $1.0\ GeV/c \leq p_T^{asc} \leq 2.5\ GeV/c$; **Top right**: $1.5\ GeV/c \leq p_T^{trg} \leq 3.0\ GeV/c$, $0.5\ GeV/c \leq p_T^{asc} \leq 2.0\ GeV/c$; **Bottom**: $1.0\ GeV/c \leq p_T^{trg} \leq 2.5\ GeV/c$, $0.1\ GeV/c \leq p_T^{asc} \leq 2.0\ GeV/c$.

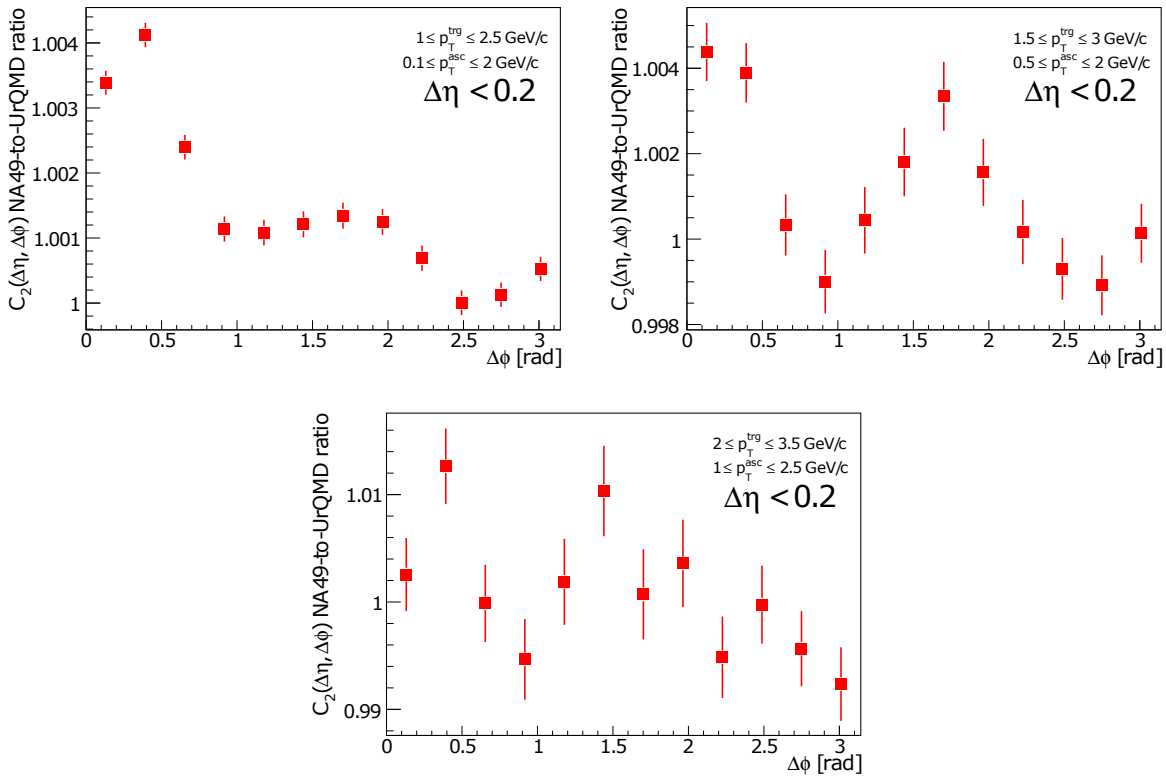

Figure 6.6: Ratios of real-data two-particle $(\Delta\eta, \Delta\phi)$ correlation functions in several transverse-momentum bins, as shown in Figure 5.14, to their respective counterparts from Figure 6.5. Each ratio has been presented as a slice at $\Delta\eta = 0$ so that error bars (statistical uncertainties only) are visible. **Top left**: $2.0\ GeV/c \leq p_T^{trg} \leq 3.5\ GeV/c$, $1.0\ GeV/c \leq p_T^{asc} \leq 2.5\ GeV/c$; **Top right**: $1.5\ GeV/c \leq p_T^{trg} \leq 3.0\ GeV/c$, $0.5\ GeV/c \leq p_T^{asc} \leq 2.0\ GeV/c$; **Bottom**: $1.0\ GeV/c \leq p_T^{trg} \leq 2.5\ GeV/c$, $0.1\ GeV/c \leq p_T^{asc} \leq 2.0\ GeV/c$.

Chapter 7

Summary and Conclusions

In the course of the project described in this dissertation we have studied long-range correlations of charged hadrons at high transverse momentum, in central and mid-central *Pb*+*Pb*, *Si*+*Si* as well as *p*+*p* collisions at beam energies from 20A to 158A GeV, observed by the NA49 experiment at the CERN SPS. This was the first such an analysis performed in NA49 and only the second among all SPS experiments. For the first time, dependence of two-particle azimuthal correlation functions on system size at 158A GeV, as well as on energy of central *Pb*+*Pb* collisions in the SPS range, have been presented.

The project's initial goal was to attempt observing modification of jets by quark-gluon plasma expected to be produced in central, high-energy heavy-ion collisions, thus complementing spectacular results obtained using such techniques by experiments at the BNL RHIC. The means through which this goal was to be achieved was a number of scans — centrality, system size, beam energy and particles' transverse momentum — over available data using two-particle azimuthal, and in the last case two-particle ($\Delta\eta$, $\Delta\phi$), correlation functions. Some of our results were compared to correlation functions produced using data from the string-hadronic model UrQMD.

We have introduced two-particle azimuthal and ($\Delta\eta$, $\Delta\phi$) correlation functions, in both cases using the event-mixing method in order to account for non-uniformities in acceptance of the NA49 detector, as well as a method of accounting for flow in all but most central collisions. Appropriate event and track cuts have been implemented in order to improve signal quality. Statistical and systematic uncertainties associated with the correlation functions have been evaluated. After performing the aforementioned scans, the following has been observed.

Somewhat surprisingly, results of our investigation appear to imply that observed correlations do *not* originate from jets. In particular, the fact the shape and amplitude of the away side of two-particle azimuthal-correlation functions, which is where one expects jet-medium modification effects to become visible, remain almost unchanged over the whole examined energy range of central *Pb*+*Pb* events is at odds with theoretical expectation of quark-gluon plasma being produced only in higher-energy collisions. Moreover, two-particle ($\Delta\eta$, $\Delta\phi$) correlation functions from central *Pb*+*Pb* interactions at 158A GeV show no evidence for the ridge

phenomenon, expected to accompany modification of the away side when the hot medium is produced. RHIC-based expectations regarding the away-side shape dependence on selection of associate transverse momentum are not met, either. Last but not least, UrQMD simulations, which agree well with our data on the away side, produce correlation functions which are similar in shape regardless of whether jet production is enabled or not.

On the other hand, results we have obtained show a large degree of consistency with qualitative expectations of how two-particle azimuthal correlation functions would behave were their source be global momentum conservation. In particular, this approach is supported by the evolution of away-side shape during the system-size scan as well as weak or no dependence of that shape on collision energy or associate transverse momentum. It is also worth noting that UrQMD simulations reproduce real-data away-side results well for both p+p and central Pb+Pb collisions, despite the lack of jet-medium effects in the simulation and indeed even with jet production disabled in the model. This result is consistent with momentum conservation in general. As a side effect of this comparison, should our observation turn out to be accurate it would provide experimental evidence for base assumptions of the two-source model not to be correct in the SPS energy range.

Future Directions

An important next step which could follow this study would be to compare its experimental results with a model which can distinguish between global and local momentum conservation. One such model is presently under development at the Institute of Theoretical Physics of the Goethe University in Frankfurt; once it has been completed, it will like prove extremely helpful in continuing interpretation of results of this study.

Secondly, improved statistical significance of the high-energy p+p and Si+Si two-particle azimuthal correlation functions is also desirable. Although the analysis described in this dissertation has already taken advantage of all the NA49 data from those systems, the NA61/SHINE experiment is to acquire in the upcoming years large samples of p+p, C+C, Si+Si and In+In events in the energy range of 10A to 158A GeV. This will not only allow for the aforementioned improvement but also make it possible to vastly extend energy and system-size scans performed in the current study, especially given NA49 and SHINE feature largely the same hardware and software.

Next, interesting information regarding the origin of the observed behaviour of two-particle azimuthal correlation functions in the away-side domain could be obtained by comparing results on the subject obtained in heavy-ion collisions at the SPS and at the RHIC to ones at even higher energies. This should become possible in the near future thanks to the LHC.

Last but by no means least, a large window of opportunity exists for further attempts of interpreting behaviour of the near-side peak of azimuthal correlation functions as a function of collision energy. In particular, the slope of that peak in central Pb+Pb collisions changes its sign at about 40A GeV: at this point near-side correlation between trigger and associate parti-

cles seen at higher energies change to anti-correlations observed on the lower end of the SPS energy range. What is the origin of this transition? Is it correlated with phenomena observed by NA49 which are considered evidence for the onset of deconfinement at the SPS? This question can be answered by further studies, which would benefit from both experimental results of NA61/SHINE, theoretical considerations and collaboration with model developers.

Appendix A

Basic Terminology

The aim of this section is to summarise kinematic variables and basic terms used throughout the dissertation.

A.1 NA49 Coordinate System

NA49 coordinates are based on a right-handed Cartesian system, with the following properties:

- The origin is located on the beam line, in the centre of the second NA49 magnet;
- Similarly to most other detector set-ups in the field, the z axis corresponds to the beam line. Direction of the beam specifies that of the axis, *i.e.* z is larger downstream;
- The y axis is vertical, pointing up.

A number of other, related variables is often used in addition to the above:

- "Transverse" distance from the beam, $r = \sqrt{x^2 + y^2}$;
- The polar angle, $\theta = \mathrm{atan}\left(\frac{z}{r}\right)$;
- The azimuthal angle, ϕ, between the x axis and r.

A.2 Kinematic Variables

Each particle can be described kinematically by its *momentum* $\vec{p}$ and *energy* E. As the system is relativistic, the latter is related to the particle's *invariant mass* m as (for $c = 1$):

$$E = \sqrt{m^2 + p^2}. \tag{A.1}$$

In particle collisions the momentum vector is typically divided into the parts *longitudinal* (marked $p_{\parallel}$ or p_L) and *transverse* ($p_{\perp}$ or p_T) to the beam. The latter is of particular interest from the point

of view of physics of an event as it originates entirely from the collision (by definition, the beam carries no $p_\perp$), moreover it is quite obviously invariant under Lorentz boosts along the beam axis. In a Cartesian system with the z axis placed along the beam line, $p_\parallel = p_z$ and $p_\perp = \sqrt{p_x^2 + p_y^2}$.

By analogy to transverse momentum one can define *transverse mass* of a particle,

$$m_\perp = \sqrt{m^2 + p_\perp^2}, \tag{A.2}$$

which pertains to energy the particle in question carries in the transverse direction.

Another useful variable, this time pertaining to the longitudinal direction, is *rapidity*, y. Due to the complex way simple longitudinal velocity $v_\parallel$ varies under Lorentz boosts along the beam axis, it isn't of much practical use — especially in fixed-target set-ups, where it is often necessary to transfer between laboratory and centre-of-mass reference frames. If however one defines rapidity as

$$y = \frac{1}{2} \ln \left(\frac{E + p_\parallel}{E - p_\parallel} \right) = \operatorname{atanh} \left(v_\parallel \right), \tag{A.3}$$

it can be shown that it is additive under the boost. Moreover, it is quite simply related to energy and longitudinal momentum of a particle: $E = m_\perp \cosh y$, $p_\parallel = m_\perp \sinh y$. Last but not least, if we define another variable, *pseudorapidity*, as

$$\eta = \frac{1}{2} \ln \left(\frac{p + p_\parallel}{p - p_\parallel} \right) = - \ln \left(\tan \frac{\theta}{2} \right), \tag{A.4}$$

it can be seen from Equation A.1 that for $m \to 0$ and/or $p \to \inf$ rapidity and pseudorapidity are equal — which is useful, as the latter possesses simple geometric meaning and can be derived directly from experimental observables.

A.3 Participants and Spectators

Assuming the binding energy of atomic nuclei to be negligible in a high-energy collision and basing on a classic, geometric view of such collisions, it can be intuitively stated that if two such nuclei do not collide exactly head-on, or if a single nucleon collides with a nucleus, only some of the projectile and/or the target's nucleons will actually take part in the interaction. As it turns out, such a naive statement both holds well enough for more realistic descriptions and corresponds with experimental observations, making the division of nucleons into *participants* and *spectators* useful and well-established in the field.

A nucleon is considered a participant if it undergoes at least one scattering in a collision. Obviously, such information cannot really be acquired experimentally and is therefore typically obtained by matching real-world results to model predictions. Conversely, it is relatively easy to observe spectators — not only do they retain much of their properties, low transverse momentum in particular, from before the collision but also mostly remain bound into large fragments

of original nuclei, frequently called *remnants*. If such remnants possess large longitudinal momentum in laboratory frame, *i.e.* if they are beam remnants, it is possible to detect them with appropriate equipment placed near the beam axis downstream from the interaction point; this is of course easier with collider set-ups.

A.4 Collision Geometry

If one disregards the peculiarities of shape of colliding objects[1], the primary variable describing collision geometry is the distance between them. In theoretical calculations this is normally expressed as the *impact parameter* b, defined as the length of the impact vector $\vec{b}$ — a vector drawn between geometric centres of the projectile and the target in the plane transverse to the beam direction. In conjunction with predictions regarding the radii of the colliding objects one can use this quantity to determine the size and shape of interaction volume.

Impact parameter is not directly useful under experimental conditions because it cannot be measured. Instead, one bases determination of collision geometry on spectator energy or particle multiplicity. In nucleus–nucleus collision this information is then translated into *centrality* (σ/σ_{geom}), which is the percentile of events with at least that low spectator energy multiplicity in a minimum-bias sample for the same system and energy.

Conversion between impact parameter and centrality is possible, using models such as the Glauber approach (as described in Section 1.4.2) or CGC.

Reaction plane In addition to the transverse plane one can also define the *reaction plane* of a collision, as a plane formed by the impact vector and the beam axis. Knowledge of position of this plane, which is random but can be determined experimentally, is particularly useful in the analyses of anisotropic flow.

[1] Which are not a large factor at high energies, even for heavy ions.

Appendix B

Acceptance Plots

Figures presented in this chapter depict various acceptance plots for all the data sets used in this study, as listed in Table 2.1. The plots have been produced from 10,000 events from each data set, after applying all event and track cuts. The following distributions have been generated: rapidity (with pion mass hypothesis) vs. transverse momentum (Figure B.1), transverse momentum (Figure B.2), azimuthal angle (Figure B.3).

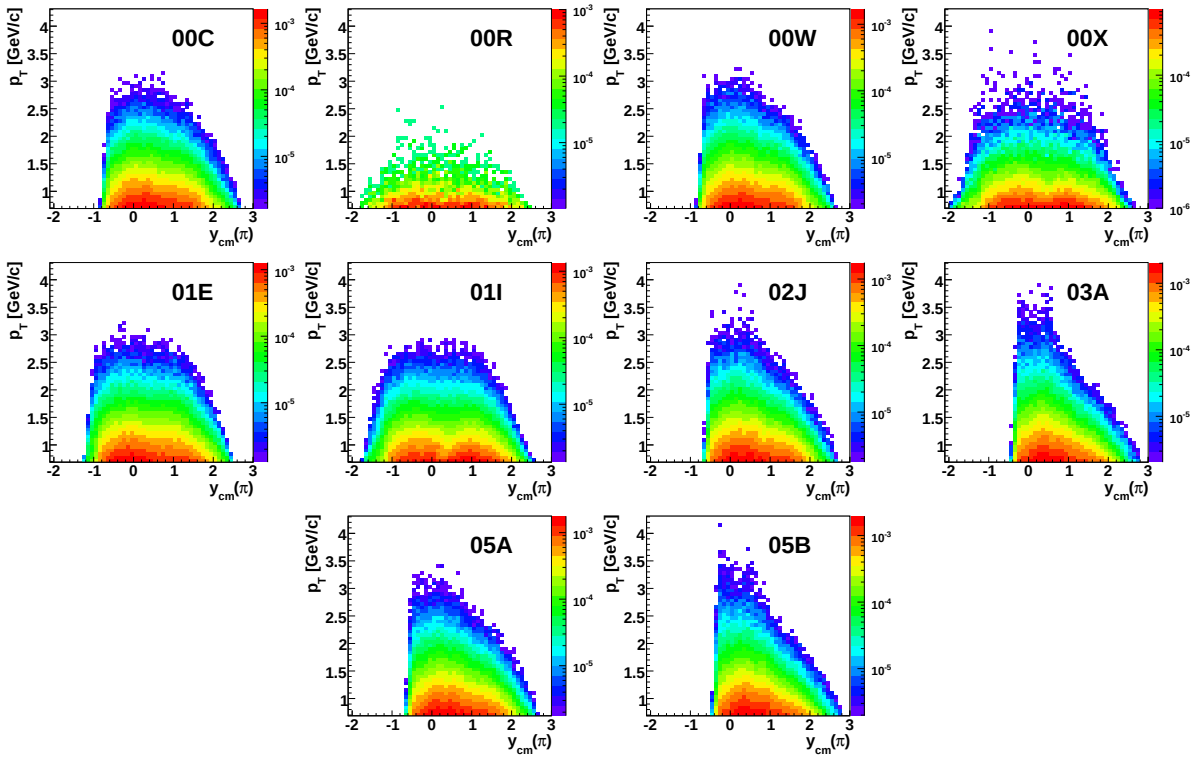

Figure B.1: Distributions of transverse momentum vs. pion-mass rapidity, for accepted particles from all data sets used in this study. Each plot has been produced from 10,000 events, with event and track cuts applied, and normalised to unity.

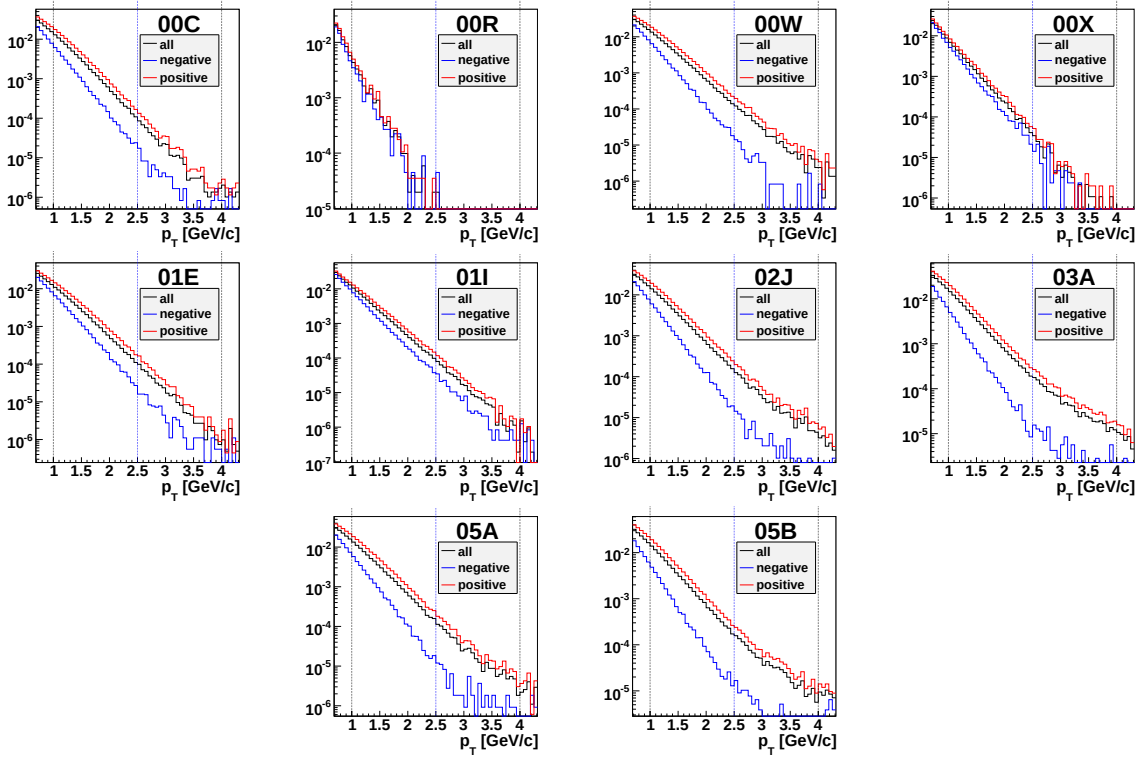

Figure B.2: Distributions of transverse momentum with marked boundaries of trigger- and associate-particle bins, for all charged (black), negative (blue) and positive (red) accepted particles from all data sets used in this study. Each plot has been produced from 10,000 events, with event and track cuts applied, and normalised to unity over the whole p_T range.

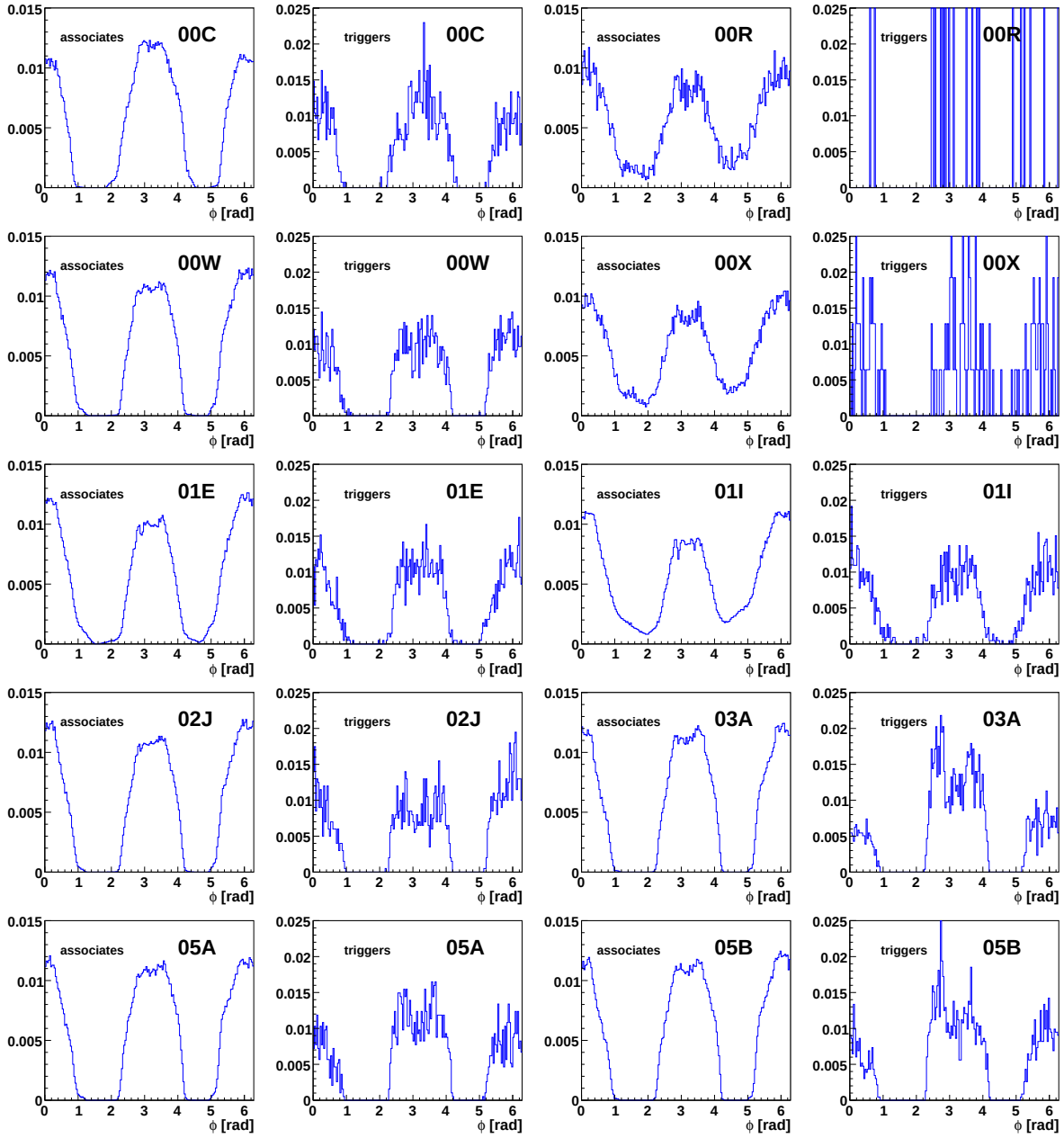

Figure B.3: Distributions of azimuthal angle, separately for trigger and associate particles, for accepted particles from all data sets used in this study. Each plot has been produced from 10,000 events, with event and track cuts applied, and normalised to unity.

Appendix C

Advanced NA49 Track Distance Cut

Instead of using standard, linear extrapolation-based method of calculating distance of closest approach of tracks, in the analysis presented in this dissertation we have employed the technique developed by Stefan Kniege of NA49 specifically for correlation studies — in particular, for HBT interferometry. This procedure consists of the following steps:

1. For each track which has passed all cuts, calculate co-ordinates of their intersections with *all* TPC planes. This is achieved by feeding reconstructed charge, momentum and point of origin of a track to a dedicated tracker class (*T49Trkstep*), which then uses magnetic-field maps of NA49 to reproduce the path the particle in question followed through VTPC1, VTPC2 and/or MTPC, in this order. Those paths together with known z positions of TPC planes provide us with co-ordinates of intersection points, which are stored;

2. After two tracks have been paired, check how many common planes — that is, planes which they both intersected — they have got in each TPC, then calculate distance between the tracks in each common plane of VTPC1, VTPC2 and then MTPC, starting from each chamber's outermost common plane and proceeding inwards;

3. A pair is said to fail the distance cut if the two tracks have got *at least* N common planes in *each* TPC they both pass through and if in *any* of those common planes they have passed closer than d cm from each other.

While investigating the effect of finite two-track resolution of NA49 on angular correlation functions, as described in Section 4.2, the aforementioned cut was used with the following parameters: **50** common planes, **2.2 cm** distance threshold.

Appendix D

Per-trigger Conditional Yield

Figure D.1 presents basic per-trigger conditional yield, as defined by Equation 3.6, for all NA49 collision systems considered in the course of our analysis except for the two more peripheral bins in *Pb+Pb* collisions at 158A GeV. As usual in this dissertation, statistical errors for points are shown as lines and systematic ones as boxes.

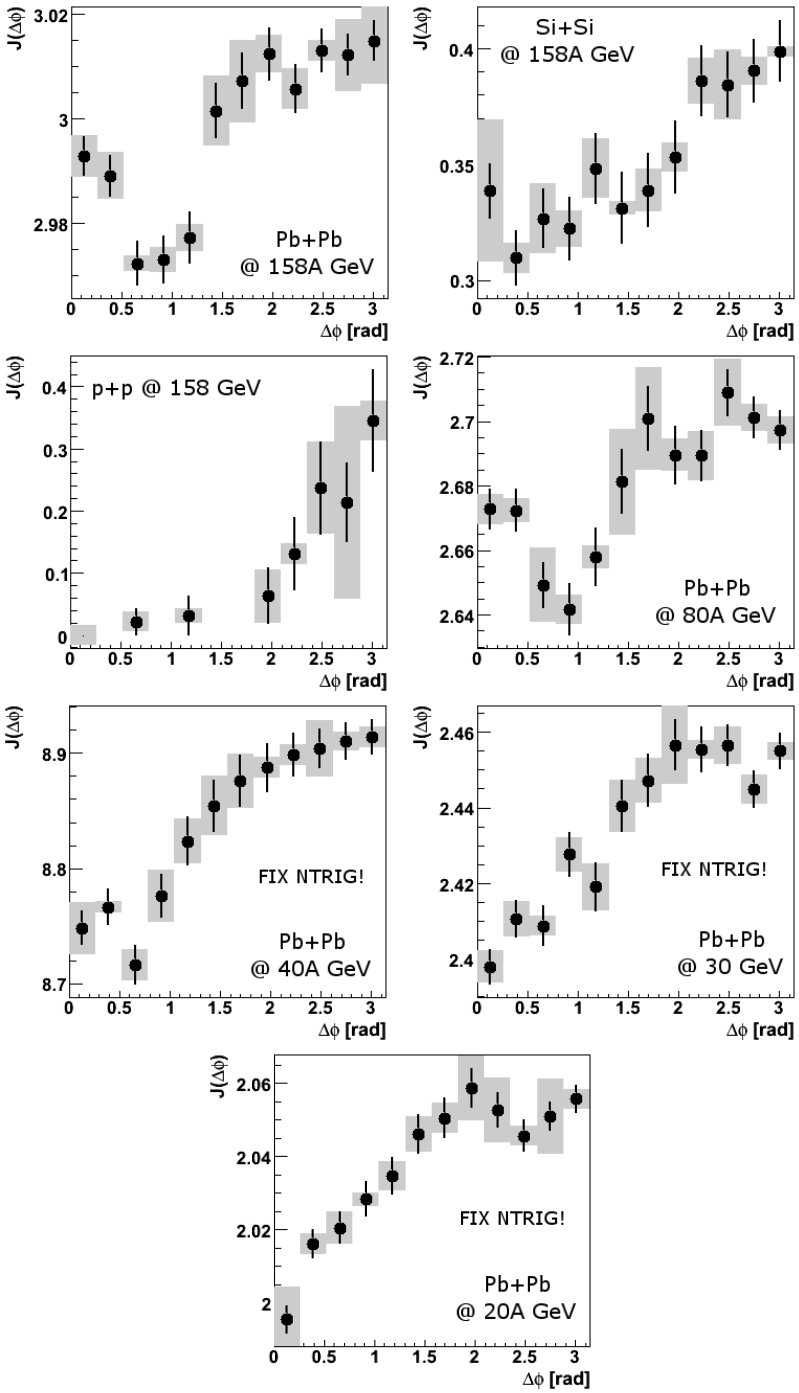

Figure D.1: Basic, *i.e.* without subtraction of flow, per-trigger conditional yield for all NA49 *p*+*p* and central (0–5 %) nucleus–nucleus collision systems discussed in this dissertation.

Appendix E

First Attempt on Three-particle Azimuthal Correlations

As it has been described in Section 3.6.1, a number of issues pertaining to signal extraction in three-particle azimuthal correlation studies exist which could make such extraction difficult or impossible, especially in case of non-uniform azimuthal acceptance. This chapter is devoted primarily to evaluating the feasibility of this approach within technical constraints imposed by NA49. This has been done by the means of a step-by step comparison of components used in the signal-extraction procedure with their CERES counterparts [100]. Plots of raw correlation functions, the hard-soft background, the soft-soft background, trigger flow and extracted signal are shown in Figures: E.1, E.2, E.3, E.4 and E.5, respectively.

NA49 data used here have once again been *Pb+Pb* events at 158A GeV from the *01I* data set. Two-particle functions combined into hard-soft background were shown in Section 5.1.1, whereas v_2 and v_4 values used to calculate trigger flow can be found in Table 5.1.

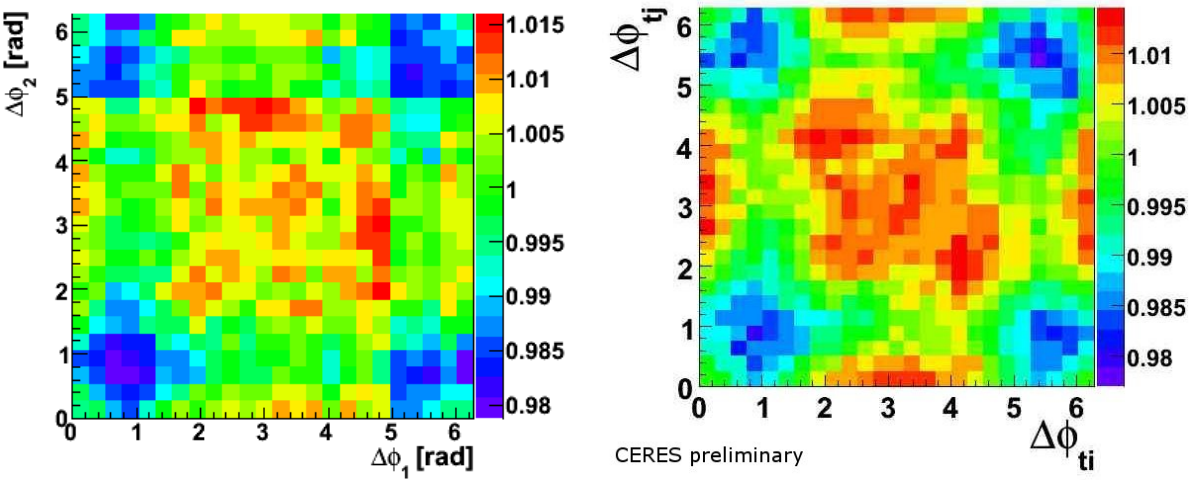

Figure E.1: Raw three-particle azimuthal correlation functions produced by NA49 (left) and CERES (right) in most central heavy-ion collisions at 158A GeV at the CERN SPS.

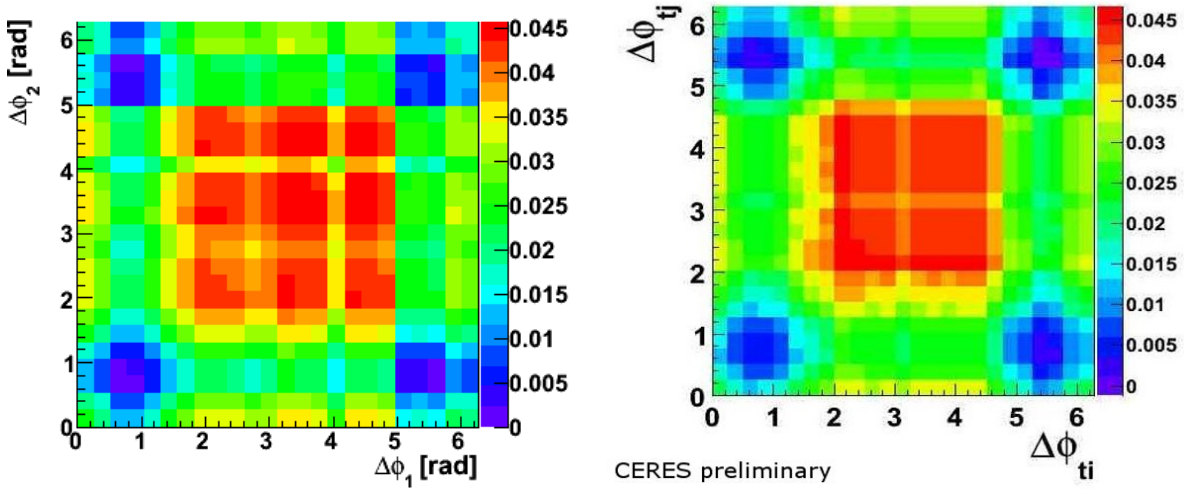

Figure E.2: Three-particle hard-soft background produced by NA49 (left) and CERES (right) in most central heavy-ion collisions at 158A GeV at the CERN SPS.

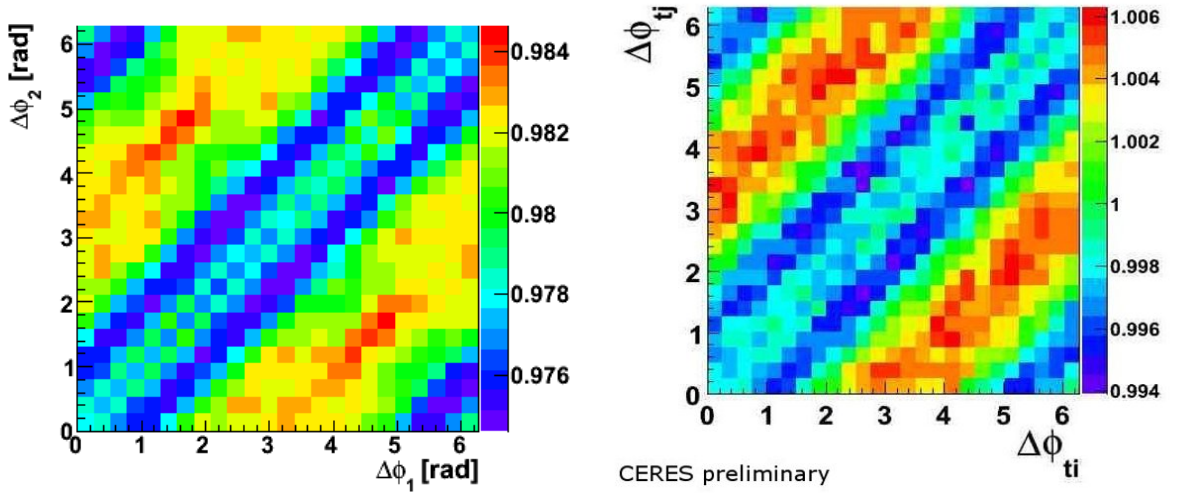

Figure E.3: Three-particle soft-soft background produced by NA49 (left) and CERES (right) in most central heavy-ion collisions at 158A GeV at the CERN SPS.

As shown in Figure E.5, a significant discrepancy exists between CERES and NA49 results after subtraction, even though both the raw correlation functions and different background components used by the two experiments exhibit a large degree of both qualitative (shape) and quantitative (magnitude; note that this includes the scaling factors) similarity. Of the former two, unfortunately it is the NA49 function which is more likely to be incorrect, as both its shape comparing to that from two-particle azimuthal correlations and the values it takes appear to be decidedly unphysical. The discrepancy appears to stem from some general issue rather than being connected to any specific term used in the subtraction. With that in mind, as well as in light of the fact this background-subtraction procedure was developed specifically for experiments

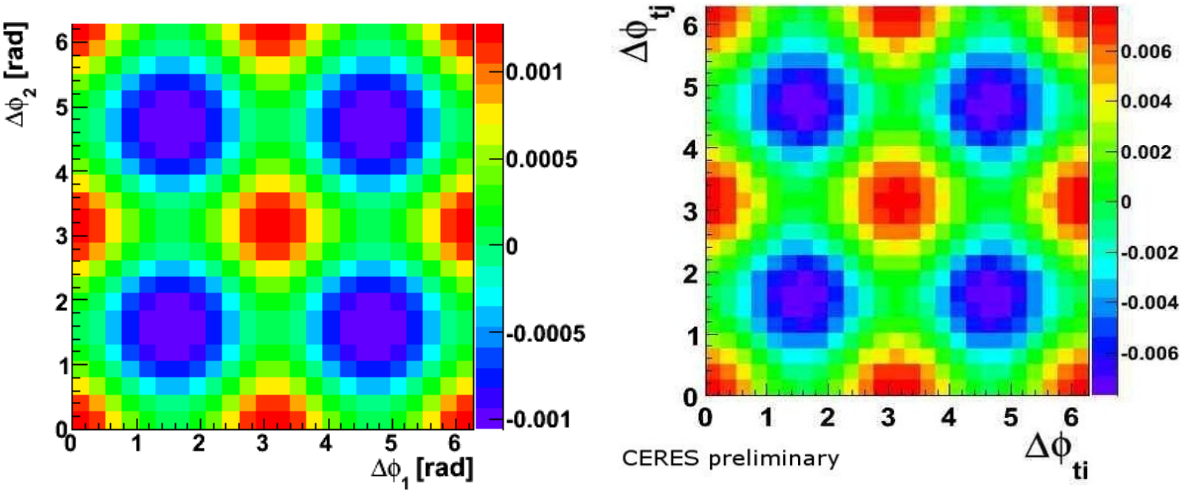

Figure E.4: Three-particle trigger-flow background produced by NA49 (left) and CERES (right) in most central heavy-ion collisions at 158A GeV at the CERN SPS.

featuring almost-uniform azimuthal acceptance, it is quite likely that it is the method itself that has failed when applied to the strongly non-uniform environment of NA49.

At the same time other, more general issues pertaining to this signal-extraction approach exist — namely, the aforementioned reservations towards the two-source model and the ZYAM approach. Results from the centrality scan of two-particle correlations presented earlier on in this chapter imply there may indeed be issues involved in employing this approach there, and given three-particle correlations are even more dependent upon it this could mean their results couldn't be considered reliable even without acceptance problems.

All this aside however, it is worth remembering that the aim behind three-particle azimuthal correlation analyses is to investigate the exact nature of interaction between jets and medium — which implies the correlations must originate from jets. Since results of other parts of this study are consistent with the momentum-conservation scenario instead, three-particle analyses may be unnecessary in order to understand the observed phenomena, thus making the aforementioned issues with this approach irrelevant.

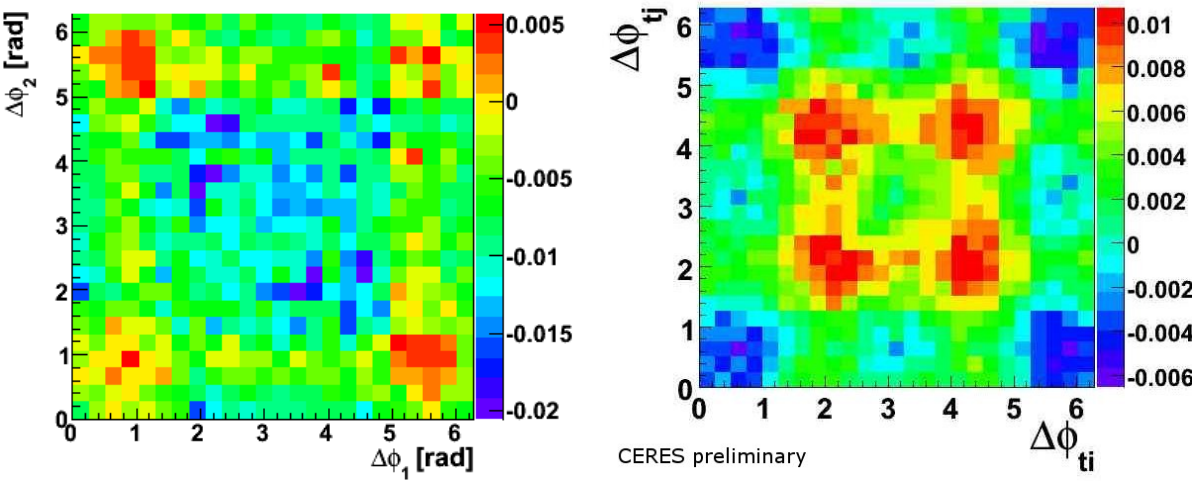

Figure E.5: Background-subtracted three-particle azimuthal correlation functions produced by NA49 (left) and CERES (right) in most central heavy-ion collisions at 158A GeV at the CERN SPS.

Appendix F

The NA49 Collaboration

C. Alt[9], T. Anticic[23], B. Baatar[8],D. Barna[4], J. Bartke[6], L. Betev[10], H. Białkowska[20], C. Blume[9], B. Boimska[20], M. Botje[1], J. Bracinik[3], R. Bramm[9], P. Bunčić[10], V. Cerny[3], P. Christakoglou[2], P. Chung[19], O. Chvala[14], J.G. Cramer[16], P. Csató[4], P. Dinkelaker[9], V. Eckardt[13], D. Flierl[9], Z. Fodor[4], P. Foka[7], V. Friese[7], J. Gál[4], M. Gaździcki[9,11], V. Genchev[18], E. Gładysz[6], K. Grebieszkow[22], S. Hegyi[4], C. Höhne[7], K. Kadija[23], A. Karev[13], D. Kikola[22], M. Kliemant[9], S. Kniege[9], V.I. Kolesnikov[8], E. Kornas[6], M. Kowalski[6], I. Kraus[7], M. Kreps[3], A. Laszlo[4], R. Lacey[19], M. van Leeuwen[1], P. Lévai[4], L. Litov[17], B. Lungwitz[9], M. Makariev[17], A.I. Malakhov[8], M. Mateev[17], G.L. Melkumov[8], A. Mischke[1], M. Mitrovski[9], J. Molnár[4], St. Mrówczyński[11], V. Nicolic[23], G. Pálla[4], A.D. Panagiotou[2], D. Panayotov[17], A. Petridis[2,†], W. Peryt[22], M. Pikna[3], J. Pluta[22], D. Prindle[16], F. Pühlhofer[12], R. Renfordt[9], C. Roland[5], G. Roland[5], M. Rybczyński[11], A. Rybicki[6], A. Sandoval[7], N. Schmitz[13], T. Schuster[9], P. Seyboth[13], F. Siklér[4], B. Sitar[3], E. Skrzypczak[21], M. Slodkowski[22], G. Stefanek[11], R. Stock[9], C. Strabel[9], H. Ströbele[9], T. Susa[23], I. Szentpétery[4], J. Sziklai[4], M. Szuba[22], P. Szymanski[10,20], V. Trubnikov[20], M. Utvić[9], D. Varga[4,10], M. Vassiliou[2], G.I. Veres[4,5], G. Vesztergombi[4], D. Vranić[7], A. Wetzler[9], Z. Włodarczyk[11], A. Wojtaszek[11], I.K. Yoo[15], J. Zimányi[4,†]

[1]NIKHEF, Amsterdam, Netherlands.
[2]Department of Physics, University of Athens, Athens, Greece.
[3]Comenius University, Bratislava, Slovakia.
[4]KFKI Research Institute for Particle and Nuclear Physics, Budapest, Hungary.
[5]MIT, Cambridge, USA.
[6]Henryk Niewodniczanski Institute of Nuclear Physics, Polish Academy of Sciences, Cracow, Poland.
[7]Gesellschaft für Schwerionenforschung (GSI), Darmstadt, Germany.
[8]Joint Institute for Nuclear Research, Dubna, Russia.
[9]Fachbereich Physik der Universität, Frankfurt, Germany.
[10]CERN, Geneva, Switzerland.
[11]Institute of Physics, Jan Kochanowski University , Kielce, Poland.

[12]Fachbereich Physik der Universität, Marburg, Germany.
[13]Max-Planck-Institut für Physik, Munich, Germany.
[14]Charles University, Faculty of Mathematics and Physics, Institute of Particle and Nuclear Physics, Prague, Czech Republic.
[15]Department of Physics, Pusan National University, Pusan, Republic of Korea.
[16]Nuclear Physics Laboratory, University of Washington, Seattle, WA, USA.
[17]Atomic Physics Department, Sofia University St. Kliment Ohridski, Sofia, Bulgaria.
[18]Institute for Nuclear Research and Nuclear Energy, Sofia, Bulgaria.
[19]Department of Chemistry, Stony Brook Univ. (SUNYSB), Stony Brook, USA.
[20]Institute for Nuclear Studies, Warsaw, Poland.
[21]Institute for Experimental Physics, University of Warsaw, Warsaw, Poland.
[22]Faculty of Physics, Warsaw University of Technology, Warsaw, Poland.
[23]Rudjer Boskovic Institute, Zagreb, Croatia.
[†]deceased

Bibliography

[1] S. Weinberg, Eur. Phys. J. **C34**, 5 (2004), arXiv:hep-ph/0401010.

[2] Particle Data Group, W. M. Yao *et al.*, J. Phys. **G33**, 1 (2006).

[3] Super-Kamiokande, Y. Fukuda *et al.*, Phys. Rev. Lett. **81**, 1562 (1998), arXiv:hep-ex/9807003.

[4] H. D. Politzer, Phys. Rev. Lett. **30**, 1346 (1973).

[5] D. J. Gross and F. Wilczek, Phys. Rev. Lett. **30**, 1343 (1973).

[6] S. B. Ruester, V. Werth, M. Buballa, I. A. Shovkovy, and D. H. Rischke, Phys. Rev. **D72**, 034004 (2005), arXiv:hep-ph/0503184.

[7] M. G. Alford, K. Rajagopal, and F. Wilczek, Phys. Lett. **B422**, 247 (1998), arXiv:hep-ph/9711395.

[8] M. G. Alford, K. Rajagopal, and F. Wilczek, Nucl. Phys. **B537**, 443 (1999), arXiv:hep-ph/9804403.

[9] F. R. Brown *et al.*, Phys. Rev. Lett. **65**, 2491 (1990).

[10] M. Gazdzicki and M. I. Gorenstein, Acta Phys. Polon. **B30**, 2705 (1999), arXiv:hep-ph/9803462.

[11] NA49, M. Gazdzicki *et al.*, J. Phys. **G30**, S701 (2004), arXiv:nucl-ex/0403023.

[12] Z. Fodor and S. D. Katz, JHEP **04**, 050 (2004), arXiv:hep-lat/0402006.

[13] F. Karsch, J. Phys. **G31**, S633 (2005), arXiv:hep-lat/0412038.

[14] NA49-future, M. Gazdzicki *et al.*, PoS **CPOD2006**, 016 (2006), arXiv:nucl-ex/0612007.

[15] G. S. F. Stephans, J. Phys. **G32**, S447 (2006), arXiv:nucl-ex/0607030.

[16] CBM, P. Senger, J. Phys. Conf. Ser. **50**, 357 (2006).

[17] G. V. Trubnikov *et al.*, EPAC'08, 11th European Particle Accelerator Conference, 23-27 June 2008, Genoa, Italy.

[18] WMAP, D. N. Spergel *et al.*, Astrophys. J. Suppl. **148**, 175 (2003), arXiv:astro-ph/0302209.

[19] E. Rutherford, Phil. Mag. **21**, 669 (1911).

[20] P. Waloschek and R. Wideröe, DESY-94-039.

[21] J. D. Cockroft and E. T. S. Walton, Nature **129**, 242 & 649 (1943).

[22] E. O. Lawrence and M. S. Livingston, Phys. Rev. **40**, 19 (1932).

[23] L. J. Haworth, Synchrotron design in general and the Brookhaven Cosmotron in particular, in *Nuclear physics and the physics of fundamental particles; proceedings of the international conference, September 17 to 22, 1951*, pp. 18–28, 1951.

[24] A. M. Baldin and I. N. Semenyushkin, Atomic Physics **43**, 1146 (1977).

[25] J. D. Bjorken, Presented at SLAC Multi-Anniversary Celebration, Stanford CA, 15 Aug 1982.

[26] B. Richter, Kerntech. **12**, 531 (1970).

[27] J. B. Adams, The CERN 400-GeV Proton Synchrotron (CERN SPS), in *Protvino 1977, Proceedings, Xth International Conference On High Energy Accelerators, Serpukhov 1977, Vol. 1*, pp. 17–29, 1977.

[28] R. R. Wilson, Phys. Today **30N10**, 23 (1977).

[29] P. J. Reardon, Nucl. Phys. **A478**, 861c (1988).

[30] E. . Bruning, O. *et al.*, CERN-2004-003-V-1.

[31] J. Brau *et al.*, ILC-REPORT-2007-001.

[32] A. A. Kuznetsov, Nucl. Phys. **A400**, 493c (1983).

[33] R. Stock, J. Phys. **G30**, S633 (2004), arXiv:nucl-ex/0405007.

[34] W. Frati, Nucl. Phys. **A418**, 177c (1984).

[35] Y. P. Viyogi, Pramana **41/1**, 359 (1993).

[36] M. A. Faessler, Invited talk given at Int. Symp. on Multiparticle Dynamics, Seewinkel, Austria, Jun 16-20, 1986.

[37] Y. Miake, Nucl. Phys. **A538**, 149c (1992).

[38] T. L. Trueman, Nucl. Phys. **A525**, 117c (1991).

[39] P. Giubellino, Nucl. Phys. **A699**, 103 (2002).

[40] BRAHMS, F. Videbaek, Nucl. Phys. **A566**, 299c (1994).

[41] PHENIX, J. C. Gregory *et al.*, Nucl. Phys. **A566**, 287c (1994).

[42] PHOBOS, B. Wyslouch, Nucl. Phys. **A566**, 305c (1994).

[43] STAR, J. W. Harris, Nucl. Phys. **A566**, 277c (1994).

[44] A. A. Isayev, (2008), arXiv:0810.4762.

[45] N. Grau and f. t. A. Collaboration, J. Phys. **G35**, 104040 (2008), arXiv:0805.4656.

[46] CMS, D. J. Hofman, Acta Phys. Polon. **B38**, 993 (2007).

[47] A. Bialas, A. Bleszynski, and W. Czyz, Nucl. Phys. **B111**, 461 (1976).

[48] STAR, J. G. Ulery, (2007), Presented at XXXVII International Symposium on Multiparticle Dynamics, Berkeley CA, 2007.

[49] R. Vogt, Phys. Rev. **C71**, 054902 (2005), arXiv:hep-ph/0411378.

[50] J. W. Cronin *et al.*, Phys. Rev. **D11**, 3105 (1975).

[51] L. D. McLerran and R. Venugopalan, Phys. Rev. **D49**, 2233 (1994), arXiv:hep-ph/9309289.

[52] L. D. McLerran and R. Venugopalan, Phys. Rev. **D49**, 3352 (1994), arXiv:hep-ph/9311205.

[53] L. D. McLerran, Lect. Notes Phys. **583**, 291 (2002), arXiv:hep-ph/0104285.

[54] W. Broniowski and W. Florkowski, Phys. Rev. Lett. **87**, 272302 (2001), arXiv:nucl-th/0106050.

[55] PHENIX, A. Adare *et al.*, Phys. Rev. Lett. **98**, 232301 (2007), arXiv:nucl-ex/0611020.

[56] G. E. Brown, C.-H. Lee, and M. Rho, (2004), arXiv:hep-ph/0408253.

[57] D. G. d'Enterria and D. Peressounko, Eur. Phys. J. **C46**, 451 (2006), arXiv:nucl-th/0503054.

[58] NA50, L. Ramello, Nucl. Phys. **A774**, 59 (2006).

[59] R. E. Taylor, Presented at 1969 Int. Conf. on Electron and Photon Interactions at High Energies, Daresbury, England.

[60] OPAL Collaboration, `http://opal.web.cern.ch/`.

[61] CDF Collaboration, `http://www-cdf.fnal.gov/`.

[62] P. Darriulat, Ann. Rev. Nucl. Part. Sci. **30**, 159 (1980).

[63] J. D. Bjorken, Phys. Rev. **163**, 1767 (1967).

[64] R. P. Feynman, Invited paper at the Third Conference on High-Energy Collisions, Stony Brook, New York, 5-6 Sep 1969.

[65] J. D. Bjorken and E. A. Paschos, Phys. Rev. **185**, 1975 (1969).

[66] R. D. Field and R. P. Feynman, Phys. Rev. **D15**, 2590 (1977).

[67] R. P. Feynman, R. D. Field, and G. C. Fox, Nucl. Phys. **B128**, 1 (1977).

[68] R. P. Feynman, R. D. Field, and G. C. Fox, Phys. Rev. **D18**, 3320 (1978).

[69] J. C. Collins, D. E. Soper, and G. Sterman, Nucl. Phys. **B308**, 833 (1988).

[70] R. J. Glauber, *Lectures in Theoretical Physics, Vol. 1* (Interscience, New York, 1959), p. 315.

[71] W. Florkowski, Lectures for PhD students, Institute of Nuclear Physics of the Polish Academy of Sciences.

[72] M. H. Seymour, (2000), arXiv:hep-ph/0007051, Talks given at 35th Rencontres de Moriond: QCD and High Energy Hadronic Interactions, Les Arcs, Savoie, France, 18-25 March 2000, and at 8th International Workshop on Deep Inelastic Scattering and QCD (DIS 2000), Liverpool, England, 25-30 Apr 2000.

[73] J. D. Bjorken, FERMILAB-PUB-82-059-THY.

[74] M. Gyulassy and M. Plumer, Phys. Lett. **B243**, 432 (1990).

[75] STAR, P. Jacobs, Topics in Heavy Ion Collisions, McGill University, 25-28 June 2003.

[76] H. Stoecker, Nucl. Phys. **A750**, 121 (2005), arXiv:nucl-th/0406018.

[77] J. Ruppert and B. Muller, Phys. Lett. **B618**, 123 (2005), arXiv:hep-ph/0503158.

[78] J. Casalderrey-Solana, E. V. Shuryak, and D. Teaney, (2006), arXiv:hep-ph/0602183.

[79] PHENIX, A. Adare *et al.*, Phys. Rev. **C78**, 014901 (2008), arXiv:0801.4545.

[80] STAR, M. J. Horner, J. Phys. **G34**, S995 (2007), arXiv:nucl-ex/0701069.

[81] STAR, J. Adams *et al.*, Phys. Rev. Lett. **95**, 152301 (2005), arXiv:nucl-ex/0501016.

[82] STAR, J. Putschke, J. Phys. **G34**, S679 (2007), arXiv:nucl-ex/0701074.

[83] STAR, J. L. Klay, Nucl. Phys. **A715**, 733 (2003), arXiv:nucl-ex/0210026.

[84] K. Kajantie, Presented at Quark Matter 2002, Nantes.

[85] NA57, F. Antinori *et al.*, J. Phys. Conf. Ser. **5**, 64 (2005), arXiv:hep-ex/0406004.

[86] CERN SPS Operation, `http://ab-dep-op-sps.web.cern.ch/ab-dep-op-sps/`.

[87] NA49, S. Afanasev *et al.*, Nucl. Instrum. Meth. **A430**, 210 (1999).

[88] NA49, A. László, NA49 Technical Note, CERN EDMS 815907.

[89] NA49, C. Alt *et al.*, (2007), arXiv:0712.3216.

[90] NA49, W. Rauch *et al.*, IEEE Trans. Nucl. Sci. **41**, 30 (1994).

[91] A. László, *Nuclear Modification at 17.3 GeV Nucleon-Nucleon Collision Energy, Measured by the Experiment CERN-NA49*, PhD thesis, Eötvös Loránd University (ELTE), Budapest, Hungary, 2008.

[92] PHENIX, C. Zhang, J. Phys. **G34**, S671 (2007).

[93] PHENIX, S. S. Adler *et al.*, Phys. Rev. Lett. **97**, 052301 (2006), arXiv:nucl-ex/0507004.

[94] N. N. Ajitanand *et al.*, Phys. Rev. **C72**, 011902 (2005), arXiv:nucl-ex/0501025.

[95] A. M. Poskanzer and S. A. Voloshin, Phys. Rev. **C58**, 1671 (1998), arXiv:nucl-ex/9805001.

[96] PHENIX, N. N. Ajitanand, Nucl. Phys. **A783**, 519 (2007), arXiv:nucl-ex/0609038.

[97] J. G. Ulery and F. Wang, Nucl. Instrum. Meth. **A595**, 502 (2008), arXiv:nucl-ex/0609016.

[98] E. L. Berger, Nucl. Phys. **B85**, 61 (1975).

[99] C. A. Pruneau, Phys. Rev. **C74**, 064910 (2006), arXiv:nucl-ex/0608002.

[100] CERES, S. Kniege, Presented at the final workshop of the Virtual Institute of Strongly Interacting Matter, Frankfurt, May 2008.

[101] NA49, D. Kikoła, private communication.

[102] STAR, M. J. Horner, Parallel talk at Quark Matter 2006, Shanghai.

[103] STAR, F. Wang, Communication on mailing lists of the STAR experiment.

[104] NA49, C. Alt *et al.*, Phys. Rev. **C77**, 024903 (2008), arXiv:0710.0118.

[105] M. Gyulassy, Final workshop of the Virtual Institute of Strongly Interacting Matter, University of Frankfurt, 19 May 2008.

[106] N. Borghini, Phys. Rev. **C75**, 021904 (2007), arXiv:nucl-th/0612093.

[107] STAR, F. Wang, Presented at Quark Matter 2004, Oakland CA.

[108] PHENIX, S. S. Adler *et al.*, Phys. Rev. Lett. **98**, 172302 (2007), arXiv:nucl-ex/0610036.

[109] D. Antreasyan *et al.*, Phys. Rev. **D19**, 764 (1979).

[110] P. B. Straub *et al.*, Phys. Rev. Lett. **68**, 452 (1992).

[111] J. Casalderrey-Solana, Plenary talk at Quark Matter 2006, Shanghai.

[112] J. Noronha, G. Torrieri, and M. Gyulassy, Phys. Rev. **C78**, 024903 (2008), arXiv:0712.1053.

[113] CERES, S. Kniege, Presented at XXXVII International Symposium on Multiparticle Dynamics, Berkeley CA, 2007.

[114] S. A. Bass *et al.*, Prog. Part. Nucl. Phys. **41**, 255 (1998), arXiv:nucl-th/9803035.

[115] M. Bleicher *et al.*, J. Phys. **G25**, 1859 (1999), arXiv:hep-ph/9909407.

[116] T. Sjostrand, S. Mrenna, and P. Skands, JHEP **05**, 026 (2006), arXiv:hep-ph/0603175.